Synthesis, Transport, Structural, And Electronic Properties Studies Of Topological Systems

Thesis submitted for the degree of

Doctor of Philosophy (Science)
in
Physics (Experimental)

by

Sayan Routh

Department of Physics
University of Calcutta
2024

Dedicated to my Parents

.....

Acknowledgement

It has been a great honour to participate in and successfully conclude my integrated Ph.D. program at the S.N. Bose National Centre for Basic Sciences. The exceptional educational and research facilities provided have greatly enriched both my academic and personal growth. Along my academic journey, I have had the privilege of learning from many mentors who have emphasized the significance of education and inspired my passion for research. I am sincerely grateful to each of them for their guidance and support.

I am delighted to express my sincere respect and heartfelt gratitude to Dr.Thirupathaiah Setti, my Ph.D. supervisor in the Department of Condensed Matter and Materials Physics at the S.N. Bose National Centre for Basic Sciences. His insightful perspective, visionary approach, expert knowledge, and unwavering guidance have been essential during the planning and development phases of this research endeavor. I am deeply thankful for his enthusiastic engagement and unwavering encouragement, which have been crucial in completing this work.

I extend my sincere gratitude to my supervisor, Prof. Prosenjit Singha Deo, for his consistent guidance and support throughout my research endeavors. His invaluable advice and direction will undoubtedly guide me towards success in my future career and life.

I am thankful to Professor Ranjan Chaudhury for allowing me the opportunity to pursue the magnetism project during my M.Sc. I express my gratitude to Dr.Soma Banik at RRCAT, Indore for her help in the x-ray photoelectron spectroscopy (XPS) measurements. Additionally, I am also extremely grateful to Prof. Kamraju Natarajan at the Indian Institute of Science Education and Research, Kolkata, for his invaluable help in the pump-probe spectroscopy measurements. I express my gratitude to my B.Sc. teacher, Professor Chanchal Kumar Chatterjee, whose inspiration encouraged me to embark on this journey.

I wish to express my genuine appreciation to the entire quantum-materials group. I am deeply grateful to Dr.Indrani Kar, Susmita Changdar, Achintya Low, Shubham Purwar, Susanta Ghosh, Soumya Ghorai, and Anupam Barik for their friendship and collaborative efforts, which have been essential to my research journey. Additionally, I owe a debt of gratitude to the postdoctoral scholars in our group, Dr.Tushar Kanti Bhowmik,

Dr.Reena Goyel, Dr.Pankaj Maheshwari, Dr.Tushita Sau, and Dr.Ayana Mukhopadhay, whose invaluable insights have guided me through numerous research challenges. Specially, I wish to extend my humble respect and heartfelt gratitude to Dr.Tushar Kanti Bhowmik for his encouragement, guidance, and supportive friendship, akin to an elder brother. His innovative ideas and insightful discussions have consistently inspired me to overcome the challenges in my research endeavors.

In addition to my lab mates, I want to extend my gratitude to Akash da, Sudipta da, Saikat da, Sasthi da, Parushattom da, and Anirban da for making these years truly memorable. Special thanks to Akash da and Sudipta da for their invaluable assistance during my Ph.D. journey. I wish to convey my heartfelt gratitude to all my close friends for creating a warm and friendly atmosphere in campus. I am thankful to many dear juniors for their assistance and delightful companionship. I wish to express my appreciation to my fellow I.Ph.D. colleagues, Ankur Srivastava, Anuj Kumar Dhiman, Achintya Low, Megha Dave, Anwesha Chakrobarty, Neeraj Kumar, and Raghvendra Pandey. I am especially thankful to Anuj, Achintya, and Ankur for their consistent encouragement and support as friends.

I appreciate the technical staff, especially Shakti da, Urmi di, Debarghya da, Sourav da, Amit da, and Joy da, for their consistent assistance during sample characterization and measurements. Furthermore, I would like to express my appreciation to the student mess, institute canteen, kitchen team, all members of the group-D staff, and security personnel for their dedicated endeavors in maintaining a healthy, hygienic, and secure campus environment.

Finally, I want to express my deepest respect and gratitude to my entire family, especially my mother(Maa) and father (Baba), for their unwavering support, blessings, and care. I extend my heartfelt respect to my uncle, aunt, my younger brother Atindra, and my elder brother Suman da for their love, support, and care.The culmination of the blessings, support, affection, and good wishes from all these individuals has resulted in the completion of this Ph.D. thesis that I am now submitting.

Finally, I express my gratitude to the almighty god for leading me through the triumphs and challenges of this incredible journey.

Sayan Routh

Abstract

The emergence of topological materials in the realm of condensed matter physics has ushered in an entirely new perspective, wherein these materials are characterized based on their electronic band structure topology and the intrinsic crystal symmetries of the systems governing the physics of topology. Topological materials have become the focus of extensive theoretical and experimental investigations, continuously unveiling the novel exotic phases of the matter. While the discovery of topological insulators signifies the inception of this field, subsequent realizations of Dirac, Weyl, and nodal-line semimetals have further expanded and enriched the research of this domain. To comprehend the efficiency and suitability of these compounds for quantum computation, it is essential to gain a microscopic understanding of their various properties. My thesis aims to synthesize high-quality single crystals of various topological systems and investigate their structural, electrical transport, and magnetic properties. Therefore, I have grown $Cr_{0.79}Se$, $FeCr_2Te_4$, and $HoSiAl_2$ due to their intriguing topological properties.

During my Ph.D. thesis, I have grown the polycrystal of $Cr_{0.79}Se$, which has a paramagnetic (PM) to antiferromagnetic (AFM) transition below 225 K. AFM metals with noncollinear spin textures have recently been acclaimed as a viable candidate for the anomalous Hall effect (AHE), which is induced by the Berry curvature. This discovery $Cr_{0.79}Se$ inspired us to revisit the system's structural, electrical, and magnetic properties. The X-ray diffraction (XRD) analysis reveals a NiAs-type structure for $Cr_{0.79}Se$. Furthermore, we identify that the NiAs-type structure remains stable up to sample temperatures of 600°C, as observed from the temperature-dependent XRD measurements. A notable exchange bias is observed below 100K, stemming from the exchange interaction between the ferro- and antiferromagnetic phases. We grew a $FeCr_2Te_4$ single crystal, which was predicted to host Weyl nodes below the Fermi level (44 meV below). The electron scattering mechanism and the impact of the external magnetic field on the scattering coefficients have been thoroughly investigated in this system. Furthermore, the magnetotransport properties of $FeCr_2Te_4$ are studied systematically. In particular, we focus on magnetoresistance (MR) behavior in the critical temperature region. Next, it was theoretically predicted that a novel kind of Weyl semimetal state in the RAlGe (R = rare-earth) family breaks both time-reversal and inversion symmetries. Moreover, $R_2Al_3Si_2$ (R=Tb, Dy, Ho, Er, and Tm) crystallizes in a C-centred monoclinic $Y_2Al_3Si_2$-type crystal structure. In

particular, the Ho-Al-Si system is stabilized in $Ho_2Al_3Si_2$ and $HoSiAl_2$. We have grown the $HoSiAl_2$ single crystal and studied in detail its physical properties, such as magnetic susceptibility, electrical resistivity, Hall effect, magnetoresistance measurements, and electronic band structure calculations.

Publications

List of publications:

1. Observation of Exchange Bias in Antiferromagnetic $Cr_{0.79}Se$ Due to the Coexistence of Itinerant Weak Ferromagnetism at Low Temperatures, **Sayan Routh** and Setti Thirupathaiah. ACS omega, **6(42)**, 28012-28018, (2021)

2. Magnetoresistance behavior across the critical region in ferrimagnet $FeCr_2Te_4$ single crystal, **Sayan Routh**, Indrani Kar, Achintya Low, Susanta Ghosh, Tushar Kanti Bhowmik Physics Letters A, **486**, 129101, (2023).

3. Magnetic and magnetotransport properties of proposed topological Weyl semimetal $HoSiAl_2$, **Sayan Routh**, Tushar Kanti Bhowmik, Achintya Low, Setti Thirupathaiah.(to be submitted)

List of Publications apart from the thesis work:

1. Effect of Mo doping on the electrical and magnetic properties of antiferromagnetic CrSe, **Sayan Routh**, Susanta Ghosh, P.K.Maheswari, P.Singha Deo, Setti Thirupathaiah. Materials Today: Proceedings,**65**, 342-344, (2022).

2. Single crystal growth, electrical, and magnetic properties studies on hexagonal CoSe, Shubham Purwar,**Sayan Routh**, Setti Thirupathaiah. Materials Today: Proceedings, **65**, 332-334, (2022).

3. Tuning of topological properties in the strongly correlated antiferromagnet Mn_3Sn via Fe doping, Achintya Low, Susanta Ghosh, Susmita Changdar,**Sayan Routh**,Shubham Purwar and Setti Thirupathaiah. Physical Review B 106, 144429,(2022).

4. Nonmagnetic Sn doping effect on the electronic and magnetic properties of antiferromagnetic topological insulator $MnBi_2Te_4$, Susmita Changdar, Susanta Ghosh ,

Kritika Vijay , Indrani Kar , **Sayan Routh** , P.K. Maheshwari , Soumya Ghorai , Soma Banik , S. Thirupathaiah Physica B: Condensed Matter, **657**, 414799, (2023).

5. Observation of weak Kondo effect and angle dependent magnetoresistance in layered antiferromagnetic V_5S_8 single crystal, Indrani Kar,**Sayan Routh**, Soumya Ghorai, Shubham Purwar and Setti Thirupathaiah. Solid State Communications, **369**, 115209, (2023).

Contents

List of Figures

Chapter 1

Introduction

In this chapter, we will discuss both the theoretical and experimental advancements that have contributed to our current understanding of topological band theory. These developments, unfolding over decades, have each played a pivotal role in advancing condensed matter physics. Our exploration will commence with a discussion of the band theory of solids, a foundational concept that significantly influences our comprehension of material properties.

Following this, we will delve into the detection of the integer quantum Hall effect and the introduction of non-trivial topological states in various types of systems. Subsequently, we will outline the distinctive features of quantum Hall insulators, three-dimensional topological insulators, and semi-metals, presenting them in the order of their theoretical predictions and experimental confirmations. Another aspects investigated in this thesis are the exchange bias mechanism, anomalous Hall effect, and the magnetocaloric effect. In this thesis, we have investigated transport and magnetic phenomena in various topological systems.

1.1 Band theory

The solid-state band theory stands as a cornerstone in condensed matter physics, serving as a crucial tool for the categorization of various states of matter. Arising from the quantized energy levels of electrons within an atom, this theory expands when applied to solids, where many atoms form a periodic lattice. Unlike the distinct levels seen in individual atoms, the motion of electrons in solids are influenced not by individual atoms but by the collective effect of neighboring atoms. Consequently, the energy states of electrons form continuous bands.

The Bloch Hamiltonian $H_m(k)$ and Bloch wave function $|u_m(k)>$, with k representing crystal momentum, describe the electronic motion inside the solid. The fully occupied band below the Fermi level is termed as the valence band, while the subsequent band above the Fermi level which could be partially or completely vacant—is called as the conduction band. The electrons only from the conduction band contribute to the charge conduction in solids. This simplified model aids in classifying materials into different groups, as illustrated in Fig. 1.1. For instance, insulators exhibit a substantial energy

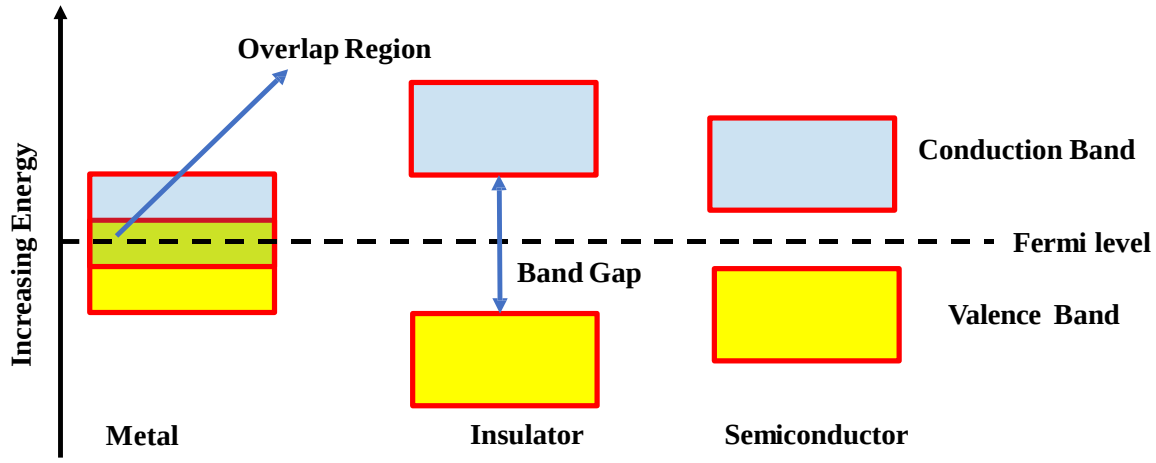

Figure 1.1: Various electronic states of matter according to the band theory.

gap, differentiating the valence and conduction bands above and below the Fermi level. Thus, electrons need to be excited in order to allow charge flow from the valence to the conduction band. Given the significant energy gap (E_g) at room temperature, insulators are incapable of conducting electrical current. In contrast, metals feature overlapping conduction and valence bands, facilitating ample conduction of electrons. Semiconductors, positioned between insulators and metals, possess a relatively smaller band gap, allowing some electrons to reach the conduction band at room temperature. Similarly, semi-metals can conduct current, with their conduction and valence bands touching each other, contributing only a limited number of electrons to the conduction band. For many years, band theory stood as a highly effective and exclusive framework for elucidating the

electronic properties of crystalline solids. Specifically, the band theory is playing a vital role in understanding various topological properties of solid.

1.2 Topology in geometry

Topology serves as a mathematical framework for classifying various geometric entities [1]. Within this context, two objects fall into the same topological category if one can be continuously transformed into the other through processes like stretching or bending, without tearing or gluing. For instance, a solid sphere can be transformed into a disc by compressing along a diagonal axis. Although they may seem different, they belong to the same topological class. However, introducing a hole to create an annular shape places the object into a new topological group. In fact, a fundamental concept in topology involves counting the number of holes in objects as a basis for their classification. For a more precise definition, we employ the genus value (g) provided by the Gauss-Bonnet theorem,

$$\int_S K\, dS = 4\pi(1-g) \tag{1.1}$$

where K is the Gaussian curvature. For a sphere with radius r, K = $1/r^2$ and leads to g = 0.

1.3 Topology in electronic band theory

Like in geometry, topology can be employed in band theory to categorize various electronic states [2, 3]. By smoothly adjusting the Bloch Hamiltonian $H_m(k)$, one can finely regulate the band gap between the conduction and valence bands within a system. As long as these two bands refrain from making direct contact, ensuring the band gap remains finite, the material remains within the same topological class. Consequently, both an ordinary insulator and semiconductor are topologically equivalent to a vacuum, characterized by a band gap of approximately 10^6 eV (for pair production). In the realm of band theory, however, a departure from the concept of genus is observed, replaced by a novel topological invariant known as the Chern invariant (n_m). The n_m remains unaffected by the smooth variation of $H_m(k)$ but undergoes changes upon transitioning to a different topological class. The mathematical formulation of the Chern invariant stems from the Berry phase linked to the Bloch wave function $|u_m(k)>$. The Berry phase is determined by the line integral of $A_m = i <u_m|\nabla k|u_m >$ along a closed path. Drawing an analogy to an electromagnetic vector potential, the Berry connection (A_m) is established. Consequently, the Berry flux F_m can be expressed as $\nabla k \times A_m$. The Chern invariant is defined as the cumulative Berry flux within the Brillouin zone,

$$n_m = \frac{1}{2\pi}\int F_m d^2k \tag{1.2}$$

1.4 Integer quantum Hall effect

In 1980, K. von Klitzing, G. Dorda, and M. Pepper unveiled the phenomenon known as the integer quantum Hall effect (IQHE) [4]. This phenomenon emerges in a two-dimensional (2D) electron gas when subjected to strong magnetic field. The Hall conductivity (σ_{xy}) is observed to exhibit highly quantized behavior, remains insensitive to the electron gas's geometry [4, 5]. As depicted in Fig. 1.2, the integer quantum Hall effect (IQHE) can be semiclasically explained. When a magnetic field is applied, electrons undergo cyclotron orbits, and their energy becomes quantized as $E_n=(n+\frac{1}{2})\hbar\omega_c$, , where ω_c is the cyclotron frequency, and n is an integer. These distinct energy levels, known as Landau levels, exhibit a degeneracy directly proportional to the magnetic field strength. Consequently, with an increasing magnetic field, each Landau level can accommodate more electrons. In order to minimize energy, electrons are compelled to transition from higher to lower Landau levels. When electrons occupy up to the N^{th} Landau level, leaving the rest empty, the observed Hall conductivity is expressed as $\sigma_{xy}= \frac{Ne^2}{h}$. In this configuration, the Landau levels can be treated as energy bands, similar to the principles of band theory. Consequently, with the filled N^{th} Landau level separated from the empty $(N+1)^{th}$ level by a constant energy gap $\hbar\omega_c$, the integer quantum Hall state (IQHS) is anticipated to behave like a typical insulator. Despite this insulator-like behavior, the IQHS exhibits

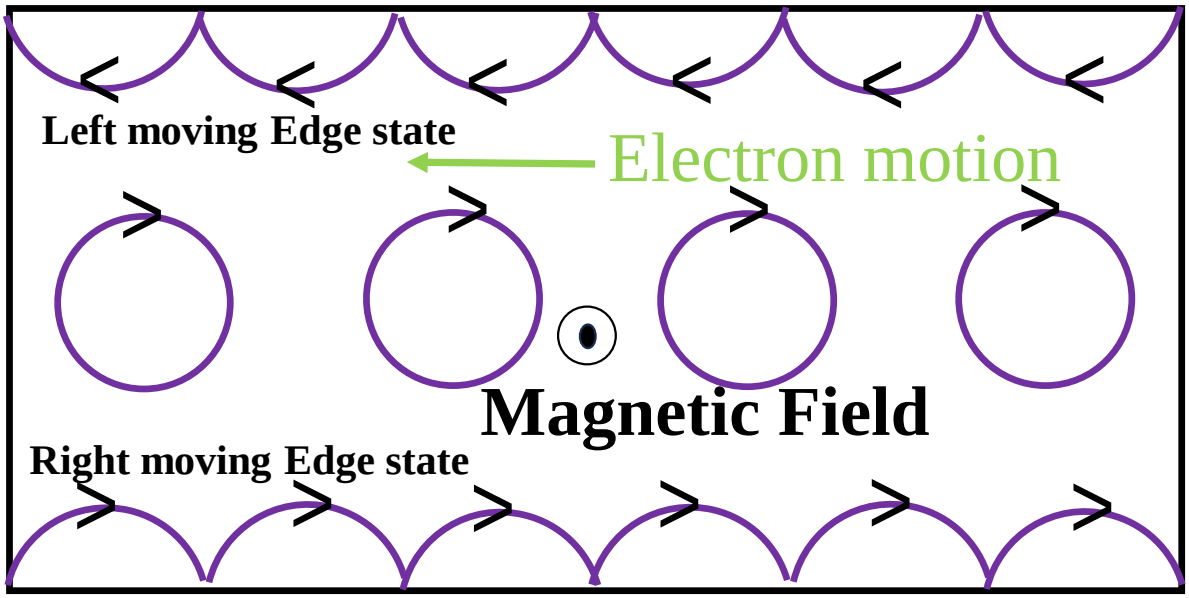

Figure 1.2: A semi-classical depiction of the integer quantum Hall state involving a two-dimensional electron gas subjected to an external magnetic field perpendicular to the plane.

a quantized Hall conductivity under an electric field. Another notable characteristic of the IQHS is the presence of conducting edge states, which manifest at the boundary of the 2D electron gas due to the skipping motion of electrons as they bounce off the edge. These states, known as "chiral edge states", propagate in only one direction without

backscattering, irrespective of any disorder in the system. The IQHE does not conform to the conventional band theory description of solids, marking the introduction of topological order in condensed matter physics.

In 1982, D. J. Thouless, M. Kohmoto, M. P. Nightingale, and M. den Nijs embraced the concept of Berry connection to mathematically derive the Hall conductivity in the Integer Quantum Hall Effect (IQHE) [6]. Applying the Kubo formula, they established the correlation,

$$\sigma_{xy} = \frac{ne^2}{h} \tag{1.3}$$

where n represents an integer referred to as the total Chern number or TKNN invariant. This integer is the summation of the Chern invariants over all occupied bands (n $=\sum_{m=1}^{N} n_m$).

This correlation, matching Equation 1.1, elucidates the robust quantization of the Hall conductivity [2, 7, 8]. Since n functions as a topological invariant, the alteration of σ_{xy} occurs exclusively during the transition to a new topological class. An example of a trivial insulator is vacuum (n = 0). In this scenario, n = 1 characterizes the Integer Quantum Hall State (IQHS). Consequently, deriving an IQHS from a trivial insulator through gradual adjustments in the Hamiltonian is unattainable. Eventually, the band gap must close, passing through zero to induce a modification in the topological invariant. At the interface between the trivial insulator (vacuum) and IQHS, a conducting chiral edge state emerges, depicted in Fig. 1.3(a) [2]. This edge state, protected by the fundamental concept of topology, contributes a one-dimensional (1D) band dispersion within the bulk band gap, as shown in Fig. 1.3(b) [2]. By altering the Hamiltonian in the vicinity of the surface, we can modify the dispersion of this 1D band. However, the difference between the number of left and right-moving channels (band dispersions intersecting the Fermi level with positive or negative group velocity) remains constant, determined by the "bulk-boundary correspondence" [2].

1.5 Quantum spin Hall state

Up to this point, our exploration has revealed the Integer Quantum Hall Effect (IQHE) as the sole topologically non-trivial electronic state, observed exclusively under a magnetic field in the absence of time reversal symmetry (TRS). In 1988, F. D. M. Haldane introduced a 2D honeycomb lattice model [9], laying the foundation for the potential existence of a topologically non-trivial electronic state in materials without the necessity of applying a magnetic field. Following this, in 2006, B. A. Bernevig, T. L. Hughes, and S.-C. Zhang anticipated the existence of such a state in the HgTe/CdTe quantum well [10], and this anticipation was eventually confirmed through experimental realization by L. W. Molenkamp and his collaborators in 2007 [11]. The discovery of the Quantum Spin Hall Insulator (QSHI) state in the HgTe quantum well was revolutionary and rep-

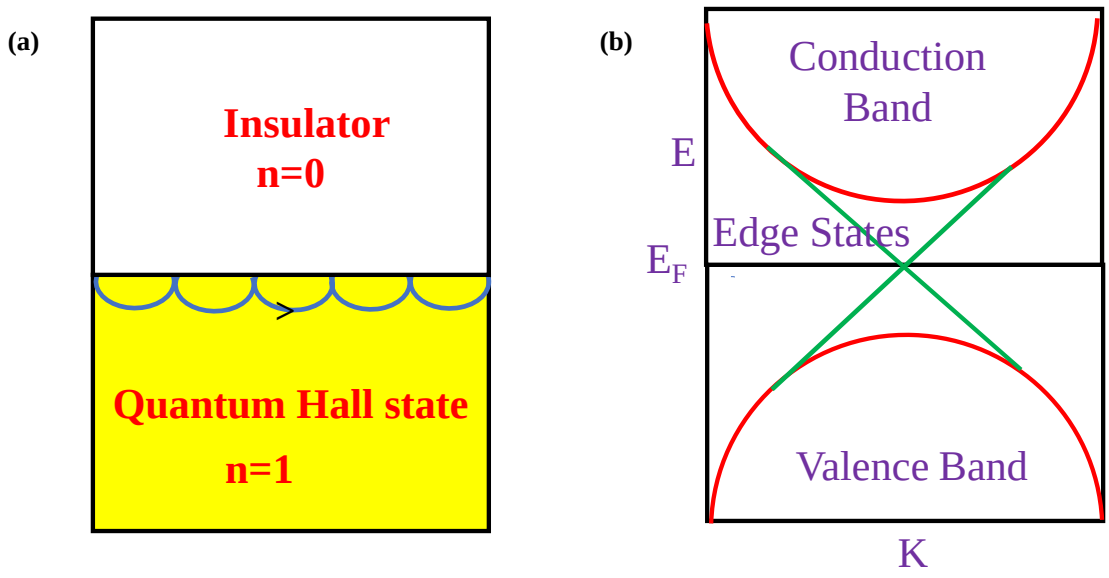

Figure 1.3: (a) Emergence of a chiral edge state at the boundary between a trivial insulator (vacuum) and a quantum Hall state. (b) This edge state is depicted by a one-dimensional band dispersion, linking the conduction and valence bands. Reproduced from Ref.[2]

resented a significant advancement in the study of noble topological phases of matter. The QSHI state can be understood as a composite of two Integer Quantum Hall States (IQHSs) for the up and down spins, as depicted in Fig. 1.4 [12]. The direction of the in-

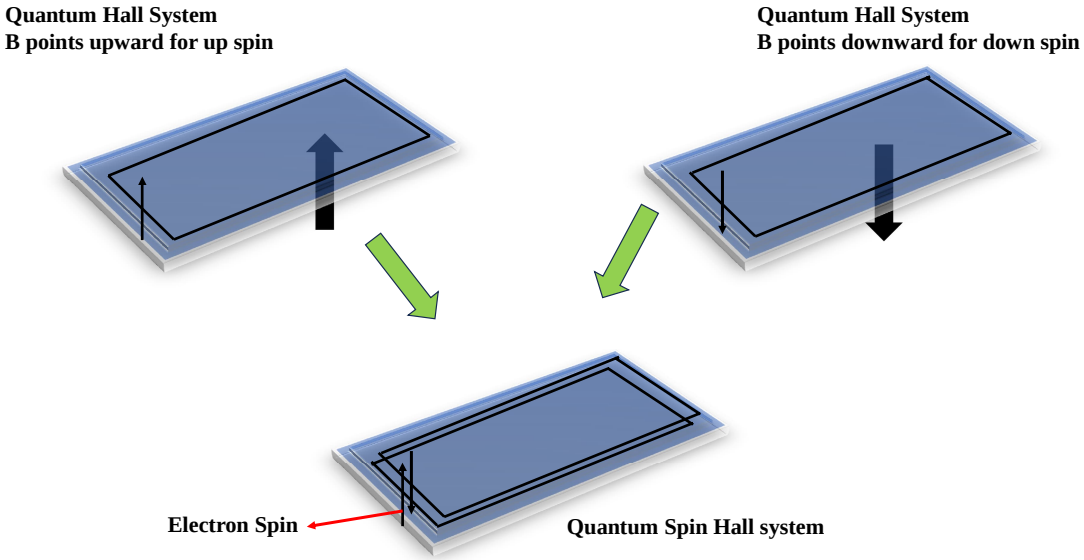

Figure 1.4: Illustration depicting a quantum spin Hall insulator (QSHI), characterized by a superposition of two integer quantum Hall states featuring counter-propagating chiral edge channels. Reproduced from Ref.[13]

trinsic magnetic field arising from spin-orbit coupling (SOC) determines whether spin-up

or spin-down states propagate in an anticlockwise or clockwise manner. Although there is no net charge flow, a net spin current is observed at the edge in QSHI. These up and down spin states act as time-reversal partners, ensuring that the combined state preserves time reversal symmetry (TRS). These edge states form two 1D bands protected by the TRS operation within the bulk band gap, intersecting the Fermi energy [14]. According to Kramer's theorem, the band crossing points are doubly degenerate in the presence of TRS. Remarkably, these edge states exhibit robustness against any form of disorder. The Quantum Spin Hall Insulator (QSHI), called as a 2D topological insulator (TI), exhibits topological distinctions from both the Integer Quantum Hall State (IQHS) and a normal insulator. Its unique characterization requires a novel topological invariant denoted as ν, referred to as the Z_2 invariant [15]. The value of ν is 0 for topologically trivial states and 1 for non-trivial states. The mathematical expression for the Z_2 invariant is given by

$$(-1)^{\nu_0} = \prod_{i=1}^{4} \frac{Pf[\omega(\Gamma_i)]}{\sqrt{\det[\omega(\Gamma_i)]}} \tag{1.4}$$

In this equation, Γ_i represents the four high symmetry points within the 2D Brillouin zone. $\omega_m n(\mathrm{k})$=<$\mathrm{u}_m(\mathrm{k})|\theta|\mathrm{u}_n(\text{-k})$> is a unitary matrix. Pf[$\omega(\Gamma_i)$] is Pfaffian. The determinant of the matrix $\omega(\Gamma_i)$equals the square of its Pfaffian. This implies, $\delta_i = \frac{Pf[\omega(\Gamma_i)]}{\sqrt{\det[\omega(\Gamma_i)]}} = \pm 1$. Consequently, the anti-unitary operator θ is the TRS operation by θ^2 = -1.

1.6 Three-dimensional Topological Insulator

In 2007, Liang Fu, C. L. Kane, and E. J. Mele demonstrated that the concept of 2D topological insulators (TI) could be extended to three dimensions (3D)[16]. However, for 3D TIs, there are four Z_2 topological invariants (ν_0 ; ν_1, ν_2, ν_3) instead of just one [16–18]. The definition of ν_0 is an extension of Equation 1.4 to include eight high symmetry points in the 3D Brillouin zone:

$$(-1)^{\nu_0} = \prod_{i=1}^{8} \delta_i \tag{1.5}$$

The remaining three invariants are determined by the multiplication of Δ_i values, where the corresponding Γ_i are located within the same plane. In the case of a trivial insulator, the topological invariant (ν_0 ; ν_1, ν_2, ν_3) is equal to (0; 0, 0, 0).

1.6.1 Weak topological insulator

One of the most straightforward methods for creating a 3D topological insulator (TI) involves stacking layers of 2D TIs with weak interlayer coupling along a specific axis [2]. The 1D edge states from each layer combine to generate a 2D conducting surface state. This surface state lacks protection from time-reversal symmetry (TRS) and can

be removed by introducing strong disorder. Such a configuration is termed a weak TI, characterized by $\nu_0 = 0$ and at least one of the other three invariants being 1 [16, 17]. However, in 2012, Z. Ringel et al. demonstrated that the surface state along specific cleavage planes in a weak TI is indeed impervious to random perturbations and preserves TRS [19].

1.6.2 Strong topological insulator

A robust topological insulator (TI) is distinguished by $\nu_0 = 1$, with an insulating bulk that coexists alongside robust metallic 2D surface states [16, 17]. A distinctive characteristic of this time-reversal symmetry (TRS)-protected surface state is "spin-momentum locking," meaning that the charge carriers' spin is consistently perpendicular their momentum [2, 3]. Consequently, non-magnetic impurities cannot cause backscattering, leading to nearly dissipationless charge conduction. Furthermore, a strong topological insulator (TI) is indicated by an odd number of TRS-invariant Kramers degenerate points enclosed by the surface Fermi energy contour [2, 3]. Of particular interest, the behavior of surface charge carriers is controlled by an effective Dirac-type Hamiltonian [2, 3]

$$H_{surface}(k_x, k_y) = \hbar v_F \hat{z} \times \vec{\sigma}.\vec{k} \tag{1.6}$$

where σ represents the Pauli spin vector. Hence, the surface state in a 3D topological insulator is depicted through linearly dispersing bands that intersect at Kramers degenerate Dirac points. This sharply contrasts to the conventional electronic systems, where energy bands adhere to a quadratic dispersion relation. Following the theoretical prediction by L. Fu and C. L. Kane [17], the emergence of the strong 3D topological insulator (TI) state was initially observed in $Bi_{1-x}Sb_x$ by M. Z. Hasan and his collaborators using angle-resolved photoemission spectroscopy (ARPES) [20]. Although the surface band structure of $Bi_{1-x}Sb_x$ is intricate, the bulk band structure exhibits a very small energy gap. Subsequently, H. Zhang et al. theoretically proposed a new series of compounds, Bi_2Se_3, Bi_2Te_3, and Sb_2Te_3 all featuring a single Dirac node at the surface and a sufficiently large bulk band gap [21]. Their predictions were subsequently validated by various experimental groups [22–24].

1.7 Classifications of the topological semi-metals

It is widely acknowledged that semimetals typically feature a low or negligible density of states in proximity to the Fermi level. Within this category, there exists a specific subset of materials where the three-dimensional (3D) Brillouin zone (BZ) is intersected or touched by both conduction and valence bands, resulting in a non-negligible density of states. Such band intersections often signify a topological phase transition and can be linked to a topological invariant [25]. Semimetals with these band intersections are

frequently distinguished topologically from others and are therefore labeled as "topological semimetals" [26–29]. In contemporary research, topological semimetals have emerged as a novel frontier in the realm of quantum materials. In the following sections, we provide a brief overview of various 3D topological semimetal phases of matter, including Weyl semimetals, Dirac semimetals, and nodal-line semimetals.

1.7.1 Weyl semimetal

Weyl semimetals (WSMs) represent a category of topological semimetals characterized by the presence of Weyl fermions as low-energy quasiparticle excitations [30]. In a WSM, two bands with singular degeneracy intersect at specific points known as Weyl nodes, dispersing linearly from each Weyl node in momentum space. Weyl fermions exhibit distinct chiralities, being either left-handed or right-handed. These chiralities of the Weyl nodes give rise to chiral charges, act as a source and sink of the Berry flux in momentum space. The surface projections of these Weyl nodes having different chiral charges are connected by the spin-polarized Fermi arcs [31]. The schematic of a WSM is shown in Fig. 1.5.

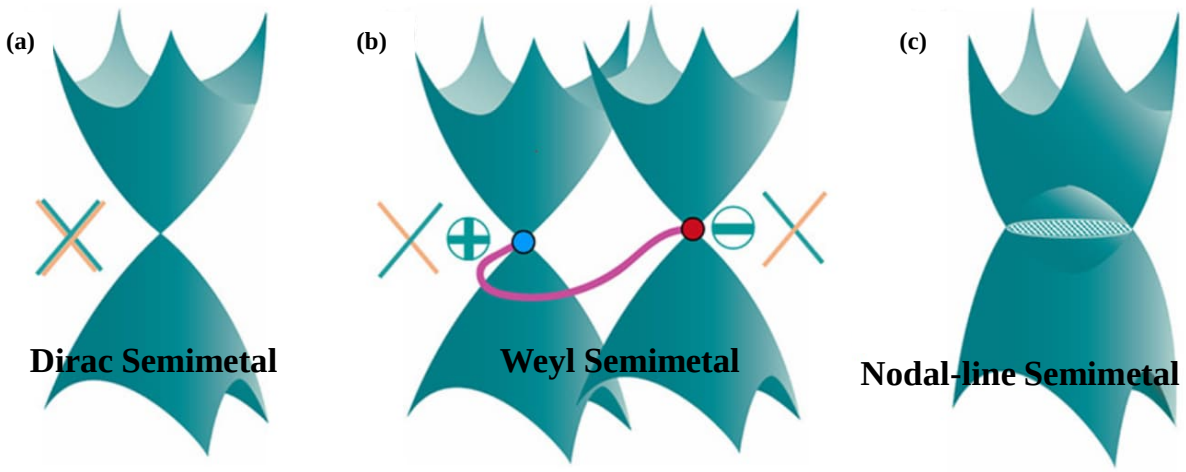

Figure 1.5: (a) Dirac, (b) Weyl, and (c) Nodal line semimetals are diagrammatically illustrated. In a Dirac semimetal, all bands exhibit 4-fold degeneracy, while in a Weyl semimetal, degeneracy is broken due to the breaking of either inversion or time-reversal symmetry, so it exhibits 2-fold degeneracy. The opposite chirality of the Weyl points is indicated by the positive and negative signs. The Weyl points are connected through Fermi arcs, illustrated by pink lines. In nodal line semimetals, band crossing happens as a line or ring, generating a two-dimensional topological surface state, known as the drumhead surface state. Taken from Ref.[31]

Real materials hosting the Weyl nodes are typically distinguished into two categories: inversion-symmetry breaking (IS) WSMs and time-reversal symmetry (TRS) breaking WSMs. For instance an IS breaking WSM is found in the noncentrosymmetric TaAs family of crystals [32–36]. WSMs with broken TRS are generally observed in ferromag-

netic materials such as pyrochlore iridate [37], $Co_3Sn_2S_2$[38, 39], and Heuslers [40, 41]. The electrical and magneto-transport properties of various WSM materials have been extensively studied. The linear band dispersion and non-trivial phases in the electronic band structure offer an ideal platform for exploring diverse non-trivial topological phenomena in different WSM materials.

1.7.2 Dirac semimetal

Dirac semimetals (DSMs) contain Dirac fermions as low-energy quasiparticle excitations [30]. Within a DSM, two 2-fold degenerate bands intersect to create a Dirac node, then disperse linearly in momentum space . Each Dirac nodes can be thought of as two pairs of degenerate Weyl nodes with different chairalities [31] (wherein the Dirac node possesses zero chiral charges). A depiction of a DSM is presented in Fig. 1.5(b) . As a pair of degenerate Weyl nodes with different chiralities is often unstable and may eliminate each other, extra crystalline point group symmetries are needed to establish a stable DSM phase [42]. One strategy involves uniaxial rotational symmetry. Typical, DSMs of this types are discovered in Na_3Bi [43], Cd_3As_2[44]. Non-symmorphic symmetries offer alternative route to achieve the Dirac semimetal phase in material. Examples of these type of materials include distorted spinels [45] and β- BiO_2 [46].

Two surface projections of the bulk Dirac points are connected by spin-polarized Fermi arcs, shown in Fig. 1.6.

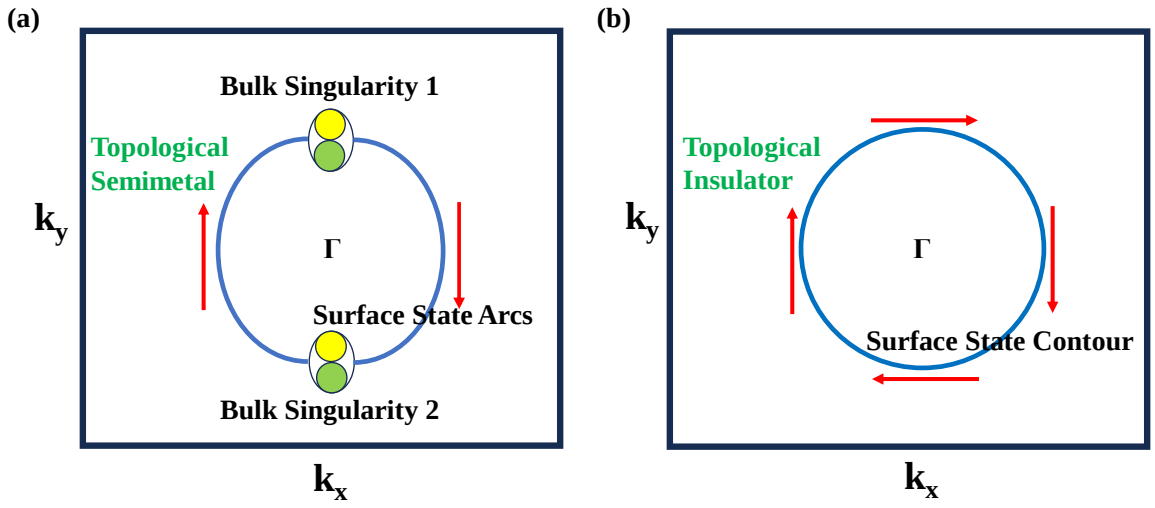

Figure 1.6: (a) Each Dirac node can be viewed as two degenerate Weyl nodes (yellow and green areas). The red arrow suggests the spin polarization of the surface states. (b) This edge state is depicted by a one-dimensional band dispersion, linking the conduction and valence bands. Reproduced from Ref.[47]

1.7.3 Nodal-line semimetal

Dirac and Weyl semimetals have a single point of intersection where their valence and conduction bands meet. However, there is a more general case in which this intersection happens around a ring or line protected by particular crystalline symmetries. Under such circumstances, they are referred to as topological nodal-line or nodal-ring semimetals[30], illustrated in Fig. 1.5(c). Owing to spin-orbit coupling, numerous Weyl and Dirac semimetals arise from such nodal lines, underlining the broad applicability of this nodal structure. These exotic states necessitate additional crystalline symmetries for stabilization, often achieved through mirror reflections [48]. The degeneracy of the line intersections can either be 2-fold, known as Weyl semimetal, or 4-fold, as depicted in the case of a Dirac semimetal.

1.8 Anomalous Hall effect

In 1879, Edwin Hall made a significant breakthrough by discovering that a current-carrying conductor experiences the Lorentz force, which pushes its electrons towards one side of the conductor [49]. Later, he observed that this effect, was ten times stronger in ferromagnetic iron compared to nonmagnetic conductors [50]. Hall's observation of this enhanced effect in ferromagnetic conductors eventually became known as the anomalous Hall effect (AHE). Despite the AHE being identified over a century ago, its origins in magnetic materials continue to be among the most intriguing aspects of condensed matter physics. This complexity arises because the AHE problem involves concepts rooted in topology and geometry, which have only recently been developed. Early researchers grappled with ideas that would not be fully understood and defined until much later, such as the Berry phase [51]. What is now recognized as the Berry curvature, previously referred to as Luttinger's "anomalous velocity," naturally emerged in the initial microscopic understanding of the AHE proposed by Karplus and Luttinger [52].

In the early stages, experimental researchers noted a fundamental difference in the dependence of Hall resistivity ρ_{xy} on the applied perpendicular field B_z between ferromagnetic and nonmagnetic conductors. In nonmagnetic conductors, ρ_{xy} increases linearly with B_z, as predicted by the Lorentz force. However, in ferromagnets, ρ_{xy} initially increases sharply with weak B_z after reaching a saturation value it is completely independent of B_z. Subsequently, Pugh (1930) and Pugh and Lippert (1932) established an empirical relationship between ρ_{xy} , B_z, and M_z[53, 54],

$$\rho_{xy} = R_0 B_z + R_s M_z \tag{1.7}$$

applicable to a broad spectrum of materials under external magnetic fields. The second part represents the contribution to the Hall effect induced by spontaneous magnetization. In contrast to R_0, which was previously understood to be mainly influenced

by carrier density, R_s was found to be somewhat influenced by certain material-specific factors, including the longitudinal resistivity ρ_{xx}. In 1954, Karplus and Luttinger (KL) formulated a hypothesis concerning the anomalous Hall effect (AHE), a pivotal advancement that significantly contributed to our comprehension of this phenomenon [52]. KL postulated that electrons gain an additional component to their velocity when subjected to an external field within a solid. This anomalous velocity which is perpendicular to the electric field, could potentially contribute to the Hall effects. In ferromagnetic conductors, the summation of the anomalous velocity over all occupied band states may not cancel out, suggesting a contribution to the Hall conductivity σ_{xy}. This contribution is now known as the intrinsic contribution to the AHE, as it primarily depends on the band structure and remains largely unaffected by scattering.

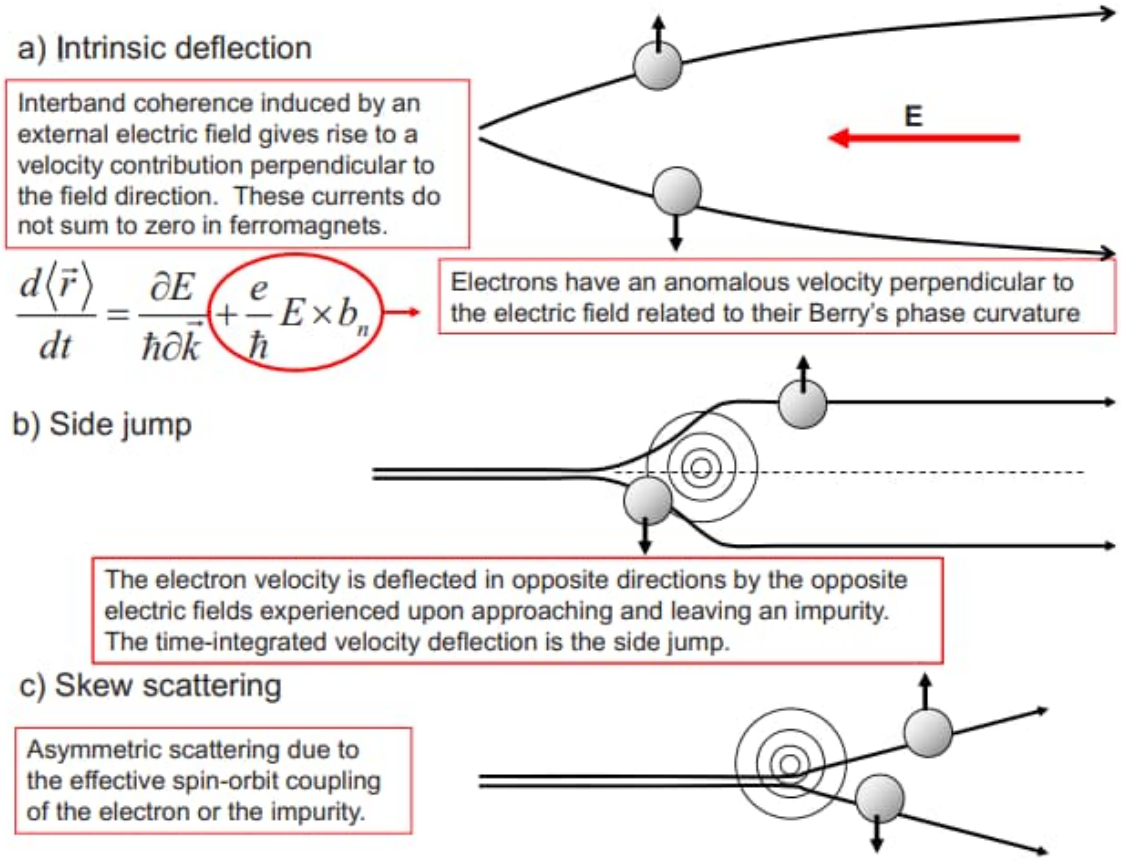

Figure 1.7: This diagram demonstrates the three primary mechanisms responsible for generating an anomalous Hall effect (AHE). In any magnetic material, these three mechanisms contribute to the Hall effect mechanism . Adapted from Ref.[55]

The inherent anomalous Hall effect (AHE) contributes to ρ_{xy} to approximately $\frac{\sigma_{xy}}{\sigma_{xx}^2}$ when the conductivity tensor undergoes reversal, rendering it proportionate to ρ_{xx}^2[55]. The anomalous velocity solely relies on the Hamiltonian of an ideal crystal and can be associated with alterations in the phase of Bloch state wave packets as they evolve in momentum space within a crystal under the influence of an electric field [56]. At the moment, the Berry phase effect of occupied electronic Bloch states clarifies the intrinsic

AHE. [57, 58].

The primary limitation of the intrinsic KL theory was its failure to demonstrate the evidence of scattering from disorder in the Hall response contribution. Conversely, semiclassical AHE theories proposed by Smit and Berger focused on the impact of disorder scattering in imperfect crystals [59–61]. Smit suggested that the predominant source of AHE currents stemmed from asymmetric skew scattering induced by impurities arising from spin-orbit interaction. In this AHE model, ρ_{xy} was proposed to be proportional to ρ_{xx}. On the other hand, Berger argued that the fundamental origin of AHE currents arise from the side jump experienced by quasiparticles when scattered by impurities with spin-orbit coupling. The side-jump AHE current emerged as a result of both the side jumps occurring per scattering event and the scattering rate. It shows $\rho_{xy} \propto \rho_{xx}^2$ with an exponent similar to that of the intrinsic KL mechanism. However, the contribution from side jumps is generally minimal for ferromagnetic materials [41, 62, 63]. Fig. 1.7 schematically illustrates the three distinct mechanisms of AHE.

1.9 Different types of Magnetic phenomena

1.9.1 Exchange Bias

In 1956, Meiklejohn and Bean invented the new type of magnetic anisotropy [64]. They observed a shift in the magnetic data along the field axis while cooling the Co fine particles surrounded by CoO in a static magnetic field [64, 65]. Originally observed in systems consisting both ferromagnetic (FM) (spins are aligned in the same direction) and antiferromagnetic (AFM) materials (spins are aligned antiparallel to each other), this phenomenon was subsequently identified in canted antiferromagnets [66], spin glass systems [67], and disordered magnetic components [68]. When the sample is cooled through the Neel temperature (T_N) under static magnetic field, the exchange bias (EB) emerges as unidirectional anisotropy by providing a single preferred direction for magnetization. Horizontal and vertical shifts are observed in the field dependent magnetization data, displayed in Fig. 1.8(b),(c). Consequently, Sin θ component emerges in the torque curve. These are typical manifestations of the exchange bias effect[69]. If the material is cooled without the presence of a magnetic field, exchange bias does not appear in the system. Specifically, the pinned ferromagnetic layer does not arise during that period. This is elaborated in Fig. 1.8(a),(c).

Phenomenology of exchange bias

The essential condition for the presence of exchange bias (EB) is the T_c of the FM should be higher than T_N of the AFM phase. For $T_N < T < T_c$, FM spins align along field direction whereas AFM spins exhibit random orientation. For $T < T_N$, AFM spins align ferromagnetically owing to the interaction at the interface and other AFM spins conform

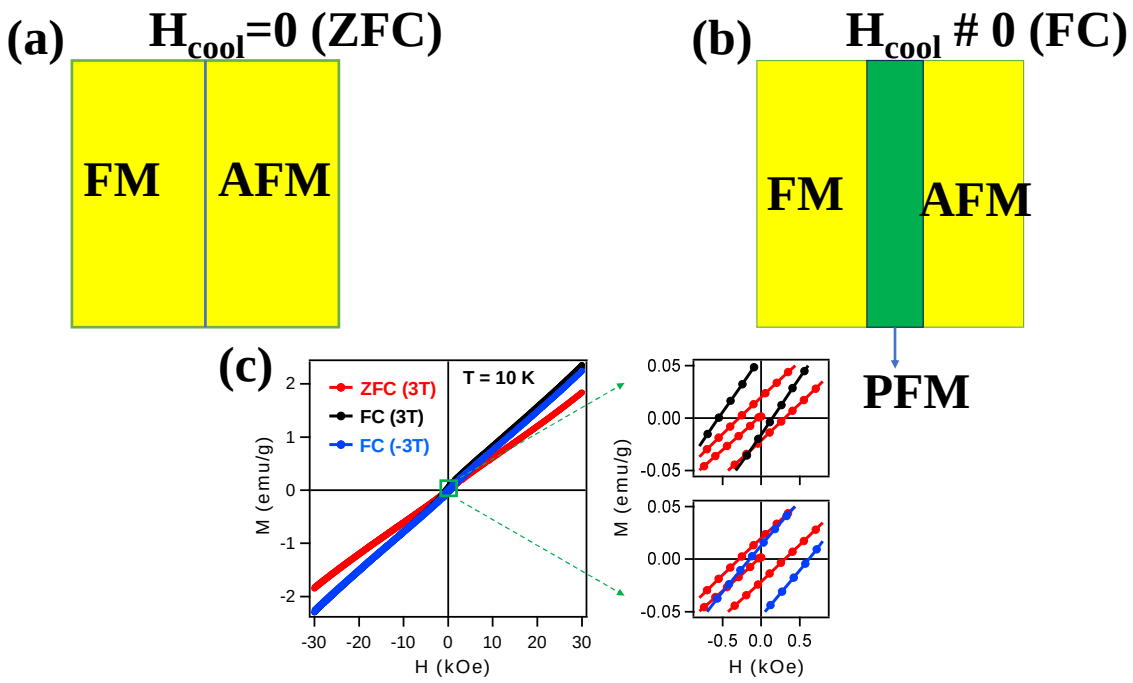

Figure 1.8: Diagram illustrating the exchange bias (EB) effect resulting from field cooling in (a) a bilayer consisting FM/AFM structure and (b) a bilayer structure comprising FM/AFM structure with new pinned ferromagnetic (PFM) layer at the interface; (c) absence of shift during zero field cooled(zfc) and shifts in the loop (field cooled) (fc).

to the AFM order. Upon applying a field in the opposite direction, ferromagnetic (FM) spins will rotate along the field direction. However, due to the coupling with AFM layer, a strong reversing field is required to overcome this coupling. Consequently, a significant coercive field (H_C) is achieved. As we return back to the positive field direction, FM spins revert back at lower field strength, resulting in a horizontal shift of the hysteresis loop away from the origin, refers as the exchange bias field (H_{EB}).

The H_{EB} and H_C field is defined as,

$$H_{EB} = -|H_1 + H_2|/2 \tag{1.8}$$

$$H_C = |H_1 - H_2|/2 \tag{1.9}$$

where, H_1, H_2 are the left and right cut-off field respectively at which magnetization becomes zero.

Training Effect

Numerous intriguing experimental properties have emerged, posing significant challenges to the exchange bias mechanism. A category of these investigations includes rotational hysteresis as a function of cycle counts. The training effect is an important intrinsic property of EB systems. The change of the shape of hysteresis loop and the corresponding

decrease of loop shift upon consecutive field cycling after field cooling for a particular temperature known as training effect. In 1966 Paccard et al discovered this phenomenon in three systems Co-CoO, NiFe-NiFeMn, and NiFe-Cr_2O_3 showing FM-AFM coupling [70]. They proposed that the following equation could account for the H_{EB} decrease with increasing loop index n.

$$(H_{EB}^1 - H_{EB}^n) \propto 1/\sqrt{n} \tag{1.10}$$

here, n indicates the loop index number. The domain structure of the antiferromagnet (AFM) within the mixed AFM/FM phase during successive cycles could be the underlying cause of this phenomenon [71].

1.9.2 Magnetocaloric Effect

The phenomenon known as the 'Magnetocaloric Effect' involves the alternation of temperature of a magnetic substance under external magnetic field. This effect, abbreviated as MCE, can be harnessed for cooling or refrigeration purposes. Nowadays, refrigeration technology proves highly beneficial across a wide temperature spectrum, from room temperature to ultra-low temperatures. Room temperature refrigerants find application in domestic and industrial settings, such as air conditioning. Conversely, low-temperature refrigerants are utilized in diverse fields like food and medicine storage in supermarkets, industrial processes like gas liquefaction, superconducting coils, medical and space sciences, as well as in research labs for studying various physical properties at extremely low temperatures.

These magnetic refrigerants offer several advantages over conventional gas compressor refrigerants. Unlike conventional refrigerants that emit harmful ozone-depleting greenhouse gases like chlorofluorocarbons (CFCs), magnetic refrigerants do not pose such environmental threats. Additionally, magnetic refrigerants are more efficient and compact compared to conventional ones.

Two fundamental parameters of the Magnetocaloric Effect are the isothermal magnetic entropy change ($\Delta\ S_m$) and adiabatic temperature change ($\Delta\ T_{ad}$).

As the Magnetocaloric Effect (MCE) relies on the magnetic field response of materials, understanding the behavior of these materials under magnetic influence is crucial before employing them in magnetic refrigeration technology. Magnetic materials inherently possess two forms of internal excitation energy: phonon excitation, associated with lattice degree of freedom, and magnetic excitation, linked to spin degree of freedom. In an isolated system, the total entropy (S) of a magnetic material remains constant and comprises two components: lattice entropy (S_L) and magnetic entropy (S_M), denoted as $S = S_L + S_M$.Fig. 1.9 illustrates the schematic representation of a standard magnetic refrigeration system.

Adiabatic magnetization: In the absence of the magnetic field, the spins within

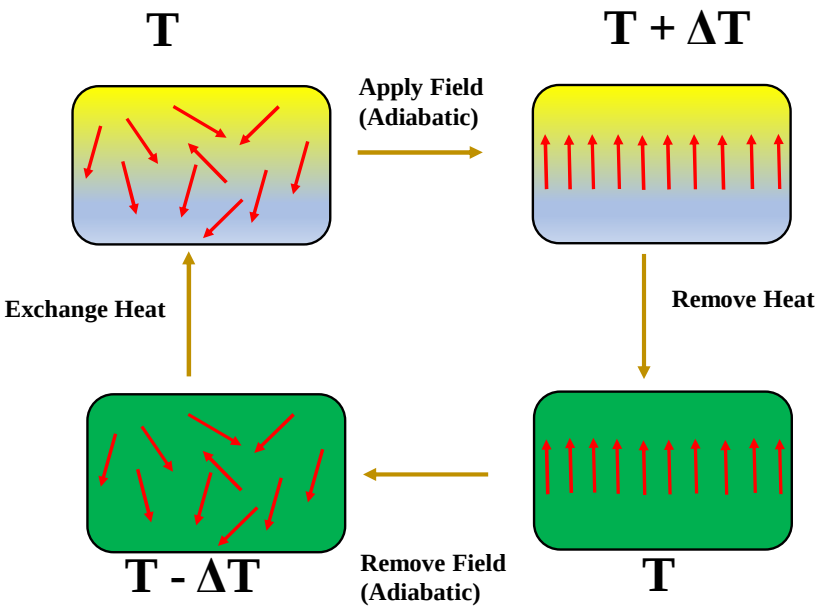

Figure 1.9: Illustrative depiction of the magnetic refrigeration cycle's framework. Reproduced from Ref.[72]

the magnetic material exhibit random orientations at an initial temperature T. Under external magnetic field H, the magnetic moments orient themselves with the direction of the magnetic field. Consequently, magnetic entropy decreases, while, concurrently, to maintain the system's total entropy constant, lattice entropy increases. This leads to the material's temperature rising to T + ΔT. This phenomenon is referred to as adiabatic magnetization, as the magnetic field is applied under adiabatic conditions.

Isomagnetic enthalpic transfer: During the second step, the elevated temperature ΔT is reduced using a coolant liquid such as helium or cold water, restoring the temperature to T. Throughout this stage, the field remains constant, thereby labeling the process as isomagnetic enthalpic transfer.

Adiabatic demagnetization: Next, in the third step, the external field is eliminated, initiating an adiabatic demagnetization process. During this process, the magnetic moments revert to a random orientation, leading to an increase in magnetic entropy while simultaneously causing a decrease in lattice entropy. Consequently, the material's temperature decreases, returning to T - ΔT.

Isomagnetic entropic transfer: In the last stage, a hot material is linked with the Magnetocaloric Effect (MCE) material requiring cooling. Consequently, the temperature of the hot material is decreased by the magnitude of ΔT through the refrigerant material. Throughout this process, the magnetic field remains constant to prevent heat reabsorption, thus defining it as an isomagnetic procedure.

Thermodynamics of the magnetocaloric effect

As entropy is a state function, its total differential can be expressed as:

$$dS = (\frac{\partial S}{\partial T})_{p,H}dT + (\frac{\partial S}{\partial P})_{T,H}dP + (\frac{\partial S}{\partial H})_{p,T}dH \tag{1.11}$$

Under isobaric (dp=0) and isothermal (dT=0) conditions, the change in entropy depends solely on the magnetic field. According to the Maxwell thermodynamic relation, the entropy change of a magnetic material under the magnetic field H is associated with its magnetization M with respect to temperature T as follows:

$$(\frac{\partial S}{\partial H})_T = (\frac{\partial M}{\partial T})_H \tag{1.12}$$

Consequently, upon integrating the magnetic entropy change, ΔS_M(T; H), under isobaric and isothermal conditions, it is shown by:

$$\Delta S_M(T,H) = S_M(T,H) - S_M(T,0) = \int_0^H (\frac{\partial M}{\partial T})_H dH \tag{1.13}$$

This is because the magnetic entropy change, ΔS_M(T; H), is directly proportional to the derivative of magnetization with respect to temperature at a constant field.

1.10 Outline of the PhD thesis

My thesis aims to synthesize high-quality single crystals of various topological systems and investigate their structural, electrical transport, and magnetic properties. Therefore, for my Ph.D. thesis, I have focused on growing $Cr_{0.79}Se$, $FeCr_2Te_4$, and $HoAl_2Si$ due to their intriguing topological properties.

Initially, We have grown polycrystals of $Cr_{0.79}Se$ which exhibits a paramagnetic (PM) to antiferromagnetic (AFM) transition below 225K. Recently, AFM metals with non-collinear spin textures have garnered attention as potential candidates for inducing the anomalous Hall effect (AHE) via Berry curvature. This prompted us to revisit the system's structural, electrical, and magnetic characteristics. Our X-ray diffraction (XRD) analysis revealed a NiAs-type structure for $Cr_{0.79}Se$. Additionally, we observed that this structure remains stable at temperatures as high as 600°C based on the XRD data. Notably, we observed exchange bias below 100 K, arising from the interaction between ferro- and antiferromagnetic phases.

We also grew $FeCr_2Te_4$ single crystals, predicted to host a Weyl node below the Fermi level (44 meV below). However, neither the material's scattering processes nor the impact of a magnetic field on these coefficients have been thoroughly explored. Furthermore, there is a lack of comprehensive analysis regarding the magnetotransport properties of $FeCr_2Te_4$. Our study aims to address these gaps by focusing on the structural, mag-

netic, electrical transport, and magnetotransport properties of $FeCr_2Te_4$ single crystals. Particularly, we emphasize the behavior of magnetoresistance (MR) near the critical temperature.

Theoretical predictions suggest the existence of a novel type of Weyl semimetal state in the RAlGe (R = rare-earth) family, breaking both time-reversal and inversion symmetry. Specifically, $R_2Al_3Si_2$ (R = Tb, Dy, Ho, Er, Tm) crystallizes in a C-centered monoclinic $Y_2Al_3Si_2$-type crystal structure. In particular, the Ho-Al-Si system appears to stabilize in $Ho_2Al_3Si_2$ and $HoSiAl_2$ phases. We have successfully grown $HoSiAl_2$ single crystals and characterized their physical properties through measurements of magnetic susceptibility, electrical resistivity, Hall effect, magnetoresistance, and electronic band structure calculations.

References

[1] M. Nakahara, Geometry, topology and physics, CRC press, 2018.

[2] M. Z. Hasan, C. L. Kane, Colloquium: topological insulators, Reviews of modern physics 82 (2010) 3045.

[3] X.-L. Qi, S.-C. Zhang, Topological insulators and superconductors, Reviews of modern physics 83 (2011) 1057.

[4] K. v. Klitzing, G. Dorda, M. Pepper, New method for high-accuracy determination of the fine-structure constant based on quantized hall resistance, Phys. Rev. Lett. 45 (1980) 494–497.

[5] K. Von Klitzing, Developments in the quantum Hall effect, Philosophical Transactions of the Royal Society A: Mathematical, Physical and Engineering Sciences 363 (2005) 2203–2219.

[6] D. J. Thouless, M. Kohmoto, M. P. Nightingale, M. den Nijs, Quantized Hall conductance in a two-dimensional periodic potential, Physical review letters 49 (1982) 405.

[7] X.-L. Qi, S.-C. Zhang, Topological insulators and superconductors, Reviews of modern physics 83 (2011) 1057.

[8] H. Zhang, S.-C. Zhang, Topological insulators from the perspective of first-principles calculations, physica status solidi (RRL)–Rapid Research Letters 7 (2013) 72–81.

[9] F. D. M. Haldane, Model for a quantum Hall effect without landau levels: Condensed-matter realization of the" parity anomaly", Physical review letters 61 (1988) 2015.

[10] B. A. Bernevig, T. L. Hughes, S.-C. Zhang, Quantum spin Hall effect and topological phase transition in HgTe quantum wells, science 314 (2006) 1757–1761.

[11] M. Konig, S. Wiedmann, C. Brune, A. Roth, H. Buhmann, L. W. Molenkamp, X.-L. Qi, S.-C. Zhang, Quantum spin Hall insulator state in HgTe quantum wells, Science 318 (2007) 766–770.

[12] S. Murakami, Phase transition between the quantum spin Hall and insulator phases in 3d: emergence of a topological gapless phase, New Journal of Physics 9 (2007) 356.

[13] S. Murakami, Phase transition between the quantum spin hall and insulator phases in 3d: emergence of a topological gapless phase, New Journal of Physics 9 (2007) 356.

[14] X.-L. Qi, S.-C. Zhang, The quantum spin Hall effect and topological insulators, Physics Today 63 (2010) 33–38.

[15] C. L. Kane, E. J. Mele, Z 2 topological order and the quantum spin Hall effect, Physical review letters 95 (2005) 146802.

[16] L. Fu, C. L. Kane, E. J. Mele, Topological insulators in three dimensions, Physical review letters 98 (2007) 106803.

[17] L. Fu, C. L. Kane, Topological insulators with inversion symmetry, Physical Review B 76 (2007) 045302.

[18] J. E. Moore, L. Balents, Topological invariants of time-reversal-invariant band structures, Physical Review B 75 (2007) 121306.

[19] Z. Ringel, Y. E. Kraus, A. Stern, Strong side of weak topological insulators, Physical Review B 86 (2012) 045102.

[20] D. Hsieh, D. Qian, L. Wray, Y. Xia, Y. S. Hor, R. J. Cava, M. Z. Hasan, A topological dirac insulator in a quantum spin Hall phase, Nature 452 (2008) 970–974.

[21] H. Zhang, C.-X. Liu, X.-L. Qi, X. Dai, Z. Fang, S.-C. Zhang, Topological insulators in Bi_2Se_3, Bi_2Te_3 and Sb_2Te_3 with a single dirac cone on the surface, Nature physics 5 (2009) 438–442.

[22] Y. Chen, J. G. Analytis, J.-H. Chu, Z. Liu, S.-K. Mo, X.-L. Qi, H. Zhang, D. Lu, X. Dai, Z. Fang, et al., Experimental realization of a three-dimensional topological insulator, Bi_2Te_3, science 325 (2009) 178–181.

[23] Y. Xia, D. Qian, D. Hsieh, L. Wray, A. Pal, H. Lin, A. Bansil, D. Grauer, Y. S. Hor, R. J. Cava, et al., Observation of a large-gap topological-insulator class with a single dirac cone on the surface, Nature physics 5 (2009) 398–402.

[24] D. Hsieh, Y. Xia, D. Qian, L. Wray, F. Meier, J. Dil, J. Osterwalder, L. Patthey, A. Fedorov, H. Lin, et al., Observation of time-reversal-protected single-dirac-cone topological-insulator states in Bi_2 Te_3 and Sb_2 Te_3, Physical review letters 103 (2009) 146401.

[25] Z. Wang, Y. Sun, X.-Q. Chen, C. Franchini, G. Xu, H. Weng, X. Dai, Z. Fang, Dirac semimetal and topological phase transitions in A_3 Bi (A= Na, K, Rb), Physical Review B 85 (2012) 195320.

[26] C. Fang, H. Weng, X. Dai, Z. Fang, Topological nodal line semimetals, Chinese Physics B 25 (2016) 117106.

[27] M. Z. Hasan, S.-Y. Xu, I. Belopolski, S.-M. Huang, Discovery of weyl fermion semimetals and topological fermi arc states, Annual Review of Condensed Matter Physics 8 (2017) 289–309.

[28] B. Yan, C. Felser, Topological materials: Weyl semimetals, Annual Review of Condensed Matter Physics 8 (2017) 337–354.

[29] N. Armitage, E. Mele, A. Vishwanath, Weyl and dirac semimetals in three-dimensional solids, Reviews of Modern Physics 90 (2018) 015001.

[30] J. Hu, S.-Y. Xu, N. Ni, Z. Mao, Transport of topological semimetals, Annual Review of Materials Research 49 (2019) 207–252.

[31] N. Kumar, S. N. Guin, K. Manna, C. Shekhar, C. Felser, Topological quantum materials from the viewpoint of chemistry, Chemical Reviews 121 (2020) 2780–2815.

[32] B. Lv, H. Weng, B. Fu, X. P. Wang, H. Miao, J. Ma, P. Richard, X. Huang, L. Zhao, G. Chen, et al., Experimental discovery of weyl semimetal TaAs, Physical Review X 5 (2015) 031013.

[33] H. Weng, C. Fang, Z. Fang, B. A. Bernevig, X. Dai, Weyl semimetal phase in noncentrosymmetric transition-metal monophosphides, Physical Review X 5 (2015) 011029.

[34] S.-M. Huang, S.-Y. Xu, I. Belopolski, C.-C. Lee, G. Chang, B. Wang, N. Alidoust, G. Bian, M. Neupane, C. Zhang, et al., A weyl fermion semimetal with surface fermi arcs in the transition metal monopnictide TaAs class, Nature communications 6 (2015) 7373.

[35] S.-Y. Xu, I. Belopolski, N. Alidoust, M. Neupane, G. Bian, C. Zhang, R. Sankar, G. Chang, Z. Yuan, C.-C. Lee, et al., Discovery of a weyl fermion semimetal and topological fermi arcs, Science 349 (2015) 613–617.

[36] L. Yang, Z. Liu, Y. Sun, H. Peng, H. Yang, T. Zhang, B. Zhou, Y. Zhang, Y. Guo, M. Rahn, et al., Discovery of a weyl semimetal in non-centrosymmetric compound TaAs, arXiv preprint arXiv:1507.00521 (2015).

[37] X. Wan, A. M. Turner, A. Vishwanath, S. Y. Savrasov, Topological semimetal and fermi-arc surface states in the electronic structure of pyrochlore iridates, Physical Review B 83 (2011) 205101.

[38] E. Liu, Y. Sun, N. Kumar, L. Muechler, A. Sun, L. Jiao, S.-Y. Yang, D. Liu, A. Liang, Q. Xu, et al., Giant anomalous Hall effect in a ferromagnetic kagome-lattice semimetal, Nature physics 14 (2018) 1125–1131.

[39] Q. Wang, Y. Xu, R. Lou, Z. Liu, M. Li, Y. Huang, D. Shen, H. Weng, S. Wang, H. Lei, Large intrinsic anomalous Hall effect in half-metallic ferromagnet $Co_3Sn_2S_2$ with magnetic weyl fermions, Nature communications 9 (2018) 1–8.

[40] K. Manna, L. Muechler, T.-H. Kao, R. Stinshoff, Y. Zhang, J. Gooth, N. Kumar, G. Kreiner, K. Koepernik, R. Car, et al., From colossal to zero: controlling the anomalous Hall effect in magnetic heusler compounds via berry curvature design, Physical Review X 8 (2018) 041045.

[41] P. Li, J. Koo, W. Ning, J. Li, L. Miao, L. Min, Y. Zhu, Y. Wang, N. Alem, C.-X. Liu, et al., Giant room temperature anomalous Hall effect and tunable topology in a ferromagnetic topological semimetal Co_2MnAl, Nature communications 11 (2020) 3476.

[42] B.-J. Yang, N. Nagaosa, Classification of stable three-dimensional dirac semimetals with nontrivial topology, Nature communications 5 (2014) 4898.

[43] Z. Liu, J. Jiang, B. Zhou, Z. Wang, Y. Zhang, H. Weng, D. Prabhakaran, S. K. Mo, H. Peng, P. Dudin, et al., A stable three-dimensional topological dirac semimetal Cd_3As_2, Nature materials 13 (2014) 677–681.

[44] M. Neupane, S.-Y. Xu, R. Sankar, N. Alidoust, G. Bian, C. Liu, I. Belopolski, T.-R. Chang, H.-T. Jeng, H. Lin, et al., Observation of a three-dimensional topological dirac semimetal phase in high-mobility Cd_3As_2, Nature communications 5 (2014) 3786.

[45] J. A. Steinberg, S. M. Young, S. Zaheer, C. Kane, E. Mele, A. M. Rappe, Bulk dirac points in distorted spinels, Physical review letters 112 (2014) 036403.

[46] S. M. Young, S. Zaheer, J. C. Teo, C. L. Kane, E. J. Mele, A. M. Rappe, Dirac semimetal in three dimensions, Physical review letters 108 (2012) 140405.

[47] S.-Y. Xu, C. Liu, S. K. Kushwaha, R. Sankar, J. W. Krizan, I. Belopolski, M. Neupane, G. Bian, N. Alidoust, T.-R. Chang, et al., Observation of fermi arc surface states in a topological metal, Science 347 (2015) 294–298.

[48] G. Chang, S.-Y. Xu, X. Zhou, S.-M. Huang, B. Singh, B. Wang, I. Belopolski, J. Yin, S. Zhang, A. Bansil, et al., Topological hopf and chain link semimetal states and their application to Co_2MnGa, Physical review letters 119 (2017) 156401.

[49] E. H. Hall, et al., On a new action of the magnet on electric currents, American Journal of Mathematics 2 (1879) 287–292.

[50] E. Hall, E. London, Dublin philos. mag, J. Sci 12 (1881) 157.

[51] M. V. Berry, Quantal phase factors accompanying adiabatic changes, Proceedings of the Royal Society of London. A. Mathematical and Physical Sciences 392 (1984) 45–57.

[52] R. Karplus, J. Luttinger, Hall effect in ferromagnetics, Physical Review 95 (1954) 1154.

[53] E. M. Pugh, Hall effect and the magnetic properties of some ferromagnetic materials, Physical Review 36 (1930) 1503.

[54] E. M. Pugh, T. Lippert, Hall emf and intensity of magnetization, Physical Review 42 (1932) 709.

[55] N. Nagaosa, J. Sinova, S. Onoda, A. H. MacDonald, N. P. Ong, Anomalous Hall effect, Reviews of modern physics 82 (2010) 1539.

[56] C.-K. Chiu, A. P. Schnyder, Classification of reflection-symmetry-protected topological semimetals and nodal superconductors, Physical Review B 90 (2014) 205136.

[57] T. Jungwirth, Q. Niu, A. MacDonald, Anomalous Hall effect in ferromagnetic semiconductors, Physical review letters 88 (2002) 207208.

[58] N. Nagaosa, Anomalous Hall effect—a new perspective—, Journal of the Physical Society of Japan 75 (2006) 042001–042001.

[59] J. Smit, The spontaneous Hall effect in ferromagnetics i, Physica 21 (1955) 877–887.

[60] J. Smit, The spontaneous Hall effect in ferromagnetics ii, Physica 24 (1958) 39–51.

[61] L. Berger, Side-jump mechanism for the Hall effect of ferromagnets, Physical Review B 2 (1970) 4559.

[62] S. Roy, R. Singha, A. Ghosh, A. Pariari, P. Mandal, Anomalous Hall effect in the half-metallic heusler compound Co_2TiX (x= Si, Ge), Physical Review B 102 (2020) 085147.

[63] G. K. Shukla, J. Sau, N. Shahi, A. K. Singh, M. Kumar, S. Singh, Anomalous Hall effect from gapped nodal line in the Co_2FeGe heusler compound, Physical Review B 104 (2021) 195108.

[64] W. H. Meiklejohn, C. P. Bean, New magnetic anisotropy, Physical review 102 (1956) 1413.

[65] W. H. Meiklejohn, C. P. Bean, New magnetic anisotropy, Physical Review 105 (1957) 904.

[66] S. K. Pradhan, B. Dalal, S. De, Exchange bias effect in a finite site disordered canted antiferromagnet, Journal of Physics: Condensed Matter 30 (2018) 365801.

[67] R. C. Sahoo, Y. Takeuchi, A. Ohtomo, Z. Hossain, Exchange bias and spin glass states driven by antisite disorder in the double perovskite compound $LaSrCoFeO_6$, Phys. Rev. B 100 (2019) 214436.

[68] P. Mohanty, S. Marik, R. P. Singh, Magnetism and exchange bias properties in Ba_2ScRuO_6, Magnetochemistry 9 (2023) 144.

[69] W. Meiklejohn, Exchange anisotropy—a review, Journal of Applied Physics 33 (1962) 1328–1335.

[70] D. Paccard, C. Schlenker, O. Massenet, R. Montmory, A. Yelon, A new property of ferromagnetic-antiferromagnetic coupling, physica status solidi (b) 16 (1966) 301–311.

[71] U. Nowak, K.-D. Usadel, J. Keller, P. Miltényi, B. Beschoten, G. Güntherodt, Domain state model for exchange bias. i. theory, Physical review B 66 (2002) 014430.

[72] A. Ghosh, Magnetic magnetocaloric and magneto-transport properties of Heusler Alloys, Ph.D. thesis, 2017.

Chapter 2

Experimental Details

2.1 Single crystal Growth

To explore novel phenomena in topological systems, a crucial prerequisite is the synthesis of materials in high-quality single-crystalline form. Polycrystalline powder introduces grain boundary effects, often blurring the delicate features. Additionally, in topological insulators , surface and bulk electronic states exhibit distinct properties. Polycrystalline samples, with a multitude of randomly oriented grains, make it impossible to differentiate between surface and bulk effects. Single crystals represent the purest state of any compound, featuring very long-range atomic ordering. They not only overcome these limitations but also provide well-defined crystallographic axes, offering the opportunity to investigate direction-dependendent properties. We have grown the single crystals of the materials using three techniques - chemical vapor transport, flux growth, and melt growth. We have used elements and compounds of high purity (99.9 % or higher) from reputable commercial sources.

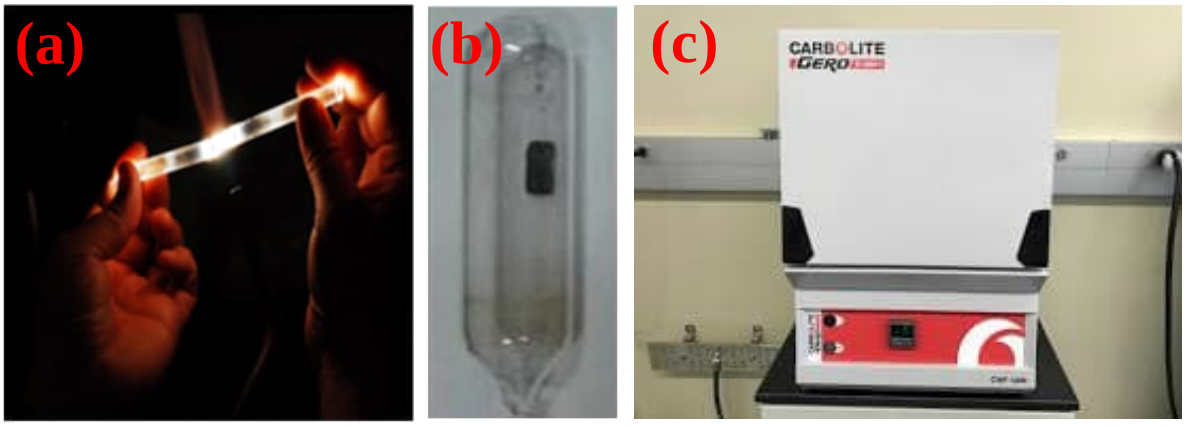

Figure 2.1: (a) Sealing a quartz tube under vacuum using a combination of oxygen and liquefied petroleum gas (LPG).(b) Sealed quartz tube containing material.(c) A muffle furnace with a maximum temperature capability of 1250°C.

(a) Chemical Vapour Transport

The chemical vapor transport (CVT) method is employed to grow single crystals in solids that lack adequate pressure for volatilization. These materials can undergo volatilization in the presence of a gaseous reactant, also known as a transport agent. Generally, a temperature gradient is utilized to facilitate the growth of the crystal. A transport agent with an endothermic nature conveys the polycrystalline material from the high-temperature end (source) and deposits it at the low-temperature end (sink) in the form of single crystals. Conversely, when utilizing an exothermic transport agent, the direction of crystal growth is reversed. To achieve successful crystal growth, various parameters must be optimized, including the temperature gradient, rate of mass transport, choice of transport agent, and the mass of the transport agent, among others. Halogens and halogen- based compounds are among the most commonly employed transport agents.

Primarily, crystallized iodine is utilized as a transport agent, vaporizing at temperatures above 457.5 K. Additionally, in certain instances, chlorides and bromides of metals such as VCl_3, $CoCl_2$, $TaCl_5$, $CoBr_2$, and $TeCl_4$ serve as transport agents, breaking down and generating chlorine or bromine gases. To prevent potential impurity phases and uphold vapor pressure, the polycrystalline powder and transport agent are enclosed in a vacuum-sealed quartz tube (10^{-5} Torr). The temperature gradient is induced by employing a two-zone tube furnace. The process has been displayed schematically in Fig. 2.2.

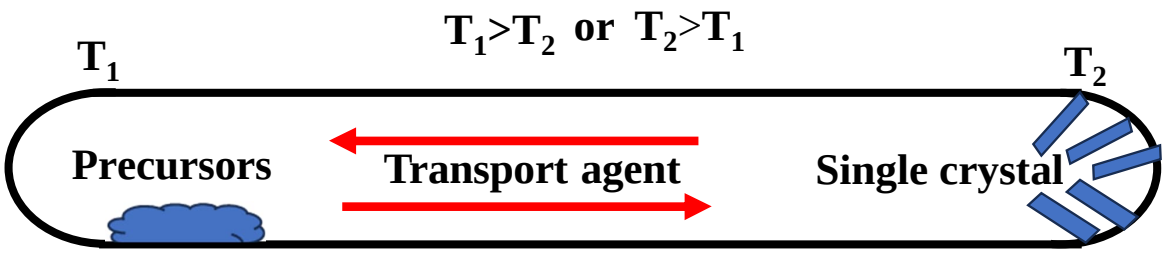

Figure 2.2: Schematic diagram depicting the experimental setup for chemical vapor transport experiments.

(b) Flux Growth

The underlying principles of the flux growth method closely resemble those of the solution growth technique, involving the growth of single crystals by initiating nucleation in a supersaturated solution. However, in flux growth, high purity elements or compounds with low melting points are employed as solvents or fluxes [1]. The flux and reactants are placed within a cylindrical alumina crucible and vacuum-sealed inside a quartz tube (10^{-5} Torr) to eliminate the risk of oxidation. The liquid solvent, above its melting point, initiates the chemical reaction, even if the reactants possess higher melting points.

Gradual cooling of the solution (approximately 3-5°C per hour) leads to the formation of nucleation points, initiating the crystallization process. In this approach, solid crystals are enveloped by a liquid flux that solidifies at room temperature, presenting challenges in the separation process. To mitigate this challenge, any excess flux is decanted at a temperature exceeding its melting point through centrifugation. Alternatively, certain flux materials can be chemically eliminated, as long as the chosen chemical does not react with the single crystals. The schematic of experimental set-up has been shown in Fig. 2.3.

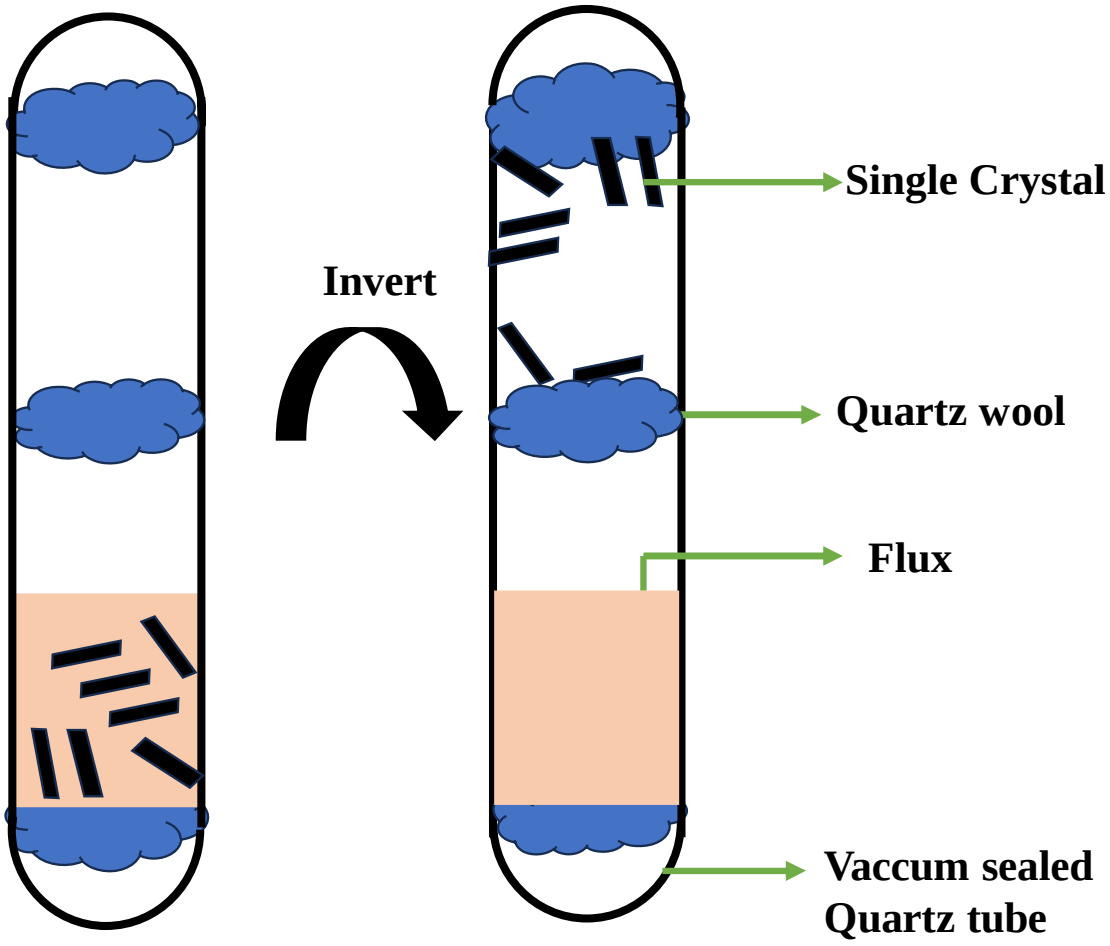

Figure 2.3: Schematic illustrating the single crystal growth in flux method.

(c) Melt Growth

If there is no incongruent melting, phase transformation occurring below the melting point, crystals can be formed by allowing the melt to cool naturally. Yet, merely solidifying the melt in a crucible usually yields to a polycrystalline mass, due to random nucleation and uncontrolled growth. For melt growth technique, constituent elements of the material were taken in stoichiometric ratio in argon atmosphere inside a glove box.

The mixture was put in an alumina crucible and placed in an evacuated quartz ampoule. After being maintained at higher temperature for several hours in a muffle furnace, the ampoule was slowly cooled to certain temperature at some temperature rate. Sometimes, ice water is used to quench the ampoule.

2.2 Sample characterization

Scanning electron microscope (SEM) machine attached with energy dispersive X-ray analysis (EDX) and powder x-ray diffraction (XRD) were used to analyze the as-grown single crystals. We confirmed the phase purity of the sample, extracted structural parameters from XRD and assessed the elemental composition through energy-dispersive X-ray spectra.

2.2.1 Structural characterization

There are three standard experimental methods of x-ray diffraction. These are

1. **Laue method**: In this technique, a single crystal is affixed to a goniometer, allowing controlled rotation along specified angles in two perpendicular planes. The crystal remains stationary within a beam of X-rays with continuous wavelength, similar to white radiation. The crystal selectively diffracts wavelengths that correspond to existing planes with spacing d and a glancing angle θ, in accordance with the Bragg's equation. The Laue method is hardly used for finding the unknown structure. It is mainly used for determining the orientation of known crystals only.

2. **Rotating crystal method**: The most ancient and accurate approach in X-ray crystallography is the single-crystal X-ray diffraction method. In this process, a single crystal is rotated about a fixed axis in monochromatic beam of X-radiation. The specimen is usually aligned with one of the crystallographic axes parallel to the axis of rotation. As a result of the rotation, various lattice planes are positioned for reflection. The diffracted images are recorded in photographic film.

3. **Debye-Scherrer powder method**: The most widely used method for determining the crystal structure and it is not required any single crystal.

In this PhD thesis, we worked on powder x-ray diffraction and single crystal x-ray diffraction for determining the crystal structure.

Powder x-ray diffraction method

X-ray diffraction (XRD) serves as a versatile tool extensively utilized for determining the structural properties of various materials. Its applications span from crystalline solids to inorganic and organic molecules, as well as biological systems. Powder XRD specifically

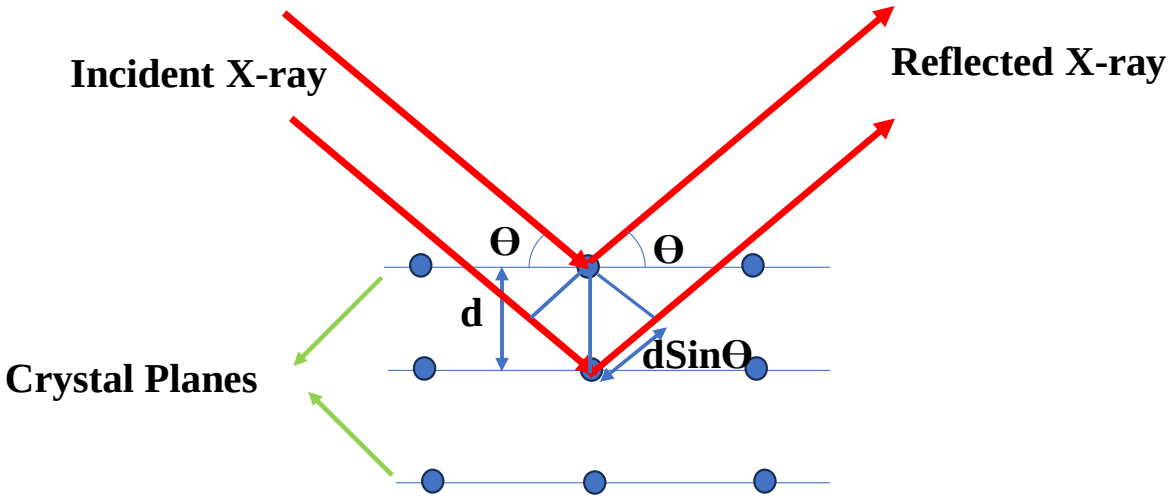

Figure 2.4: Schematic diagram illustrating the x-ray diffraction by crystallographic planes.

applies to polycrystalline samples, where the crystallographic planes of different grains are randomly oriented [2]. In this method, the sample is exposed to parallel beams of monochromatic X-rays. Since X-rays are electromagnetic waves, they primarily scatter through interaction with atomic electrons. In XRD measurements, we utilize elastic scattering events, which encapsulate information about the electronic distribution within the material.

In a crystal lattice with a periodic atomic arrangement Fig. 2.4 , each atom scatters X-rays in all possible directions. The resulting scattered beams interact with each other, exhibiting either constructive or destructive interference. Constructive interference leads to a significant increase in intensity and is observed at specific angles as dictated by Bragg's law [3]

$$2dsin\theta = n\lambda \tag{2.1}$$

Here, inter-planar spacing of the crystal is d, angle of diffraction is θ, n denotes the order of diffraction, and wavelength of the incident X-ray beam is λ. Currently, the majority of x-ray diffractometers work in the Bragg-Brentano geometry, as illustrated in Fig. 2.5. Here, the x-ray source and detector revolve around the sample in a circular motion, ensuring that when the sample is positioned at an angle θ, the detector consistently maintains a 2θ orientation relative to the incident beam. By systematically scanning through continuous 2θ values, it is possible to capture all potential Bragg peaks originating from randomly oriented grains. For this thesis work, we have used Rigaku SmartLab 9 kW X-ray Diffractometer using Cu-K_α radiation ($\lambda = 1.54$ Å) to characterize the samples. The data were acquired by varying 2θ in the range 10 °to 90°at intervals of

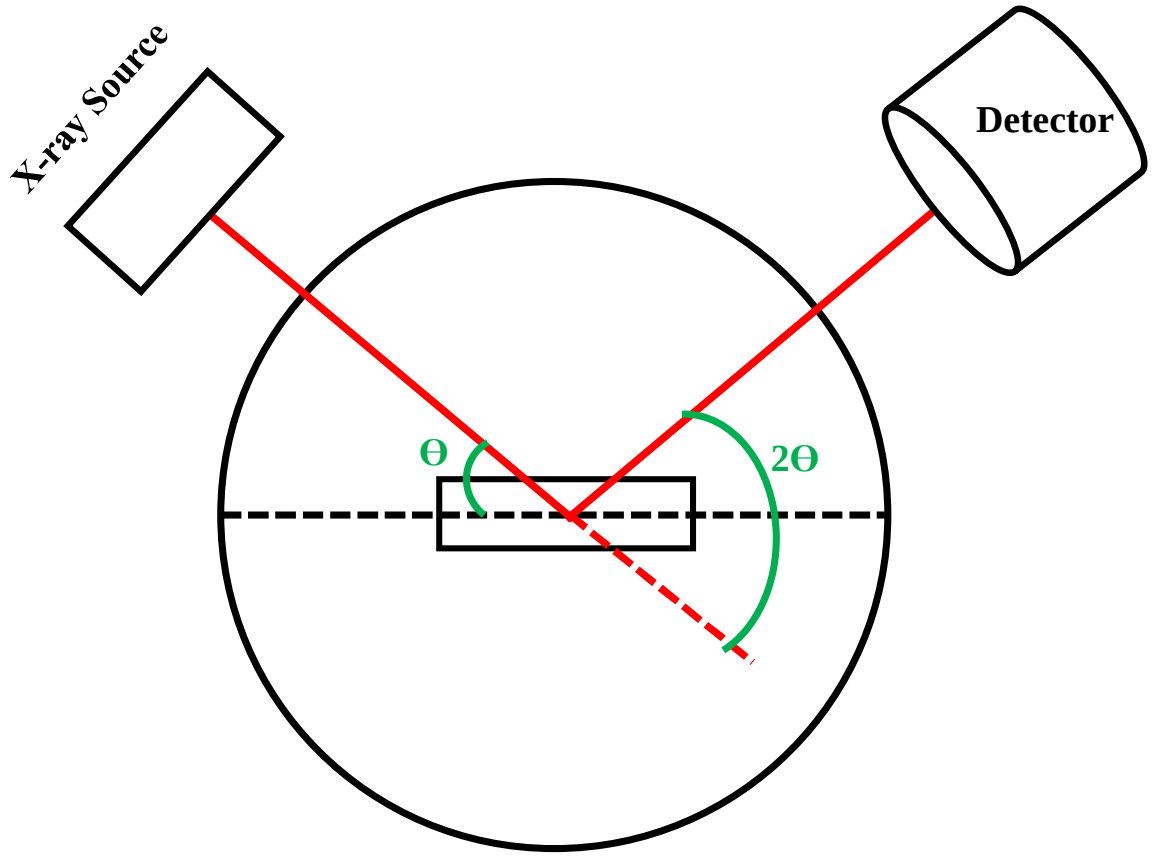

Figure 2.5: Schematic diagram illustrating the x-ray diffraction by crystallographic planes.

0.02°. The preparation of the samples involved crushing and grinding single crystals. To determine the space group symmetry and lattice parameters, the experimental data have been fitted using Rietveld structural refinement [4] with FULLPROF software package [5].

Single Crystal X-Ray Diffraction

Single-crystal X-ray diffraction (SCXRD) stands as the earliest and most precise technique within X-ray crystallography. The fundamental principle behind SCXRD involves the rotating crystal methods. For this method, single crystal is mounted on a rotation axis oriented perpendicular to a monochromatic x-ray beam, displayed in Fig. 2.6. The crystal undergoes rotation and cylindrical film is place around it. Sets of lattice planes will at some point form the correct Bragg angle, causing the formation of a diffracted beam at that point. Through the recording of diffraction patterns, encompassing both angles and intensities, one can ascertain the structure of the unit cell, along with the arrangement of atoms within the cell. In my thesis, We have measured the SCXRD data of the single crystal sample $HoSiAl_2$. We have computed the lattice parameters and crystal structure of this material which closely matches with the powder xrd data.

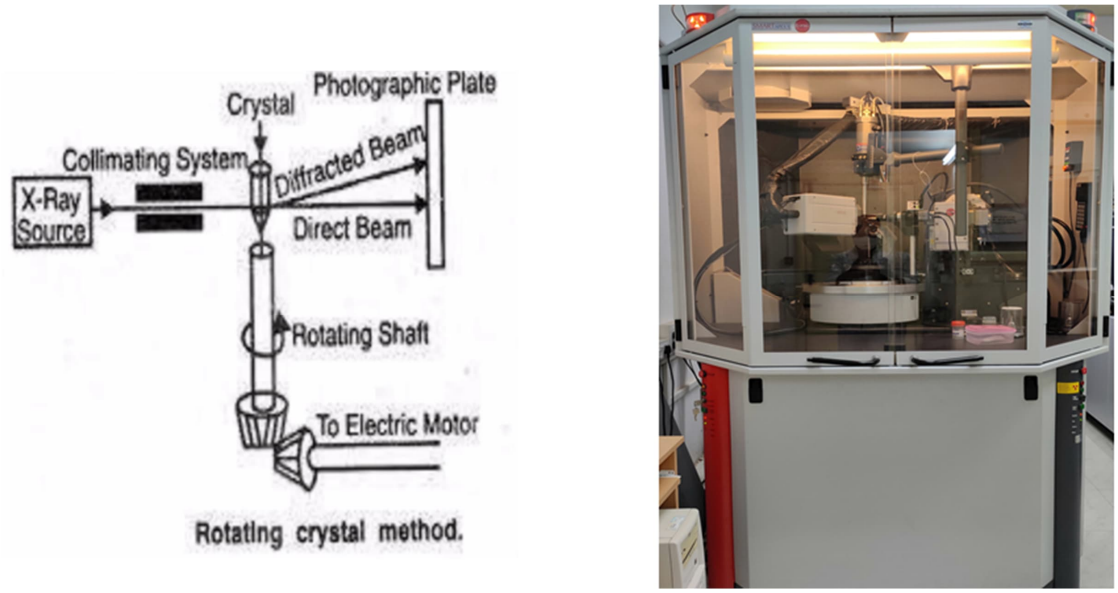

Figure 2.6: Rotating crystal method **(Source: Internet)** and Single crystal XRD instrument, IACS, Kolkata, India.

2.2.2 Scanning Electron Microscope

To investigate the material's morphology and composition high resolution scanning electron microscopy (SEM) is required in material science. Typically, SEM utilizes a high-energy electron beam, typically around 20 to 30 keV, to scrutinize materials. The scanning beam, with a diameter ranging from 5nm to 3 μm, explores the surface, revealing intricate details.

SEM comprises three primary components: an electron gun, electromagnetic lenses, and scan coils, displayed in Fig. 2.7 . The electron gun generates a stream of electrons, which travel through electromagnetic lenses like condenser lenses and objective lenses. The condenser lens controls the size of the electron beam spot, while the objective lens directs the electrons onto the material, focusing them sharply. In between these lenses, the scan coils deflect the electron beam across the surface of the material. When electrons interact with materials, inelastic collisions occur between the electron beam and the atoms within the material. Consequently, various signals emerge, including secondary electrons, back scattered electrons, auger electrons, and characteristic X-rays. Depending on their energy levels, secondary electrons and back scattered electrons are distinguished. Secondary electrons play a crucial role in creating surface images of the material. SEM image of the $FeCr_2Te_4$ single crystal is shown in Fig. 2.8.

2.2.3 Energy Dispersive X-Ray Spectroscopy

This method is non-destructive analytical techniques extensively used for investigating the chemical composition and assessing the degree of chemical homogeneity in metallic

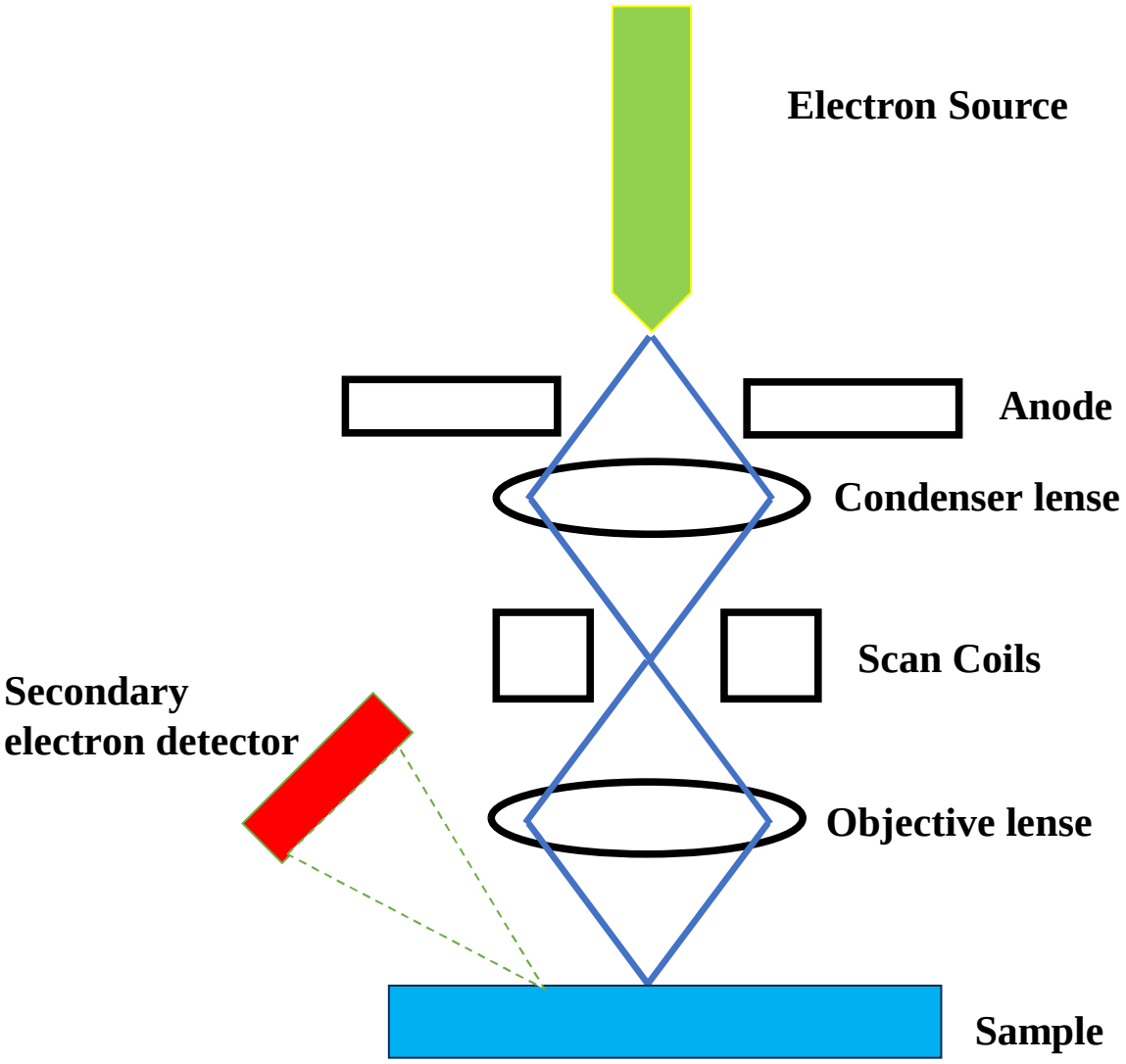

Figure 2.7: Schematic representation of scanning electron microscope (SEM).

samples. The fundamental principle of the EDAX is elaborated in the following paragraph.

When a high-energy electron beam interacts with the atoms of a material, it displaces electrons from the inner shell of the material, leaving behind vacancies. Electrons from higher energy levels then fill these vacancies, emitting energy in the form of characteristic X-rays. These X-rays provide direct insights into the composition of the material. According to Moseley's law, the energy of characteristic X-rays is inversely proportional to the atomic number of the material. In energy dispersive X-ray analysis (EDAX), a Si or Li detector is commonly used as an energy dispersive spectrometer to measure the energy and count the emitted X-rays.

The analysis was conducted at multiple positions on the sample surface to verify compositional homogeneity, shown in Fig. 2.9 (a). Fig. 2.9 (b) illustrates a typical X-ray spectrum, showing the EDAX spectra for the $FeCr_2Te_4$ single crystal.

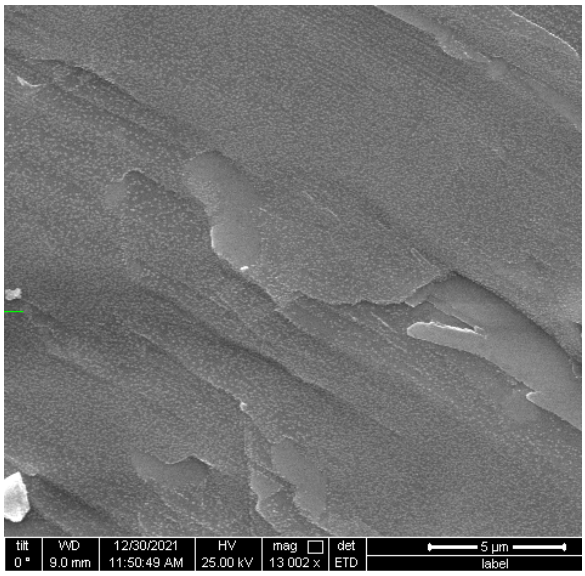

Figure 2.8: SEM micrograph of $FeCr_2Te_4$ single crystal.

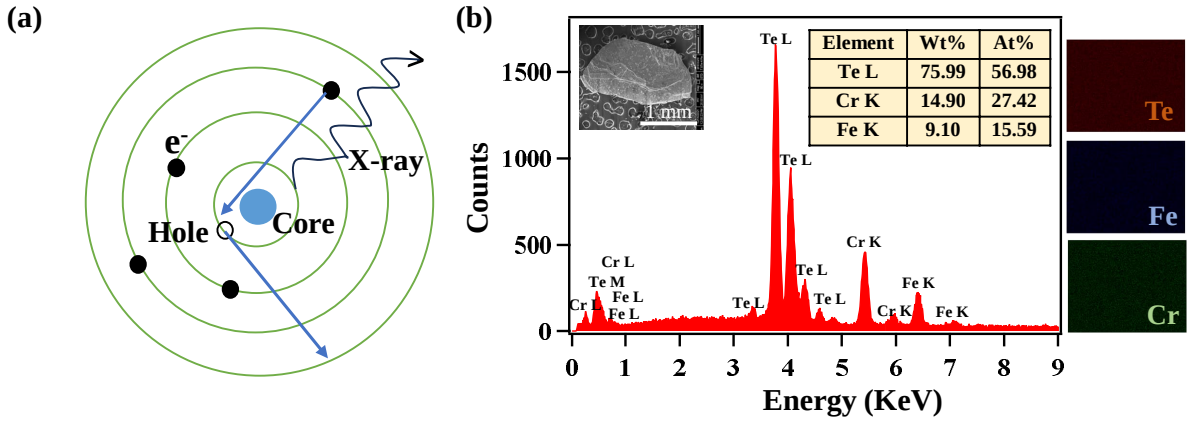

Figure 2.9: (a) Illustration depicting the schematic diagram for EDAX analysis. (b) Spectra from EDAX displaying the $FeCr_2Te_4$ single crystal.

We employed the FEI QuantaTM FEG 250 instrument for EDX analysis, displayed in Fig. 2.10.

2.3 Electronic transport and magnetic properties measurements

2.3.1 Electrical transport measurement

The materials investigated in this thesis are metallic systems having low resistances ($\approx$ mΩ). To measure the resistivity of these materials, a four-probe low-resistance circuit method was employed. A schematic representation is displayed in Fig. 2.11. The outer

Figure 2.10: The image of FEI QuantaTM FEG 250 instrument, accessible through the central equipment facilities of SNBNCBS, Kolkata, India. The inset depicts samples attached to the sample holder using conductive carbon tape.

leads were employed for passing the probe current, while the inner leads were utilized to detect the voltage drop. This method avoided lead and contact resistances since negligible current flowed through the voltage leads. We employed AC excitations for measuring the AC resistances. As the current flowing through both the sample resistance and standard resistance is same, it is expressed as $\frac{V_{sample}}{R_{sample}}=\frac{V_{std}}{R_{std}}$, where V_{std} and V_{sample} denote the voltage drops across the standard resistance and the sample, and R_{std} and R_{sample} represent the resistances of the standard resistance and the sample resistance, respectively. Therefore, computing V_{sample}, V_{std}, and R_{std}, we can determine the sample resistance using the formula $R_{sample} = V_{sample}$ x $\frac{R_{std}}{V_{std}}$

An alternating current (approximately 1-2 mA) was supplied by a lock-in amplifier having frequency of 111.11 Hz , passing through a standard resistance (around 1 kΩ). We have used the Stanford Research Systems 830 (SR830) digital signal processing (DSP) lock-in amplifier as the source for the alternating current. We have also measured the voltage across the sample utilizing this lock-in amplifier. Moreover, we have recorded the voltage drop across the standard resistance in a four-probe setup employing a Keithley 2000 digital multimeter (DMM). We employed a closed-cycle cryostat (CCR) supplied by Oxford InstrumentsTM (Optistat AC-V®) with a pulsed tube refrigerator (PTR) to

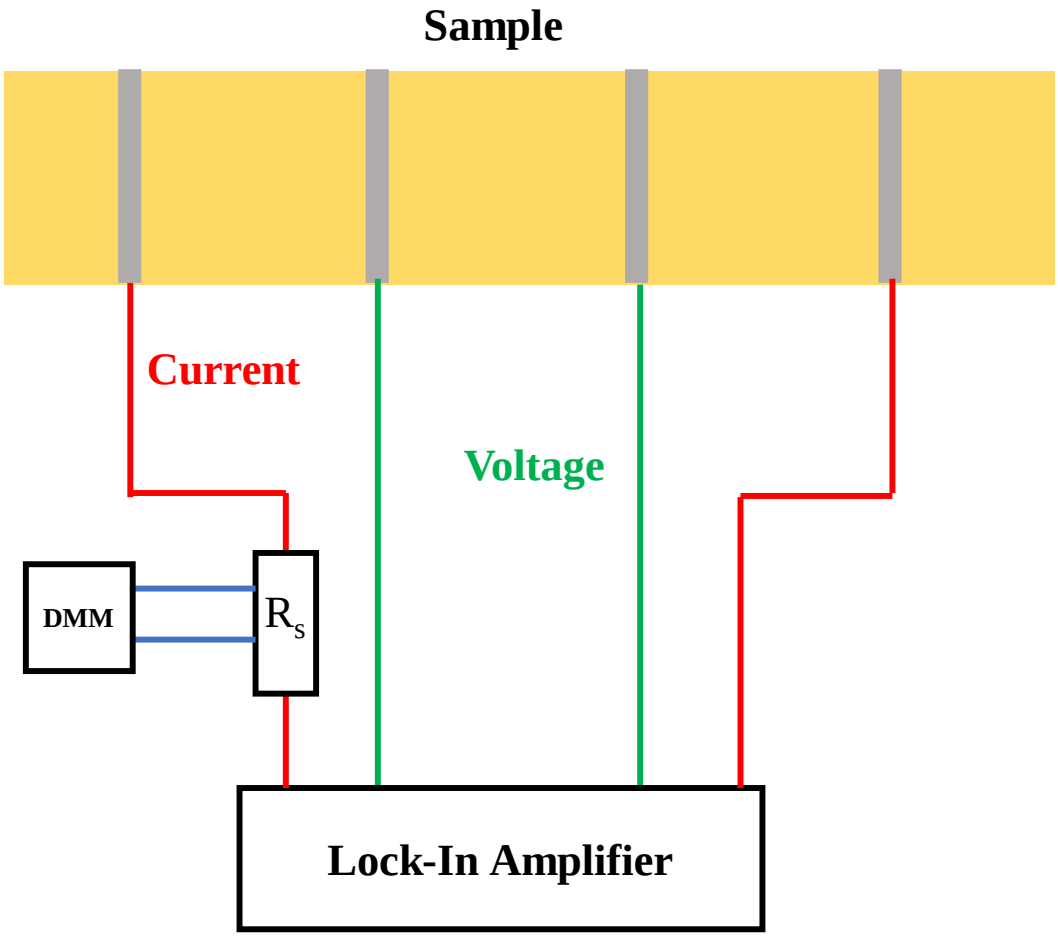

Figure 2.11: Schematic diagram illustrating the four-probe method utilized for resistivity measurement. R_S represents the standard resistance, and DMM stands for digital multimeter.

establish the low-temperature conditions which is required for measuring resistivity data at low temperatures. In this setup, resistance measurements were done within the temperature range of 3.8 K to 325 K.

Additionally, electrical transport measurements were carried out using a physical property measurement system (PPMS) (Quantum DesignTM PPMS-9T) with a standard puck and rotator setup, as illustrated in the [6]. The alternating current (ac) resistance was determined using the ac transport feature in the PPMS, displayed in Fig. 2.13. A sinusoidal current with a suitable amplitude and a frequency was applied across the outer two terminals, and the ac voltage was measured between the two voltage probes. The PPMS Multiview software program was used to record the resistance as a function of temperature and magnetic field. At various polar angles, magnetic fields were applied with the axis perpendicular to the ab-plane for magneto-transport measurements up to 9 T. Assuming a uniform current flow throughout the sample, the resistivity (ρ) was

Figure 2.12: Diagram illustrating the four-probe method employed for resistivity measurement. Standard resistance is denoted as R_S and the digital multimeter is referred to as DMM.

determined using the formula:

$$\rho = \frac{RA}{l} \tag{2.2}$$

where A represents the cross-sectional area perpendicular to the current path, and l suggests the distance between the two voltage terminals.

2.3.2 DC magnetization

VSM

The measurement of the dc magnetization of the samples varying with temperature and magnetic field was conducted using a Vibrating Sample Magnetometer (VSM) [7]. This measurement depends on Faraday's law of induction, which states that an alternating magnetic flux generates a voltage. In the presence of a magnetic field (H), the sample is magnetized by an applied magnetic field . When a magnetized sample oscillates within the pick-up coil, it generates a voltage in the coil. Then, the induced volatge is expressed as $V_{coil} = d\phi/dt = \frac{d\phi}{dz}\frac{dz}{dt}$ where ϕ represents the magnetic flux, and the vertical displacement of the sample relative to the coil is represented by z. In the case of sinusoidal oscillation of the sample, V_{coil} varies directly with the magnetic moment of the sample and is demonstrated by $V_{coil} = KmA\omega\sin(\omega t)$, where K is the coupling constant, dc magnetic moment of the sample is m, $\omega = 2\pi f$ where f represents the oscillation frequency of the sample and A denotes the oscillation amplitude. A diagram illustrating the configuration of a VSM system is presented in Fig. 2.14.

Figure 2.13: (a) Image of the Quantum DesignTM PPMS-9T instrument available under technical research centre at SNBNCBS. The picture of the ETO puck is in the inset. (b) Photograph depicting a representative specimen of a single crystal with electrical connections. Picture of the rotator puck one where the rotation axis (c) remains in the sample plane and (d) one where the rotation axis points out of the sample plane.

We utilized two distinct commercially available VSM systems to measure the magnetic properties of the samples: (i) the Lake Shore CryotronicsTM VSM and (ii) VSM equipped with Quantum DesignTM Physical Property Measurement System® (PPMS). The Lake Shore Cryotronics VSM system includes two cryostats, one designed for low-temperature measurements within the range of 80 K – 400 K and another for high-temperature measurements spanning from 300 K – 1273 K. This system can generate a maximum magnetic field of 1.6 T. Magnetization measurements were conducted over a temperature range of 2 K to 300 K, under magnetic fields reaching up to 9 T within PPMS VSM set up.

2.3.3 Squid

The Superconducting Quantum Interference Device (SQUID) is an exceptionally sensitive magnetometer that operates based on the Josephson effect and flux quantization. The Josephson effect [8] is a quantum phenomena where two superconductors are separated by a thin insulating layer, Cooper pairs of electrons tunnel through the junction, even

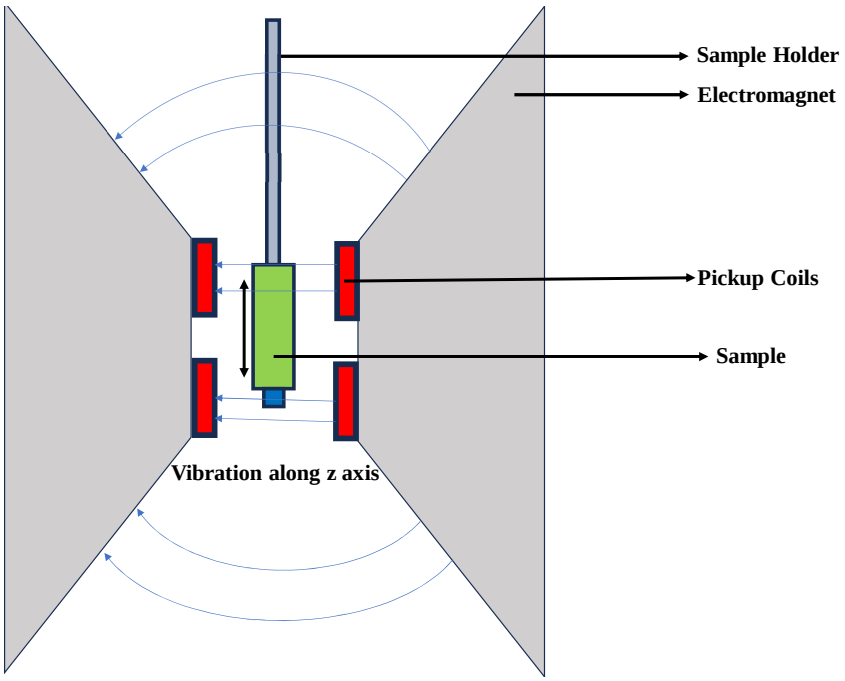

Figure 2.14: Schematic diagram illustrating the configuration of a Vibrating Sample Magnetometer (VSM).

without an applied voltage. There are two types of SQUIDs: the DC-SQUID, which operates based on the DC Josephson effect, and the RF-SQUID, which operates based on the AC Josephson effect. In the dc Josephson effect,A current flows through the Josephson junction even in the absence of an electric field. This occurs due to the phase change of the wave function across the junction. In the AC Josephson effect, a high-frequency AC voltage is applied across the junction, resulting in a current across the junction. In a DC-SQUID, a superconducting loop is formed by placing two Josephson junctions in parallel. When a magnetic field is applied perpendicular to the plane of the loop, the loop generates a current owing to the quantization of magnetic flux, where a magnetic flux quantum $\phi = \frac{h}{2e} = 2.0678 \times 10^{-15} \mathrm{Tm}^2$ (with h as the Planck constant and e as the electron charge). Measurements are done by moving the sample through superconducting detection coils. As the sample moves through the coils, its magnetic moment alters the magnetic flux enclosed by the pick-up coils. These superconducting pick-up coils are inductively coupled to a SQUID sensor, resulting any change in the signal from the pick-up coils to be reflected in the SQUID's output voltage. SQUID magnetometers have greater sensitivity than conventional VSM systems and can detect very small magnetizations in samples that are not detectable with conventional VSM systems. Fig. 2.15 illustrates a diagram of the SQUID.

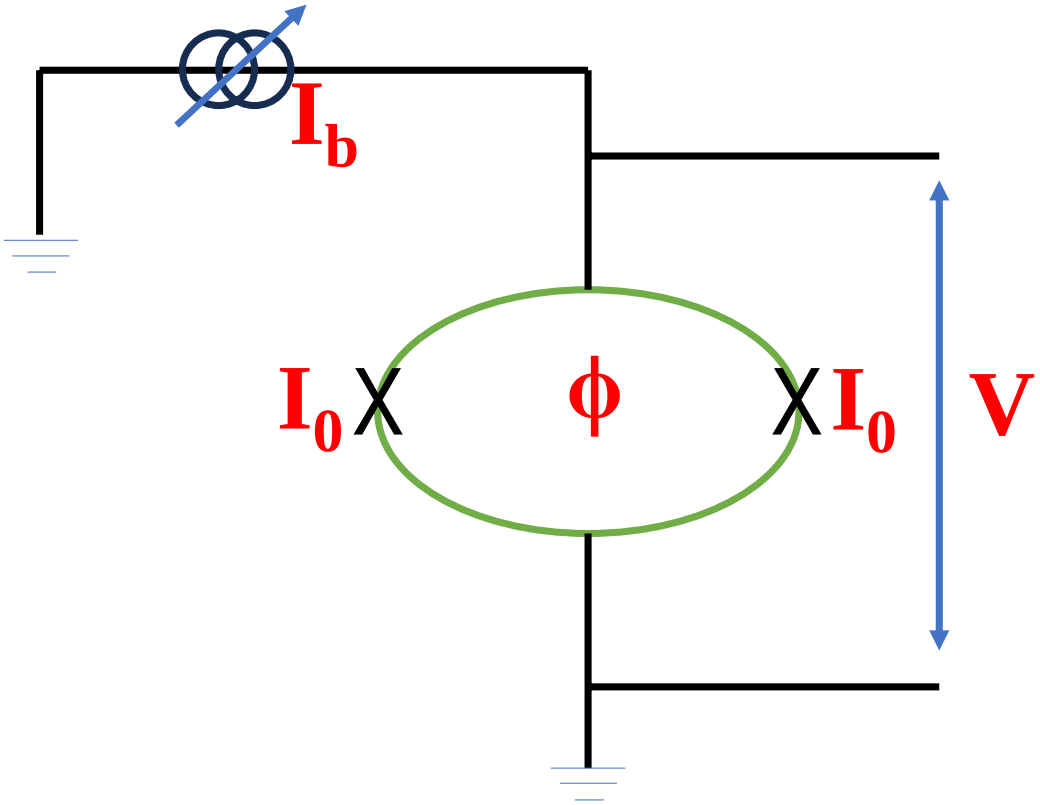

Figure 2.15: Schematic diagram illustrating a SQUID, the bias current and critical current are represented by I_b and I_0 , respectively. The flux passing through the SQUID is represented by ϕ, and V indicates the voltage response associated with that flux.

References

[1] P. C. Canfield, Z. Fisk, Growth of single crystals from metallic fluxes, Philosophical magazine B 65 (1992) 1117–1123.

[2] B. D. Cullity, Elements of X-ray Diffraction, Addison-Wesley Publishing, 1956.

[3] C. Kittel, Introduction to solid state physics, John Wiley & sons, inc, 2005.

[4] R. A. Young, The rietveld method, volume 5, International union of crystallography, 1993.

[5] J. Rodrigues-Carvajal, Fullprof: A rietveld refinement and pattern matching analysis program, Laboratoire Leon Brillouin, CEA-CNRS, France (2000).

[6] Physical Properties Measurement System User Manual, Quantum Design, USA, 2002.

[7] S. Foner, Versatile and sensitive vibrating-sample magnetometer, Review of Scientific Instruments 30 (1959) 548–557.

[8] B. D. Josephson, Possible new effects in superconductive tunnelling, Physics letters 1 (1962) 251–253.

Chapter 3

Observation of Exchange Bias in Antiferromagnetic $Cr_{0.79}Se$ due to Coexistence of Itinerant Weak Ferromagnetism at Low-temperature

3.1 Introduction

"The design and synthesis of materials with a strong magnetic exchange bias (EB) property has been one of the intense research activities from the past several decades [1] and till to the present days [2–5] due to their potential applications in spintronic devices [6, 7].

There exists several studies on designing the multilayered and core-shell structures to generate an effective large exchange bias at the interface of a ferromagnetic (FM) and an antiferromagnetic (AFM) layer [8–12]. Several bulk materials too have been synthesised, showing large exchange bias [13–15]. But most of the bulk materials are in the form of nanocomposites or with a complicated crystal structure of the doped ternary compounds. In this chapter, we will discuss the exchange bias in a transition-metal monochalcogenide having a simplest crystal structure.

Transition-metal monochalcogenides with the chemical formula of MX (M= Fe, Cr; X=S, Se, Te) are very versatile materials due to their diverse structural, electronic, and magnetic properties. For instance, Fe_xSe is a non-magnetic high temperature superconductor with a T_c of 8 K, having a tetragonal crystal structure for $x \geq 1$ [16], while it is an antiferromagnetic metal having hexagonal crystal structure for $x<1$ [17]. Whereas, FeTe is always a tetragonal antiferromagnetic system with a stripe order [18, 19]. Further, FeS is found to be a non-magnetic superconductor with a tetragonal crystal structure [20]. On the other hand, similar to Fe_xX, Cr_xX systems too are very diverse in their structural, electronic, and magnetic properties. For instance, Cr_xTe is a ferromagnetic half-metal

Results presented in this chapter are published in **ACS Omega** , 6(42), 28012-28018, (2021).

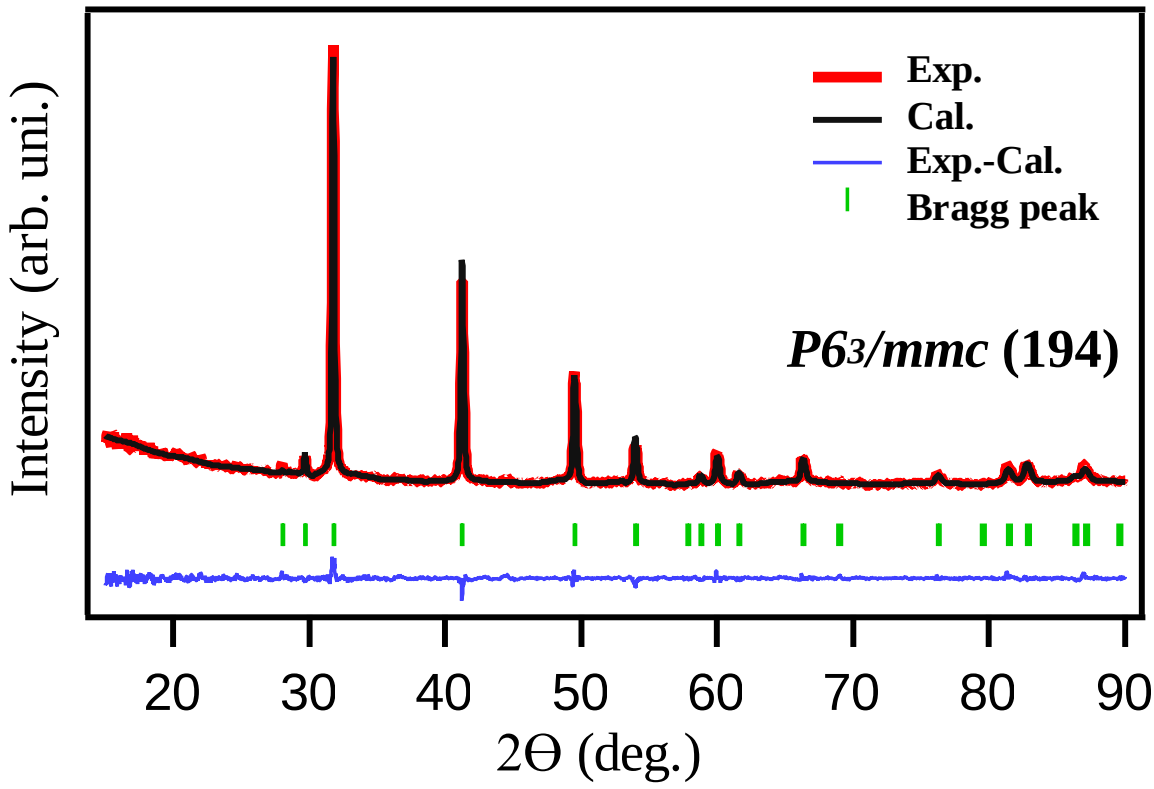

Figure 3.1: Powder X-ray diffraction pattern and reitveld refinement of $Cr_{0.79}Se$, confirming the NiAs-type crystal structure with space group of $P6_3/mmc$ (194).

and can exist in any of zinc-blend (ZB) [21], rock-salt (RS) [22], or NiAs [23] crystal structure type. Whereas, Cr_xS [24] and Cr_xSe [25] are mostly known for their antiferromagnetic nature having the NiAs-type crystal structure. Some reports suggested Cr_xSe to be even a spin-glass system [26] and Cr_xS to be a ferrimagnetic metal [27].

In this report, we report a comprehensive study on the structural, electrical transport, and magnetic properties of $Cr_{0.79}Se$ in the polycrystal form. Till date not many experimental studies are available on these system, despite being a non-collinear AFM metal [25]. Recently, it was suggested that the antiferromagnetic metals with non-collinear spin texture are promising candidates for the anomalous Hall effect, induced by the berry curvature [28–30]. With this motivation, we reinvestigated the structural, electrical, magnetic properties of this system. Our X-ray diffraction studies demonstrate that $Cr_{0.79}Se$ has a NiAs-type structure. At higher temperatures we noticed shift in certain XRD peak positions, leading to change in the lattice parameters with temperature. In addition, from the temperature dependent XRD measurements we observe that the NiAs-type structure is stable up to as high as 600^oC of the sample temperature. Electrical resistivity studies show Fermi-liquid like metallic behaviour at low temperatures (< 41 K), and in the intermediate temperatures (41-200 K) the resistivity changes sublinearly with temperature. Further, at the elevated temperatures (> 200 K) the rate of change of resistivity rapidly decreases with temperature. Magnetic properties studies suggest a

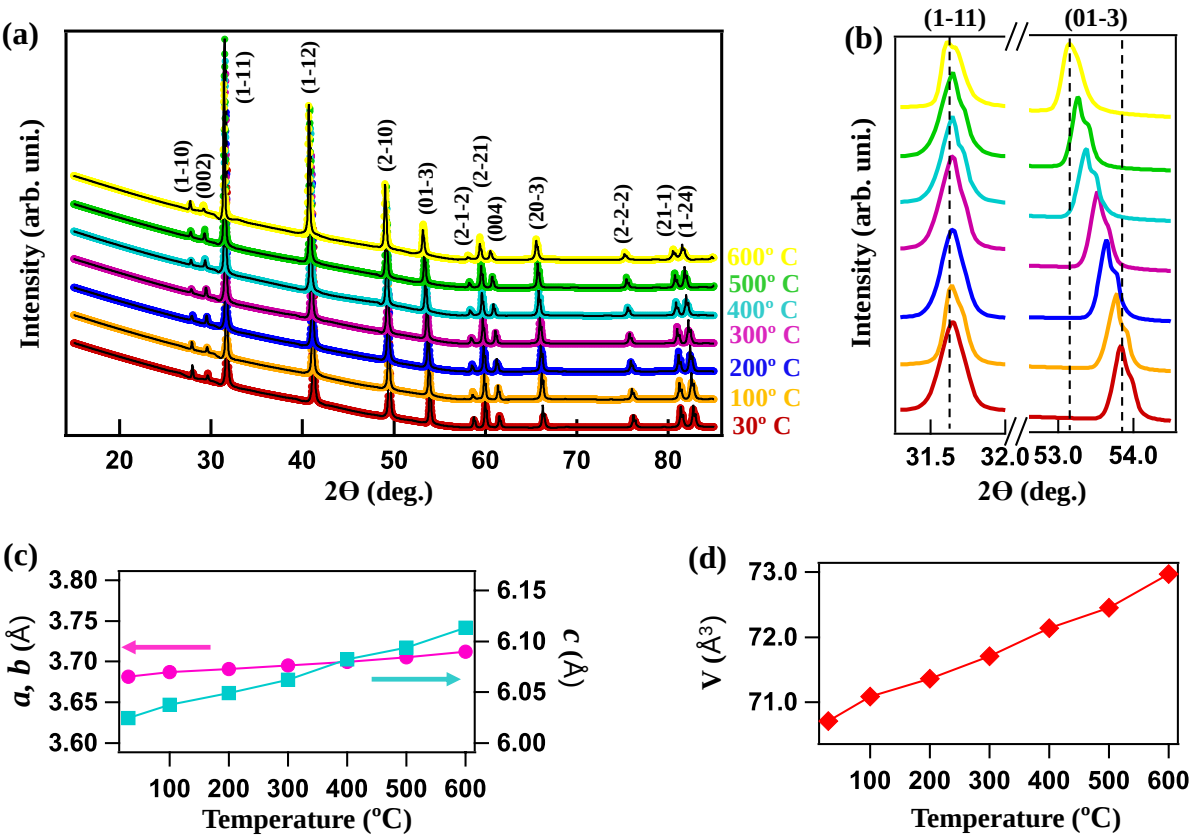

Figure 3.2: (a)Temperature dependent powder X-ray diffraction pattern of $Cr_{0.79}Se$ overlapped with reitveld refinement. (b) Enlarged XRD patterns for the reflections of $(1\bar{1}1)$ and $(01\bar{3})$. (c) Plot of lattice constants a, b, and c as a function of temperature. (d) Plot of cell volume (V) as a function of temperature.

transition from paramagnetic phase to an antiferromagnetic phase at a Néel temperature of 225 K. Further, below 100 K, a weak ferromagnetism is found which is coexisting with antiferromagnetism.

3.2 Methods

Samples of $Cr_{0.79}Se$ are prepared by the standard solid-state reaction method [31] from high purity powders of Chromium (4N, Alfa Aeser) and Selenium (5N, Alfa Aeser) elements by mixing in appropriate ratio. The well-mixed powders were then heated in a muffle furnace at 1000^{o}C for 48 hours. The final sample was pressed into pellet form and heated again at 1000^{o}C for another 48 hours. As prepared polycrystalline sample was structurally characterized using the powder X-ray diffraction (XRD) equipped with Cu Kα radiation of Rigaku-SmartLab (9 KW) at various samples temperatures (30^{o}C to 600^{o}C). Rietveld refinement analysis of the XRD data is done using FULLPROF software package [32]. Energy-dispersive X-ray (EDX) analysis suggests the chemical composition of as prepared sample to be $Cr_{0.79}Se$. Electrical resistivity measurements were carried out

using the standard four-probe technique with a closed-cycle refrigerator (CCR) based cryostat, within a temperature range of 3.1 K to 310 K. Conducting silver epoxy and Cu wires were used to make the electrical contacts. Magnetic property measurements were carried out using the vibrating sample magnetometer (VSM) (DynaCool, Quantum Design) up to a magnetic field of 9 tesla.

3.3 Results

Figure 3.1(a) shows rietveld refinement on the XRD data of $Cr_{0.79}Se$ measured at the room temperature (RT). It is evident from the XRD data that $Cr_{0.79}Se$ crystallizes into the NiAs-type crystal structure with a hexagonal space group of $P6_3/mmc(194)$. The estimated lattice parameters from the rietveld refinement are found to be a=b=3.6811(3)Å and c=6.0198(6) Å. No additional impurity peaks have been noticed from the XRD data, demonstrating high phase purity of the sample. Further, we have performed XRD measurements as a function of temperature starting from RT to 600^{o}C, as shown in Figure 3.2(a). From the temperature dependent XRD data we noticed that the peak positions are relatively shifted with the temperature. To demonstrate the peak shift, in Figure 3.2(b), we fixed peak position of the reflection $(1\bar{1}1)$ to notice a significant shift in peak position of the reflection $(01\bar{3})$. In order to elucidate the structural changes with the temperature, we performed rietveld refinement for the XRD data at every measured temperature. The obtained lattice parameters are plotted as a function of temperature as shown in Figure 3.2(c). We identify that the lattice parameter $a(b)$ is almost constant, changing from 3.681 Å to 3.712 Å, while the lattice parameter c substantially increases from 6.024 Å to 6.113 Å in going from RT to 600^{o}C. Consequently, the unit cell volume also increases with the temperature as shown in Figure 3.2(d).

Figure 3.3 shows temperature dependent electrical resistivity of $Cr_{0.79}Se$ measured within the temperature range of 3.1 to 310 K. We observe from the resistivity data that at low temperatures (T<41 K), the data nicely fits to the Fermi liquid law of resistivity ($\propto aT^2$). But beyond, 41 K the data follows a sublinear behaviour ($\propto bT^{0.62}$) with temperature up to 200 K. Inset, in Fig. 3.3 confirms the Fermi-liquid nature of the resistivity as one can notice perfect linear relation between ρ and T^2 (for T up to 41K). Bottom panel of Fig. 3.3 presents the plot of dρ/dT vs T. We notice that dρ/dT increases with T up to 41 K, above 41 K dρ/dT decreases with T up to 302 K, and beyond 302 K -dρ/dT decreases with T hinting at an electronic phase transition at this temperature as dρ/dT becomes $-ve$. Next, in Figure 3.4, we show magnetization (M) as a function of temperature measured under zero-field-cooled (ZFC) and field-cooled (FC) modes at an applied external magnetic field of 500 Oe. In Fig. 3.4, further we show inverse magnetic susceptibility ($1/\chi$) as a function of temperature measured in the FC mode. As can be seen from Fig. 3.4, at higher temperatures (T>225 K), susceptibility follows the Curie-Weiss law,

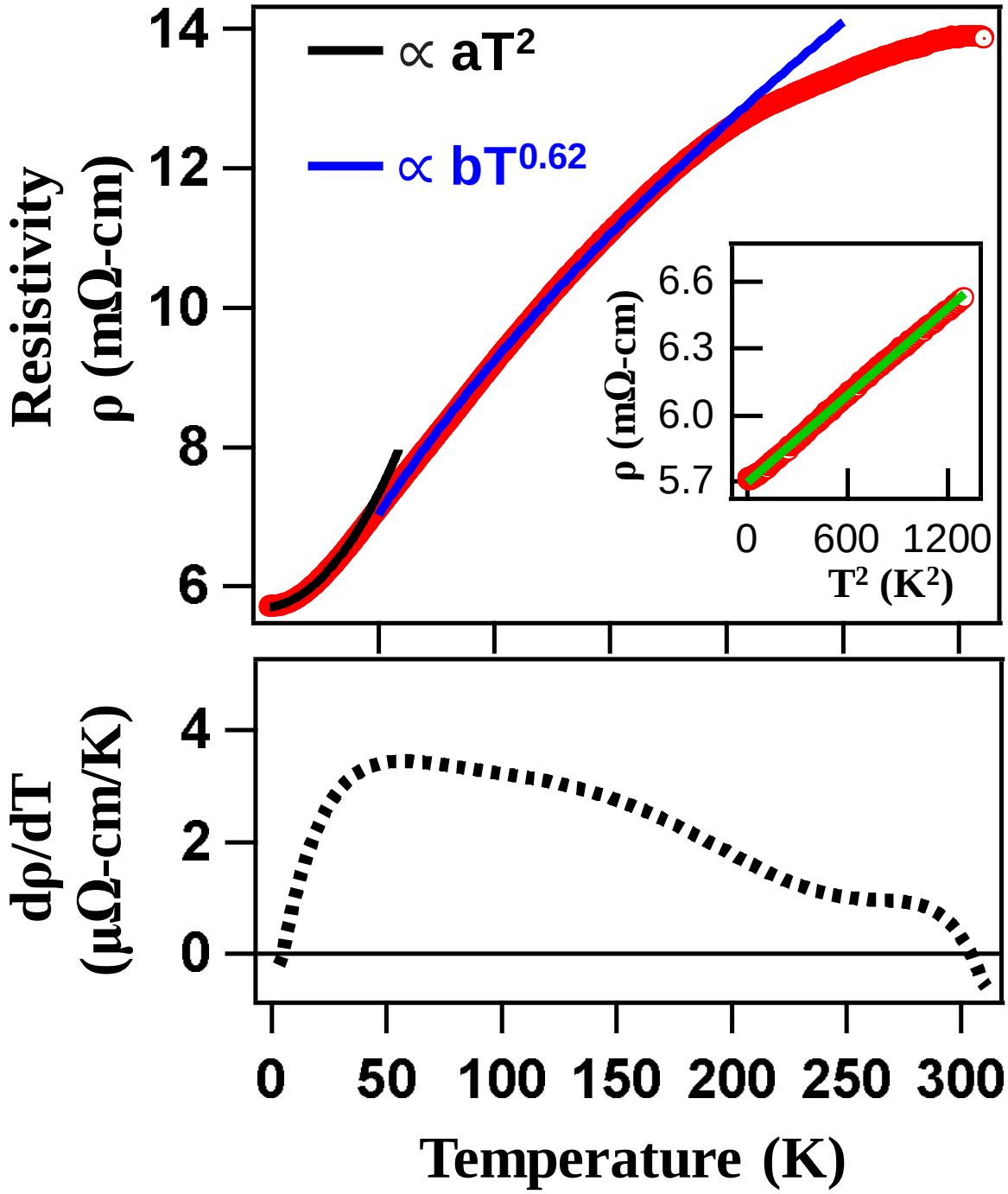

Figure 3.3: Temperature dependent electrical resistivity of $Cr_{0.79}Se$. Black solid curve represents T^2 law fitting up to 41K and the blue solid curve represents sublinear fitting between 41 and 200 K. Inset shows the plot of ρ *vs.* T^2. Green line in the inset is a linear fit to the data. Bottom image represents dρ/dT *vs.* T

$$\chi(T) = \frac{C}{T - T_C} \tag{3.1}$$

here, C is the Curie constant and T_C is the asymptotic Curie temperature. From

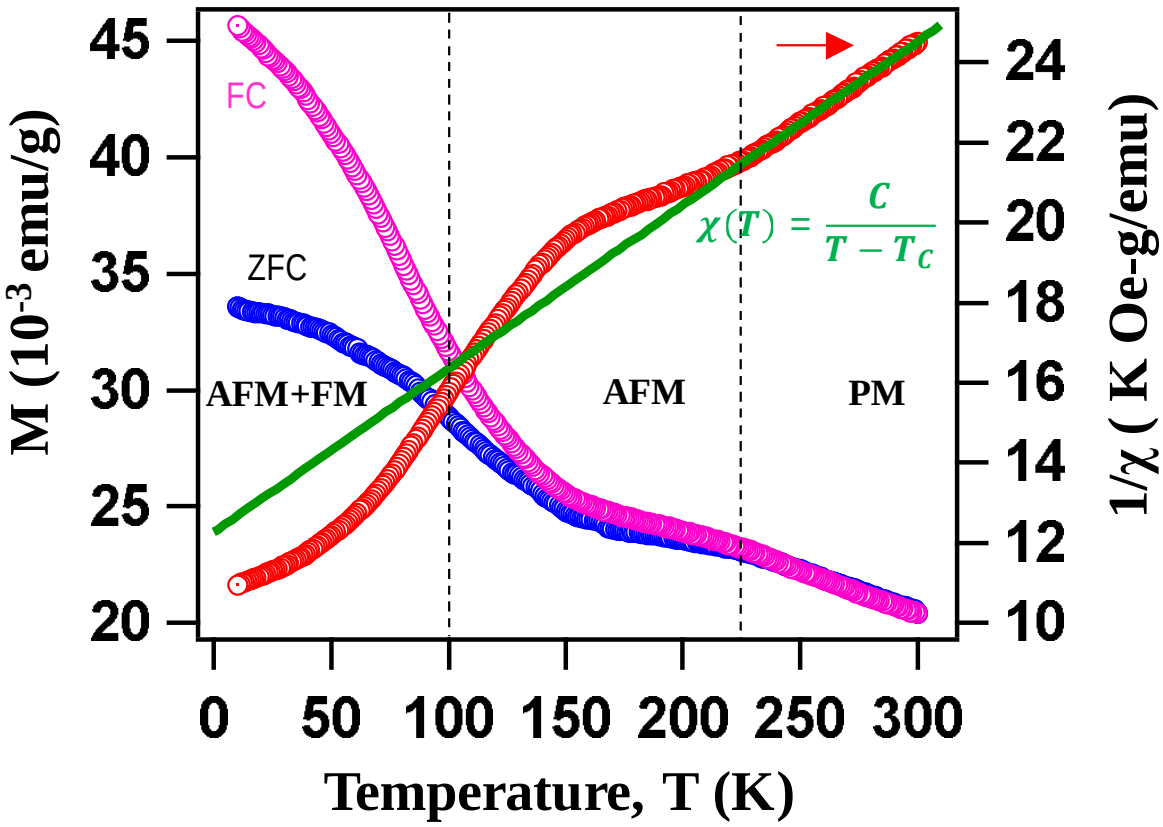

Figure 3.4: Magnetization as a function of temperature plotted for zero-field-cooled (ZFC) and field-cooled (FC) modes. Susceptibility as a function of temperature is plotted for the FC mode. Blue curve is a susceptibility fitting with the Curie-Weiss law.

the fitting, we found an asymptotic Curie temperature of T_C=-300±2 K and a Curie constant of C= 24.5±0.5 Oe.gm.emu^{-1}.K^{-1}. The negative asymptotic Curie constant suggest for a dominant antiferromagnetic interactions in the system. We further have calculated the effective magnetic moment of Cr ion in the paramagnetic regime using the formula, $\mu_{eff} = 2.84\sqrt{MC}\ \mu_B = 5.08\mu_B$/Cr [33]. In addition, we observe a deviation from the linear dependence of $1/\chi$ on T below 225 K, suggesting a magnetic transition from a paramagnetic to an antiferromagnetic phase.

Figure 3.5 depicts $M - H$ curves taken in the ZFC mode with an applied magnetic field of 1.5 T at temperatures 10, 100, and 150 K. From the inset shown at the bottom of Fig. 3.5, we observe hysteresis in the $M - H$ loop with a coercive field of H_C=410 Oe when measured at 10 K and the hysteresis disappears at 100 K. Presence of hysteresis loop suggests for a ferromagnetic order at low temperature. Also, magnetization saturation is not reached up to the applied field of 1.5 T suggesting for a strong AFM order as well in this system. In order to quantify the strength of ferromagnetism in the system, as shown in the top-left inset of Fig. 3.5, we performed M-H curve fitting with equation 2.2 [34], to estimate the saturation magnetization M_s=1.3±0.1 emu/g and remanent magnetization M_r=0.09±0.01 emu/g, while holding the experimental coercive field H_c=410 Oe and

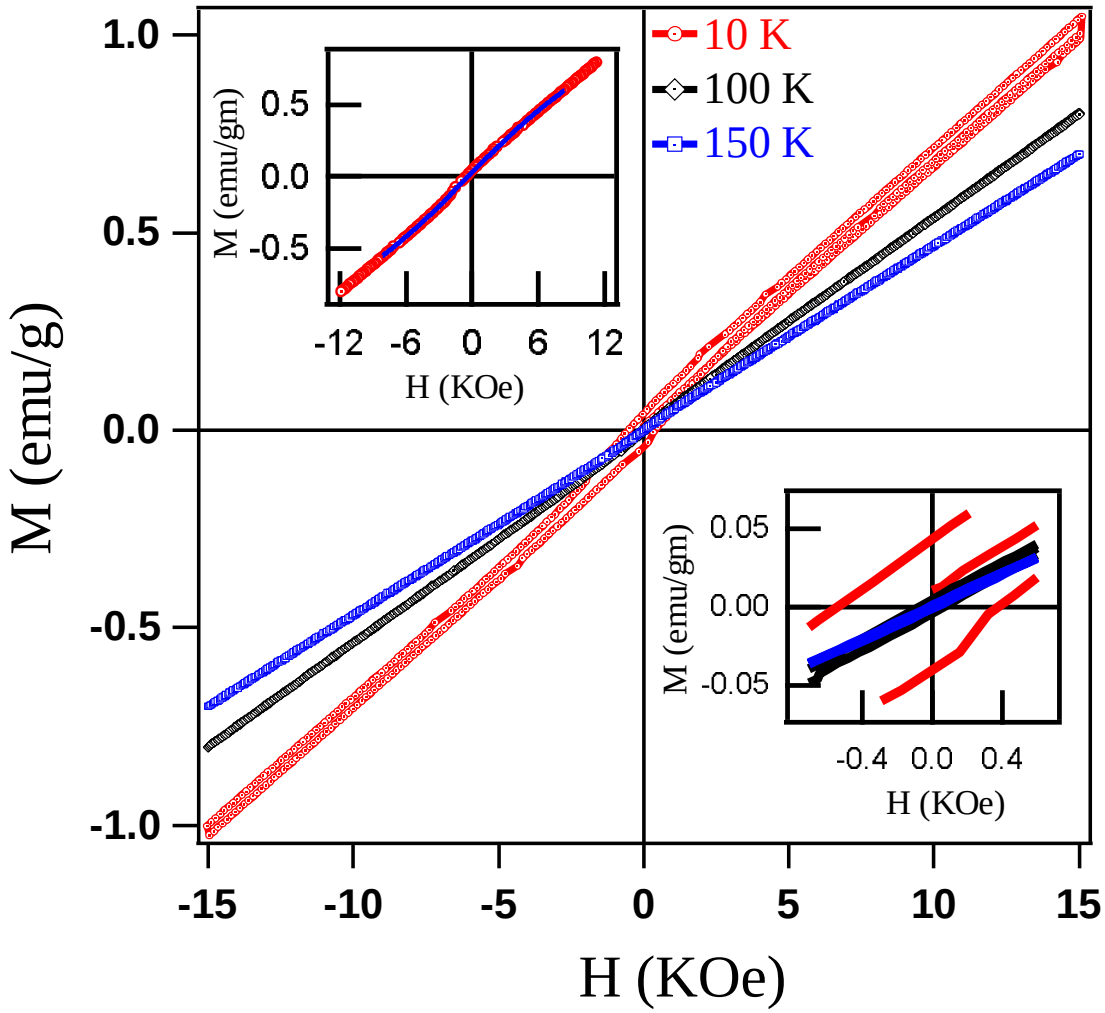

Figure 3.5: Magnetization (M) as a function of applied magnetic field (H) is plotted for the ZFC mode at sample temperatures of 10, 100 and 150 K. Top-left inset shows M-H curve fit using the Eq. 2.1. Bottom-right inset shows enlarged data around the zero magnetic field to show the hysteresis of M-H curve for 10 K, which disappears above 100 K.

susceptibility χ=9.1 $\times$ 10^{-5} emu/(Oe-g). These values suggest for a weak ferromagnetism in $Cr_{0.79}Se$.

$$M(H) = \frac{2M_s}{\pi} tan^{-1}[(\frac{H}{H_c} \pm 1)\ tan(\frac{M_r}{2M_s})] + \chi H \tag{3.2}$$

Figure 3.6(a) depicts $M-H$ curves measured in the FC mode at various sample temperatures using the applied magnetic field of 3 T. Inset at the right-bottom of Fig. 3.6(a) demonstrate a significant shift in the M-H loop hysteresis, hinting at the presence of exchange bias in this sample. Figure 3.6(b) depicts M-H curves in the FC mode at a fixed sample temperature of 10 K by varying the applied magnetic fields, 3 T, 6 T, and 9 T. Right-bottom inset of Fig. 3.6(b) is the zoomed in image of $M-H$ loops in which one can notice hysteresis at all applied magnetic fields. Further, left-bottom inset of

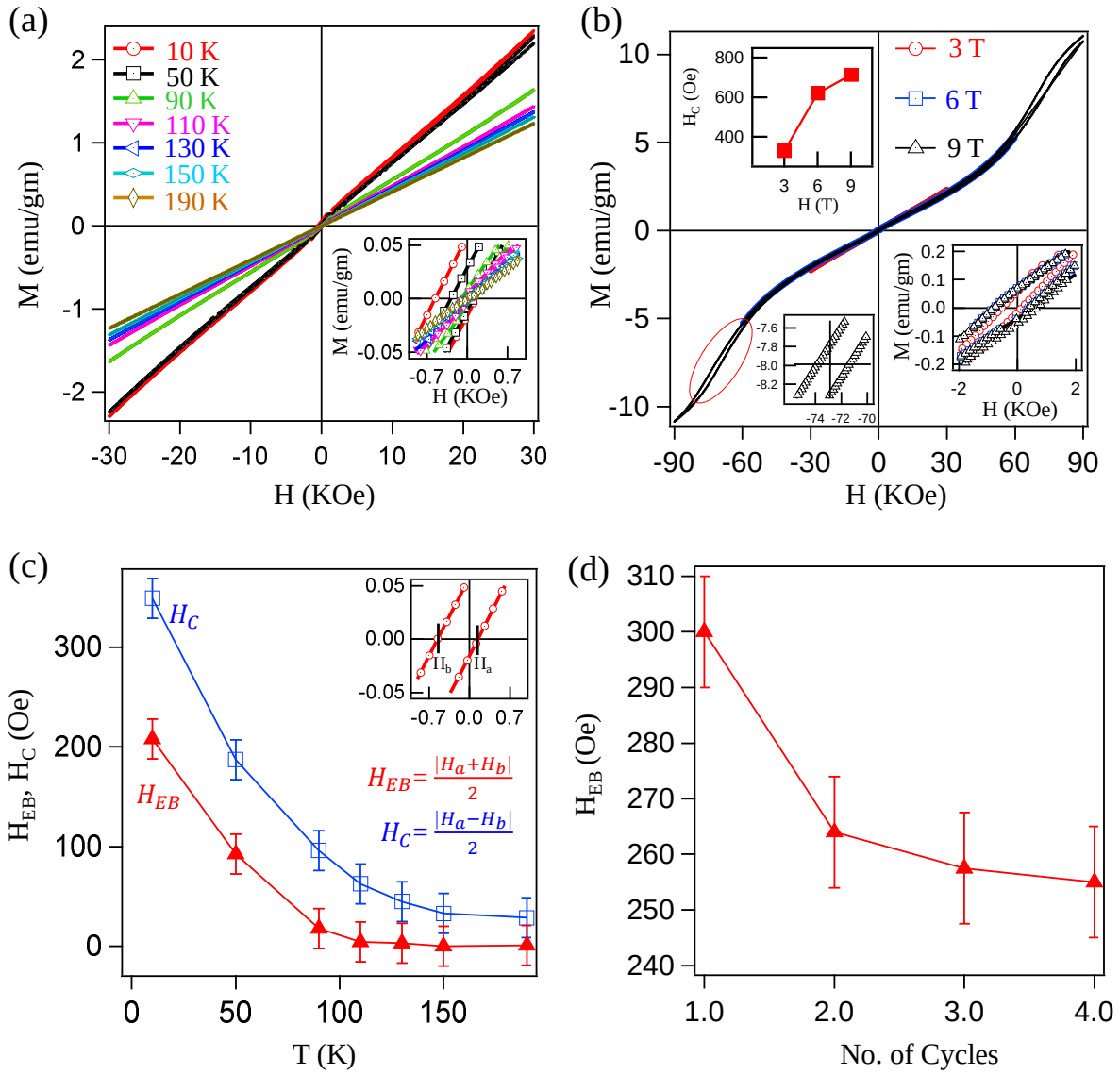

Figure 3.6: (a) M-H loops plotted for the FC mode at various sample temperatures. Inset in (a) is enlarged data around the zero magnetic field to show the hysteresis of M-H curve. (b) M-H curves plotted for the FC mode at various applied magnetic fields. Bottom-right inset in (b) is enlarged data around the zero magnetic field to show the hysteresis of M-H curve at various applied fields. Bottom-left inset in (b) is enlarged data to show the hysteresis of M-H curve for the applied field of 9 T. Top-right inset in (b) shows coercive field as a function of applied field. (c) Exchange bias (H_{EB}) and coercive field (H_C) are plotted as a function of temperatures. (d) Plot of H_{EB} *vs.* no. of M-H loop cycles.

Fig. 3.6(b) is the zoomed in image of $M-H$ loop measured with a magnetic field of 9 T, demonstrating the presence of hysteresis between 6 and 9 T. Figure 3.6(c) depicts the exchange bias (H_{EB}) and coercivity (H_C) plotted as a function of temperature. From Fig. 3.6(c) we can observe that both H_{EB} and H_C decrease with increase in temperature and become negligible above 100 K within an instrumental error of$\pm$20 Oe. Figure 3.6(d) depicts training effect on the exchange bias. We observe a significant decrease (15%) in the exchange bias after repeating four cycles of $M-H$ loops. The observation of exchange

bias under the FC mode but not under the ZFC mode is in line with the phenomenon of the exchange bias, as explained for various magnetic alloys and compounds [35].

3.4 Discussions

The studied sample, $Cr_{0.79}Se$, has been found in the NiAs-type structure of the hexagonal crystal symmetry as demonstrated in Figs. 3.1 and 3.2, which is consistent with the crystal structure of stoichiometric CrSe [31]. On the other hand, the crystal symmetry of the so far existing off-stoichiometric systems of Cr_xSe deviate form the stoichiometric system. For instance, $Cr_{0.67}Se$ posses trigonal crystal symmetry with a space group of $R\bar{3}H$ (148) [36], while $Cr_{0.875}Se$, $Cr_{0.75}Se$ and $Cr_{0.625}Se$ posses the monoclinic crystal symmetry with a space group of $C1_2/m1(12)$ [37–39]. Most importantly, we identify that $Cr_{0.79}Se$ is the first known off-stoichiometric composition crystallizing in the $P6_3/mmc$ space group. Further from the temperature dependent XRD data, we notice peak shifting with the temperature. Such a peak position shift with temperature generally lead to change in the lattice parameters while still preserving the crystal symmetry. This has been supported by the rietveld refinement (see Fig. 3.2). Thus, our studies confirm that the NiAs-crystal structure of $Cr_{0.79}Se$ is stable up to 600^oC from the room temperature. Though Jahn-Teller distortion is not observed so far in any of the off-stoichiometric Cr_xSe compositions, in the case of stoichiometric CrSe, the Jahn-Teller distortion is suggested for temperature below 305^oC [40]. However, we do not observe any signature of Jahn-Teller distortion from our temperature dependant XRD data in the studied compounnd.

Next, from the electrical resistivity data shown in Fig. 3.3(a) it is clear that $Cr_{0.79}Se$ is as a Fermi-liquid type metal below 41 K. But above 41 K, the system deviates to a non-Fermi-liquid type metal showing a sub-linear dependence of the resistivity on temperature. The same is confirmed from the $d\rho/dT$ *vs* T curve [see bottom of Fig. 3.3(a)]. From this curve we observe that $d\rho/dT$ increases with temperature up to 41 K and after that it decreases with T to reach zero at 302 K. Above 302 K, -$d\rho/dT$ decreases with increasing T up to the measured temperature of 310 K. This observation hints at a metal-insulator (MI) transition above 302 K in $Cr_{0.79}Se$. MI transition has been noticed in some of the other transition-metal monochalcogenides as well. For instance, in $Fe_{0.875}Se$ the MI transition is observed at 100 K due to a proximity effect of magnetic moment reorientation [17]. On the other hand, no report exist so far showing the MI transition in the off-stoichiometric compositions of Cr_xSe except that $Cr_{0.68}Se$ was reported to be a small gap semiconductor (E_g=3.9 meV) [29].

Finally coming to the important observations of this study, we found a weak ferromagnetism in $Cr_{0.79}Se$ below T_C=100 K that is coexisted with the AFM phase. As a result an exchange bias has been observed in this system below T_C. Usually, CrSe is known for their non-collinear AFM phase. But recently, one report showed a weak ferromagnetism in $Cr_{0.67}Se$ along with AFM phase below 50 K [41]. However not much

discussion is drawn on the presence of the exchange bias in $Cr_{0.67}Se$. Thus, we report the exchange bias for the first times in these systems of Cr_xSe. Another report of the neutron diffraction studies on $Cr_{0.67}Se$ suggests for the existence of two magnetic phases. They are low temperature (< 38 K) non-collinear AFM and high temperature (38 K>T<45 K) collinear AFM, but did not find the ferromagnetism down to as low as 6 K [36]. On the other hand, the estimated effective paramagnetic moment of $5.08\mu_B$/Cr in our systems is slightly higher than the effective paramagnetic moment of $4.5\mu_B$/Cr in the stoichiometric CrSe [23]. This could be mostly because of the mixed Cr valance states in the off-stoichiometric compositions [42, 43]. Although, earlier a spin-glass like magnetic phase has been observed due to the frustrated magnetic moments between AFM and FM phases [26], in our system from $M-T$ data (see Fig. 3.4 we do not see any signature of the spin-glass like behaviour below T_C.

3.5 Conclusions

In summary, we systematically studied the structural, electrical transport, and magnetic properties of the antiferromagnetic transition-metal monochalcogenide $Cr_{0.79}Se$. We identify that $Cr_{0.79}Se$ is synthesised into the same NiAs-type hexagonal crystal structure of the stoichiometric CrSe, unlike the other off-stoichiometric systems which form in differing crystal symmetries. Resistivity data suggest $Cr_{0.79}Se$ to be a Fermi-liquid-type metal at low temperatures, while at higher temperatures the resistivity depends sublinearly on the temperature. Above the room temperature the resistivity data hints at a MI transition, but need more studies to confirm the same. Magnetic measurements suggest for a transition from paramagnetic phase to an antiferromagnetic phase at a Néel temperature of 225 K. Importantly, a weak ferromagnetism is noticed below 100 K along with the antiferromagnetism. As a result, we notice significant exchange bias below 100 K due to the interaction between the ferro- and antiferromagnetic phases. Thus, for the first time we report on the presence of exchange bias in Cr_xSe systems."

References

[1] W. H. Meiklejohn, C. P. Bean, New magnetic anisotropy, Physical Review 105 (1957) 904.

[2] B. M. Wang, Y. Liu, P. Ren, B. Xia, K. B. Ruan, J. B. Yi, J. Ding, X. G. Li, L. Wang, Large Exchange Bias after Zero-Field Cooling from an Unmagnetized State, Phys Rev Lett 106 (2011) 077203.

[3] A. K. Nayak, M. Nicklas, S. Chadov, P. Khuntia, C. Shekhar, A. Kalache, M. Baenitz, Y. Skourski, V. K. Guduru, A. Puri, U. Zeitler, J. M. D. Coey, C. Felser, Design of compensated ferrimagnetic Heusler alloys for giant tunable exchange bias, Nat Mater 14 (2015) 679–684.

[4] A. Saha, S. Sohoni, R. Viswanatha, Interface Modeling Leading to Giant Exchange Bias from the CoO/CoFe2O4 Quantum Dot Heterostructure, The Journal of Physical Chemistry C 123 (2019) 2421–2427.

[5] F. Tian, Y. Li, Q. Zhao, M. Fang, R. Zhang, Z. Dai, Z. Yu, X. Ke, Y. Zhang, C. Zhou, S. Yang, Maximizing Zero-Field-Cooled Exchange Bias in Crystallized Co@CoO Nanocluster Assembled Thin Film by Varying Film Thickness, The Journal of Physical Chemistry C 125 (2021) 7337–7342.

[6] S. Parkin, Spintronic materials and devices: past, present and future!, in: IEDM Technical Digest. IEEE International Electron Devices Meeting, pp. 903–906.

[7] A. Hirohata, K. Takanashi, Future perspectives for spintronic devices, J. Phys. D: Appl. Phys. 47 (2014) 193001.

[8] S. E. Inderhees, J. A. Borchers, K. S. Green, M. S. Kim, K. Sun, G. L. Strycker, M. C. Aronson, Manipulating the Magnetic Structure of Co Core/CoO Shell Nanoparticles: Implications for Controlling the Exchange Bias, Phys Rev Lett 101 (2008) 117202.

[9] E. Lage, C. Kirchhof, V. Hrkac, L. Kienle, R. Jahns, R. Knöchel, E. Quandt, D. Meyners, Exchange biasing of magnetoelectric composites, Nat Mater 11 (2012) 523–529.

[10] G. C. Lavorato, E. L. Winkler, E. Lima, R. D. Zysler, Exchange-Coupled Bimagnetic Core–Shell Nanoparticles for Enhancing the Effective Magnetic Anisotropy, in: Exchange Bias, CRC Press, 2017, pp. 47–70.

[11] M. Perzanowski, M. Krupinski, A. Zarzycki, A. Dziedzic, Y. Zabila, M. Marszalek, Exchange Bias in the [CoO/Co/Pd]10 Antidot Large Area Arrays, ACS Applied Materials & Interfaces 9 (2017) 33250–33256.

[12] N. Song, H. Yang, Y. Luo, X. Ren, J. Zhou, S. Geng, G. Zhao, X. Zhang, Z. Cheng, Well-controlled exchange bias effect in MnO@Mn3O4 core-shell nanoparticles with an inverted coupling structures, AIP Advances 7 (2017) 045316.

[13] A. Wisniewski, I. Fita, R. Puzniak, V. Markovich, Exchange-Bias Effect in Bulk Perovskite Manganites, in: Exchange Bias, CRC Press, 2017, pp. 275–299.

[14] A. A. Belik, Origin of Magnetization Reversal and Exchange Bias Phenomena in Solid Solutions of $BiFeO_3$–$BiMnO_3$: Intrinsic or Extrinsic?, Inorganic Chemistry 52 (2013) 2015–2021.

[15] E. L. Fertman, A. V. Fedorchenko, V. A. Desnenko, V. V. Shvartsman, D. C. Lupascu, S. Salamon, H. Wende, A. I. Vaisburd, A. Stanulis, R. Ramanauskas, N. M. Olekhnovich, A. V. Pushkarev, Y. V. Radyush, D. D. Khalyavin, A. N. Salak, Exchange bias effect in bulk multiferroic $BiFe_{0.5}Sc_{0.5}O_3$, AIP Adv 10 (2020) 045102.

[16] F.-C. Hsu, J.-Y. Luo, K.-W. Yeh, T.-K. Chen, T.-W. Huang, P. M. Wu, Y.-C. Lee, Y.-L. Huang, Y.-Y. Chu, D.-C. Yan, M.-K. Wu, Superconductivity in the PbO type structure FeSe, Proceedings of the National Academy of Sciences 105 (2008) 14262–14264.

[17] G. Li, B. Zhang, T. Baluyan, J. Rao, J. Wu, A. A. Novakova, P. Rudolf, G. R. Blake, R. A. de Groot, T. T. M. Palstra, Metal–Insulator Transition Induced by Spin Reorientation in Fe_7Se_8 Grain Boundaries, Inorg Chem 55 (2016) 12912–12922.

[18] P. K. Maheshwari, R. Jha, B. Gahtori, V. P. S. Awana, Structural and Magnetic Properties of Flux-Free Large FeTe Single Crystal, J Supercond Novel Magn 28 (2015) 2893–2897.

[19] T. Hänke, U. R. Singh, L. Cornils, S. Manna, A. Kamlapure, M. Bremholm, E. M. J. Hedegaard, B. B. Iversen, P. Hofmann, J. Hu, Z. Mao, J. Wiebe, R. Wiesendanger, Reorientation of the diagonal double-stripe spin structure at Fe_yTe bulk and thin-film surfaces, Nat Commun 8 (2017).

[20] J. Zhang, F.-L. Liu, T.-P. Ying, N.-N. Li, Y. Xu, L.-P. He, X.-C. Hong, Y.-J. Yu, M.-X. Wang, J. Shen, W.-G. Yang, S.-Y. Li, Observation of two superconducting domes under pressure in tetragonal FeS, npj Quantum Materials 2 (2017).

[21] B. Sanyal, L. Bergqvist, O. Eriksson, Ferromagnetic materials in the zinc-blende structure, Phys Rev B 68 (2003) 054417.

[22] Y. Liu, S. K. Bose, J. Kudrnovský, First-principles theoretical studies of half-metallic ferromagnetism in CrTe, Phys. Rev. B 82 (2010) 094435.

[23] F. Lotgering, E. Gorter, Solid solutions between ferromagnetic and antiferromagnetic compounds with NiAs structure, J Phys Chem Solids 3 (1957) 238–249.

[24] T. Kamigaichi, K. ichi Masumoto, T. Hihara, Electrical Properties of Chromium Sulfides, J Phys Soc Jpn 15 (1960) 1355–1355.

[25] L. M. Corliss, N. Elliott, J. M. Hastings, R. L. Sass, Magnetic Structure of Chromium Selenide, Phys. Rev. 122 (1961) 1402–1406.

[26] Y. B. Li, Y. Q. Zhang, W. F. Li, D. Li, J. Li, Z. D. Zhang, Spin-glass-like behavior and electrical transport properties of $Cr_7(Se_{1-x}Te_x)_8$, Phys Rev B 73 (2006).

[27] H. Konno, M. Yuzuri, Ferrimagnetic Resonance on $CrS_{1.17}$, J Phys Soc Jpn 57 (1988) 621–625.

[28] L.-Y. Gan, Q. Zhang, C.-S. Guo, U. Schwingenschlögl, Y. Zhao, Two-Dimensional MnO_2/Graphene Interface: Half-Metallicity and Quantum Anomalous Hall State, The Journal of Physical Chemistry C 120 (2016) 2119–2125.

[29] B. Yan, C. Felser, Topological materials: Weyl semimetals, Annual Review of Condensed Matter Physics 8 (2017) 337–354.

[30] P. Li, J. Koo, W. Ning, J. Li, L. Miao, L. Min, Y. Zhu, Y. Wang, N. Alem, C.-X. Liu, et al., Giant room temperature anomalous Hall effect and tunable topology in a ferromagnetic topological semimetal Co_2MnAl, Nature communications 11 (2020) 3476.

[31] I. Tsubokawa, The Magnetic Properties of Chromium-Tellurium-Selenium System, Journal of the Physical Society of Japan 11 (1956) 662–665.

[32] J. Rodríguez-Carvajal, Recent advances in magnetic structure determination by neutron powder diffraction, Physica B: Condensed Matter 192 (1993) 55–69.

[33] G. Makovetskii, G. Shakhlevich, Magnetic properties of the $CrS_{1-x}Se_x$ system, physica status solidi (a) 47 (1978) 219–222.

[34] S. K. S. Patel, J.-H. Lee, M.-K. Kim, B. Bhoi, S.-K. Kim, Single-crystalline Gd-doped $BiFeO_3$ nanowires: R3c-to-Pn21a phase transition and enhancement in high-coercivity ferromagnetism, J. Mater. Chem. C 6 (2018) 526–534.

[35] S. Giri, M. Patra, S. Majumdar, Exchange bias effect in alloys and compounds, Journal of Physics: Condensed Matter 23 (2011) 073201.

[36] Y. Adachi, M. Ohashi, T. Kaneko, M. Yuzuri, Y. Yamaguchi, S. Funahashi, Y. Morii, Magnetic Structure of Rhombohedral Cr_2Se_3, J Phys Soc Jpn 63 (1994) 1548–1559.

[37] M. Chevreton, E. Bertaut, Etude de seleniures de chrome, C.R. Hebd. Seances Acad. Sci. 253 (1961) 145.

[38] R. Blachnik, P. Gunia, M. Fischer, H. Lutz, Das system chrom-selen, Journal of the Less Common Metals 134 (1987) 169–177.

[39] A. W. Sleight, T. A. Bither, Chromium chalcogenides prepared at high pressure and the crystal growth of chromium sesquisulfide, Inorg Chem 8 (1969) 566–569.

[40] K.-i. Masumoto, T. Hihara, T. Kamigaichi, Anomalies in Electrical Conductivity and Magnetic Susceptibility of Chromium Selenides, J. Phys. Soc. Jpn. 17 (1962) 1209–1210.

[41] J. Wu, C.-L. Zhang, J.-M. Yan, L. Chen, L. Guo, T.-W. Chen, G.-Y. Gao, L. Fei, W. Zhao, Y. Chai, et al., Magnetotransport and magnetic properties of the layered noncollinear antiferromagnetic Cr_2Se_3 single crystals, Journal of Physics: Condensed Matter 32 (2020) 475801.

[42] A. F. Andresen, E. Zeppezauer, T. Boive, B. Nordström, C.-I. Brändén, The Magnetic Structure of Cr_2Te_3, Cr_3Te_4, and Cr_5Te_6., Acta Chem Scand 24 (1970) 3495–3509.

[43] Y. Liu, C. Petrovic, Critical behavior of the quasi-two-dimensional weak itinerant ferromagnet trigonal chromium telluride $Cr_{0.62}Te$, Phys Rev B 96 (2017) 134410.

Chapter 4

Magnetoresistance behavior across the critical region in ferrimagnet $FeCr_2Te_4$ single crystal

4.1 Introduction

"Spin-dependent electron transport phenomena are emerging aspects of modern condensed matter physics, both theoretically and experimentally [1, 2]. Within this context, Magnetoresistance (MR) refers to the change in electrical resistivity when an external magnetic field is applied, given by the expression $\frac{\rho(H)-\rho(0)}{\rho(0)}$. It is a extensively studied phenomenon in condensed matter physics. The origin and nature of MR vary among different materials. The significant change in electrical resistance resulting from the application of an external magnetic field offers unique performance in magnetic sensors and information technology [3]. Various physical mechanisms have been proposed to describe MR in different materials. For instance, the giant magnetoresistance (GMR) is observed in Fe/Cr multilayered structures due to the spin-dependent transmission of conduction electrons through the Cr layer [4]. Large positive MR is reported in topological semimetals, attributed to relativistic quasiparticle excitations and high carrier mobility [5]. In hole-doped manganite perovskites, a large negative colossal magnetoresistance (CMR) effect near the Curie temperature (T_c) is observed, resulting from the mixed valency of Mn ions [6–8]. Similarly, large negative CMR effects have been noticed in pyrochlores and Cr-based chalcogen spinels [9, 10]. Recently, MR phenomena have also been observed in layered phosphide crystals, antiferromagnetic (AFM) insulators, and in the complex charge density wave regime of the $CeSb_xTe_{2-x-\delta}$ system [11–13]. The introduction of light Ti doping in Cr_2Se_3 enhances spin frustration and can lead to CMR in this material [14]. Furthermore, a CMR effect has been reported in the ferrimagnetic (FIM) insulator $Mn_3Si_2Te_6$ when an external magnetic field is applied along the magnetic hard axis

Results presented in this chapter are published in **Physics Letters A** , 486, 129101(2023).

[15, 16]. Chromium-based ternary compounds, denoted as ACr_2X_4 (where A represents a transition metal and X represents S, Se, or Te), have recently attracted considerable attention due to their diverse range of physical properties. These properties arise from the complex interplay between structural, spin, charge, and orbital degrees of freedom. Notable examples include the metallic $CuCr_2X_4$ [17], the semiconducting $CdCr_2Se_4$[18], and the half-metallic $HgCr_2Se_4$ (n-type), which exhibit ferromagnetic (FM) behavior [19]. On the other hand, the semiconducting $MnCr_2Se_4$ demonstrates FIM properties [20], while the insulating $ZnCr_2S_4$ displays AFM characteristics [21]. Some of these materials have garnered significant interest due to the presence of FM ordering and the potential emergence of Chern semimetallicity, as predicted by band structure calculations[22]. In these chalcogenide spinels, the FM order arises from superexchange interactions between the Cr ions' $3d$ electrons[23, 24], mediated by the anions. The exchange interaction between the s and d electrons results in a substantial spin splitting of the electronic bands. Depending on the strength of the spin-orbit coupling and exchange splitting, the chalcospinels can exhibit either magnetic semiconductor behavior [25] or Chern semimetal properties[26]. Additionally, compounds based on iron (Fe), such as $FeCr_2X_4$ (where X can be O, S, Se, or Te), display intriguing magnetic and electronic properties. For instance, $FeCr_2O_4$ exhibits FIM behavior and multiferroic ordering below 80 K [27–29]. $FeCr_2S_4$ is a multiferroic insulator that undergoes a FIM transition (T_c) below 170 K[30]. It also exhibits a metal-insulator transition near T_c with colossal magnetoresistance [31–33]. Lastly, $FeCr_2Se_4$ is an AFM insulator with a Neel temperature (T_N) of 218 K [34].

Recently, a noteworthy Fe-based ternary compound, $FeCr_2Te_4$, has been reported to undergo a FIM transition at a critical temperature (T_c) of 123 K. Through critical behavior analysis, it has been observed that $FeCr_2Te_4$ exhibits long-range exchange interactions with a three-dimensional Ising behavior at the critical temperature [35]. The research findings propose that the FIM interaction in $FeCr_2Te_4$ arises due to itinerant FM among antiferromagnetically coupled Cr-Fe-Cr trimers. Furthermore, this compound displays an anomalous Hall effect below 123 K, primarily dominated by an extrinsic skew-scattering mechanism rather than an intrinsic Karplus-Luttinger mechanism or an extrinsic side-jump mechanism [36]. Theoretical predictions suggest that $FeCr_2Te_4$ hosts a type-I Weyl point below the Fermi level (located at 44 meV) [37]. However, there has been no detailed study on the scattering mechanism of this material or the effects of a magnetic field on these scattering coefficients. Additionally, a comprehensive investigation of magnetotransport properties in $FeCr_2Te_4$ is still lacking.

To address these gaps, our study focuses on the structural, magnetic, electrical-transport, and magnetotransport properties of single crystals of $FeCr_2Te_4$. Specifically, we pay close attention to the magnetoresistance (MR) behavior in the vicinity of the critical temperature. Our findings reveal that the MR exhibits a negative maximum at T_c, indicating high sensitivity to external magnetic fields. Moreover, our Hall resistivity measurements suggest that the change in MR near T_c is directly associated with the

carrier concentration in $FeCr_2Te_4$.

4.2 Experimental Details

High-quality single crystals of $FeCr_2Te_4$ were grown using the solid-state reaction method, as described in the work by Liu et al. [35]. The constituent elements, Fe (99.99%), Cr (99.999%), and Te (99.99%) were weighed in stoichiometric ratios and mixed within an argon atmosphere inside a glove box. The resulting mixture was placed in an alumina crucible and then transferred to an evacuated quartz ampoule. The ampoule was subsequently heated in a muffle furnace at 1200°C for 12 hours, followed by a slow cooling process to 900°C at a rate of 1.5°C/hour. Finally, the ampoule was quenched in ice water.

The chemical composition of the obtained single crystals was determined using energy-dispersive X-ray analysis (EDAX) integrated with a scanning electron microscope (Quanta 250 FEG). Phase purity was confirmed through X-ray diffraction (XRD) measurements utilizing Cu k_α radiation with a Rigaku SmartLab 9KW instrument. Electrical resistivity measurements were carried out using the linear four-probe method, while Hall measurements were performed with the current and magnetic field directions as indicated in the inset of fig 4.9 (a). Both electrical transport and Hall measurements were conducted using a physical property measurement system (Quantum Design PPMS-9T) equipped with the ETO option. The four copper (Cu) leads were connected to the sample using silver epoxy (Epo-Tek H2OE). The temperature range during transport measurements varied from 2 K to 300 K, and to account for contact misalignment, the final Hall resistivity was anti-symmetrized using the formula $\left(\frac{\rho(H)-\rho(-H)}{2}\right)$.

DC magnetization measurements were performed using a Quantum Design PPMS-9T instrument equipped with a vibrating sample magnetometer (VSM). The temperature dependence of magnetization was investigated through the zero-field-cooled (ZFC) and field-cooled (FC) processes. Additionally, field-dependent magnetization was recorded up to 5 T.

4.3 Results and discussions

The X-ray diffraction (XRD) pattern presented in fig. 4.1 (a) confirms that $FeCr_2Te_4$ single crystals crystallize in a monoclinic crystal structure with a space group of $I2/m$. The pattern exhibits reflections corresponding to the $(00l)$ plane, indicating that the crystal growth occurs parallel to the c-axis, while the flat plane of the crystal corresponds to the ab plane. The as-grown single crystals exhibit a platelike form with a shiny metallic luster. To analyze the XRD pattern of crushed single crystals, Rietveld refinement was employed, as shown in fig.4.2. The obtained lattice parameters, a = 6.8942 Å, b = 3.9509 Å, c = 12.0605 Å, and β= 89.593°, match those reported previously [35]. The left-side inset of fig. 4.1 (a) illustrates the typical size of an as-grown single crystal. The

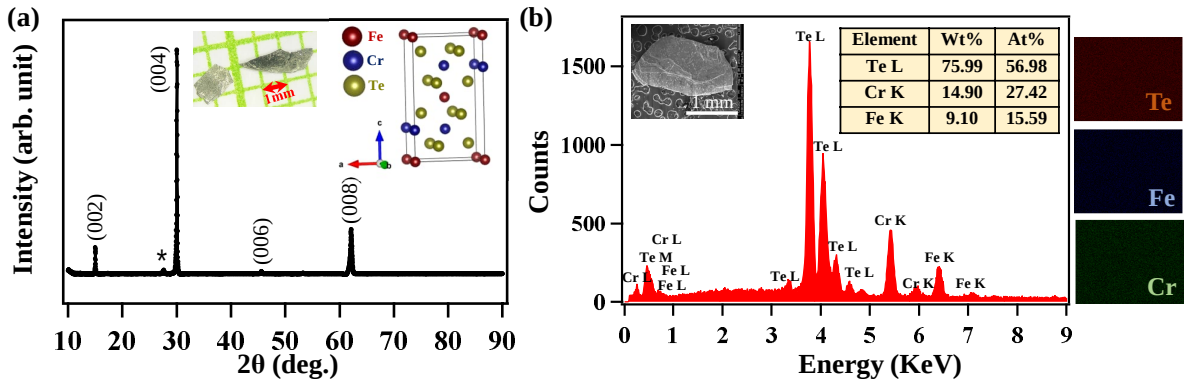

Figure 4.1: (a) Single crystal XRD pattern of $FeCr_2Te_4$ having $(00l)$ reflections. Impurity peak of FeTe is indicated by * mark. Inset shows the optical image of the typical $FeCr_2Te_4$ single crystal and crystal structure of $FeCr_2Te_4$. (b) Energy dispersive X-ray analysis (EDAX) data of cleaved $FeCr_2Te_4$ single crystal. Left side inset shows the SEM image of single crystal. Right side inset shows atomic and weight percentages of elements in $FeCr_2Te_4$ single crystal. Right panel shows EDAX mapping of elements Fe, Cr, and Te in $FeCr_2Te_4$ single crystal.

right-side inset in fig. 4.1 (a) illustrates the unit cell representation of $FeCr_2Te_4$. The chemical composition of the single crystal was determined to be $Fe_{1.09}Cr_{1.92}Te_{3.96}$ (or $Fe_{1.08}Cr_{1.92}Te_4$) using EDAX analysis. A recent study by Liu et al. [35] reported the magnetism of $FeCr_2Te_4$ with a Fe:Cr:Te ratio of 0.99(2):1.90(2):4.0(1). In comparison, our system contains an excess of Fe when compared to the previous study. Figure. 4.1 (b) presents the EDAX spectra of $FeCr_2Te_4$, with the left-side inset showing the SEM image of the as-grown single crystal and the right-side inset displaying the obtained atomic and weight percentages. The right panel of fig. 4.1 (b) exhibits the EDAX mapping of the elements Fe, Cr, and Te in the $FeCr_2Te_4$ single crystal. The homogeneous distribution of these elements is confirmed through EDAX mapping.

4.3.1 Structural analysis

For structural investigation and phase purity, the room temperature x-ray diffraction (XRD) pattern of the sample is taken. The XRD pattern is refined using FULLPROF software. The powder X-ray diffraction pattern of crushed $FeCr_2Te_4$ single crystals can be fitted by using a monoclinic structure with the I2/m (monoclinic) space group with FeTe phase (tetragonal), confirming the main phase of $FeCr_2Te_4$ with FeTe impurity, displayed in fig. 4.2

4.4 Magnetism

Figure 4.3 (a) illustrates the magnetization as a function of temperature with an applied magnetic field of 500 Oe parallel to the crystallographic c-axis in both zero-field-cooled

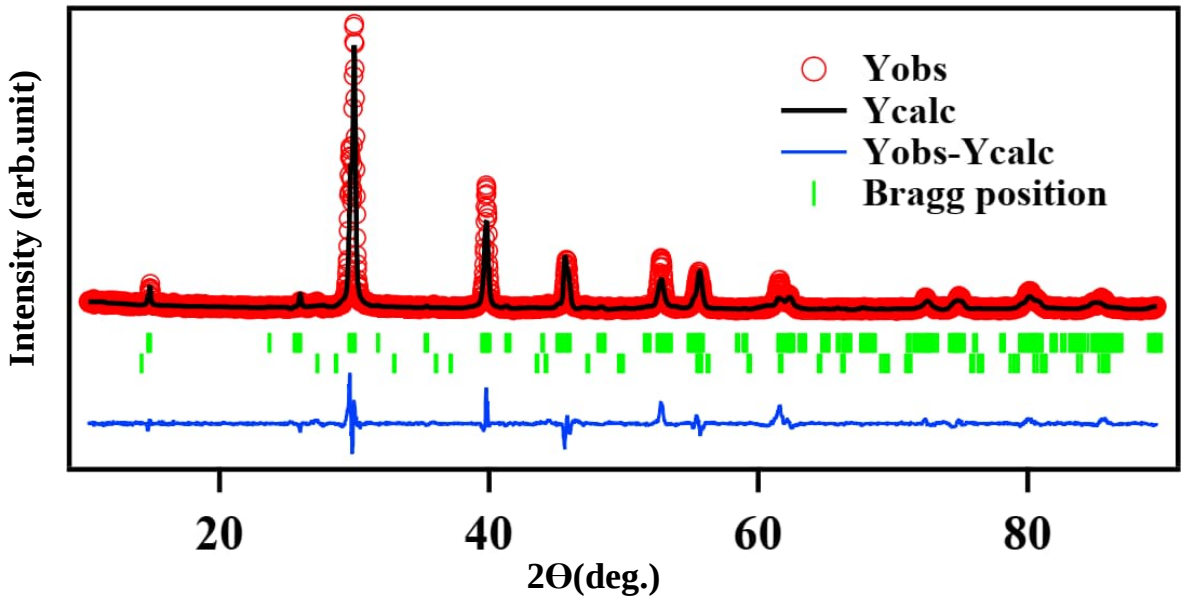

Figure 4.2: X-ray diffraction spectra for crushed $FeCr_2Te_4$ single crystal samples with the Rietveld refinement. The red circle illustrates the observed intensity and the black solid line represents the Rietveld refinement fit. The difference between experimental and calculated data was demonstrated by solid blue line. The vertical tick marks (green) show Bragg reflections of I2/m space group (upper vertical tick marks) and FeTe impurity (lower vertical tick marks).

(ZFC) and field-cooled (FC) modes. The inset in fig. 4.3 (a) displays the dM/dT plot. Figure 4.3 (b) presents the magnetization (M) as a function of temperature with an applied magnetic field of 500 Oe perpendicular to the crystallographic c-axis in ZFC and FC mode. The inset of fig. 4.3(b) shows the first derivative of magnetization (dM/dT).

Both the out-of-plane ($H \parallel c$) and in-plane ($H \perp c$) magnetization measurements indicate a rapid increase in M near 123 K, attributed to the paramagnetic (PM) to FIM transition (T_c) [35]. The dM/dT plot shows a dip at 123 K in both directions, further confirming the PM to FIM transition in $FeCr_2Te_4$. The in-plane magnetization is considerably smaller than the out-of-plane magnetization, suggesting the presence of significant magnetic anisotropy in this system, as shown in fig. 4.3. Field-dependent magnetization data at 5K parallel to the c-direction is presented in the inset of fig. 4.3(a), and perpendicular to the c-direction in the inset of fig. 4.3(b), confirming the large magnetic anisotropy and the easy axis along the c-direction. To investigate the exact magnetic interaction in the system, we studied the inverse of susceptibility ($1/\chi$) as a function of temperature for $H \parallel c$ and $H \perp c$ directions. The plot of $1/\chi$ vs. T exhibits a hyperbolic nature instead of a straight line above T_c [38] (measured at 500 Oe) (shown in fig. 4.4). These observations imply the presence of FIM exchange interaction [39]. In $FeCr_2Te_4$, Fe and Cr atoms occupy different crystallographic sites and have opposite spin orientations. We have got positive χ_0 value via fitting this expression $\chi = \chi_0 + \frac{C}{T-\theta}$, where C is the Curie constant and θ is the Curie-Weiss temperature. From C we have estimated the magnetic

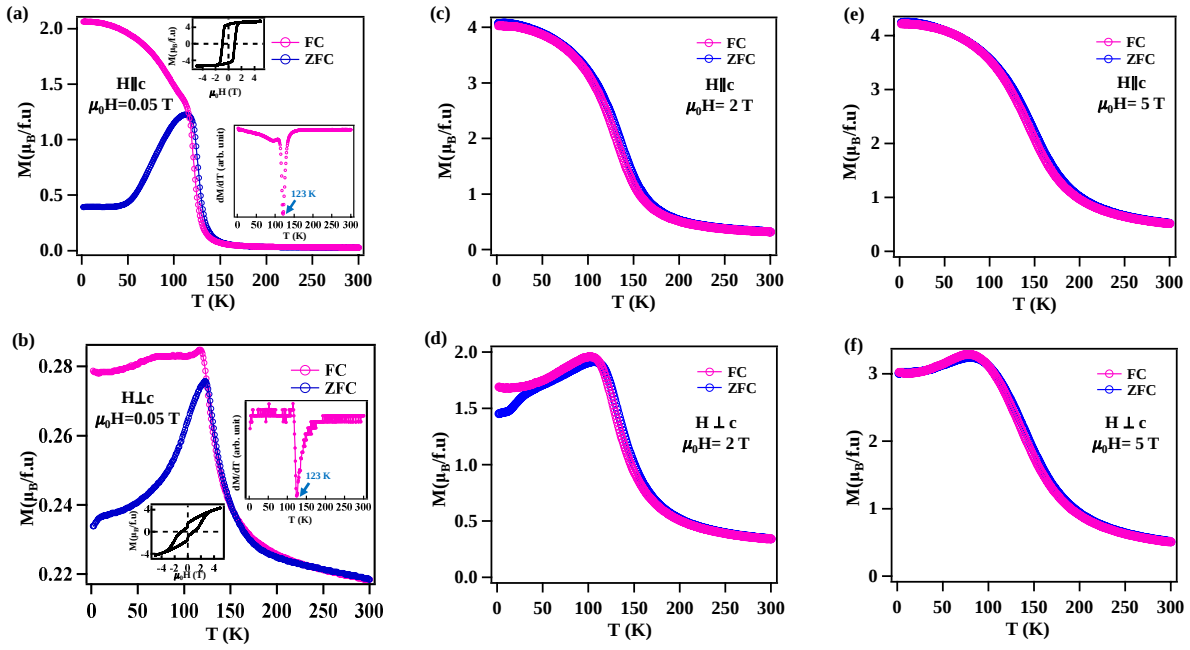

Figure 4.3: (a) Temperature dependent magnetization data at a field of 500 Oe for $H \| c$. The above inset shows the field dependence of magnetization data at 5K for $H \| c$ and The below inset shows transition temperature at 123 K from PM to FIM transition.(b) Magnetization versus temperature data measured at a field of 500 Oe. The right inset shows the first derivative curve dM/dT where the minimum corresponds to PM to FIM transition temperature 123 K and field dependence of magnetization data at 5K for $H \perp c$.(c) Temperature dependent magnetization data at a field of 2T for $H \| c$ and (d)2T for $H \perp c$. (e) Temperature dependent magnetization data at a field of 5T for $H \| c$ and (f) 5T for $H \perp c$.

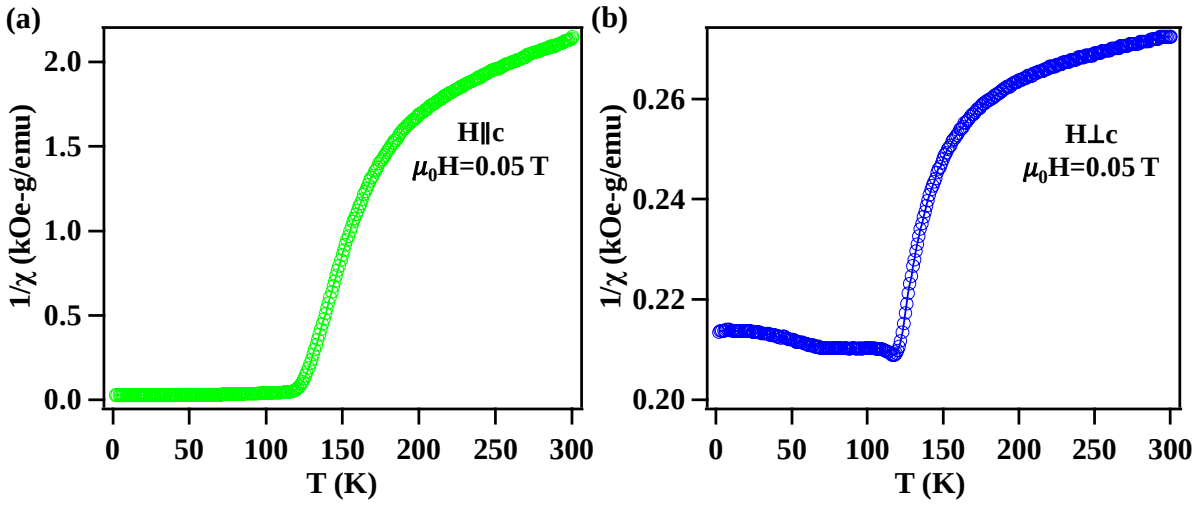

Figure 4.4: (a) Inverse susceptibility $(1/\chi)$ as a function of temperature for $H \parallel c$ and $H \perp c$ in FC mode.

moment(shown in fig. 4.5). The positive χ_0 term may be attributed to Pauli contribution, but this aspect is beyond the scope of our discussion. Temperature-dependent magneti-

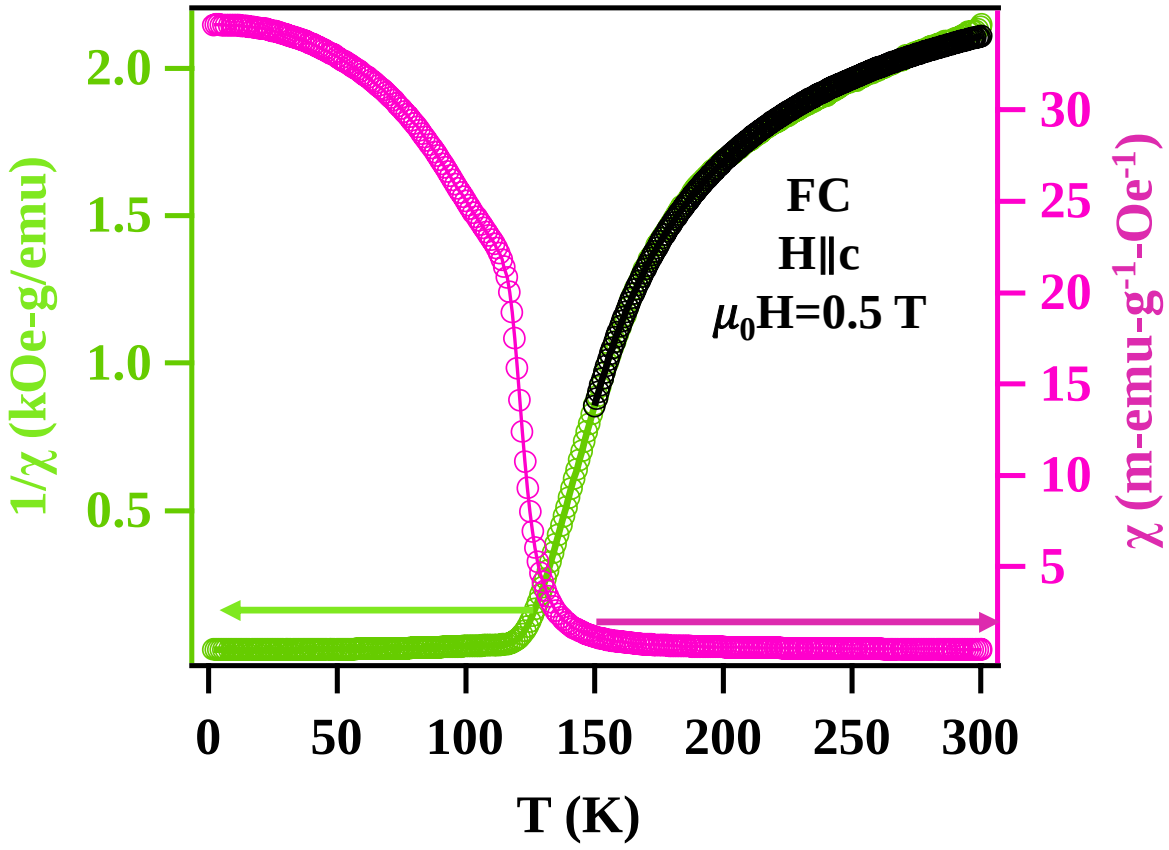

Figure 4.5: Susceptibility (χ) and inverse susceptibility ($1/\chi$) as a function of temperature for $H \parallel c$ in FC mode. The black curve is a susceptibility fitting with the Curie-Weiss law from 150 to 300 K.

zation data at a field of 2T fig. 4.3(c)and 5T fig. 4.3(e) were obtained for $H \parallel c$. Similarly, temperature-dependent magnetization data at a field of 2T fig. 4.3(d)and 5T fig. 4.3(f) were acquired for $H \perp c$. The peak feature around the magnetic transition temperature (T_c) is suppressed with the application of an external magnetic field. Bifurcation in $H \perp c$ is observed at 2T fig. 4.3(d), but it is not visible at 5T fig. 4.3(f) [40]. For a more comprehensive understanding of the magnetism in this material, neutron scattering experiments can be conducted.

4.5 Transport

According to Matthiessen's rule, the total resistivity of a metallic sample is determined by the sum of all scattering mechanisms. This can be expressed as follows [41, 42] $\rho(T) = \rho_0 + \rho_{e-m} + \rho_{e-p} + \rho_{e-e}$ Here, ρ_0 represents the residual resistivity caused by lattice defects, disorder, and imperfections in the lattice. On the other hand, ρ_{e-m}, ρ_{e-p}, and ρ_{e-e} correspond to electron-magnon, electron-phonon, and electron-electron scattering, respectively. The resistivity term ρ_{e-p} exhibits a linear dependence on temperature, while

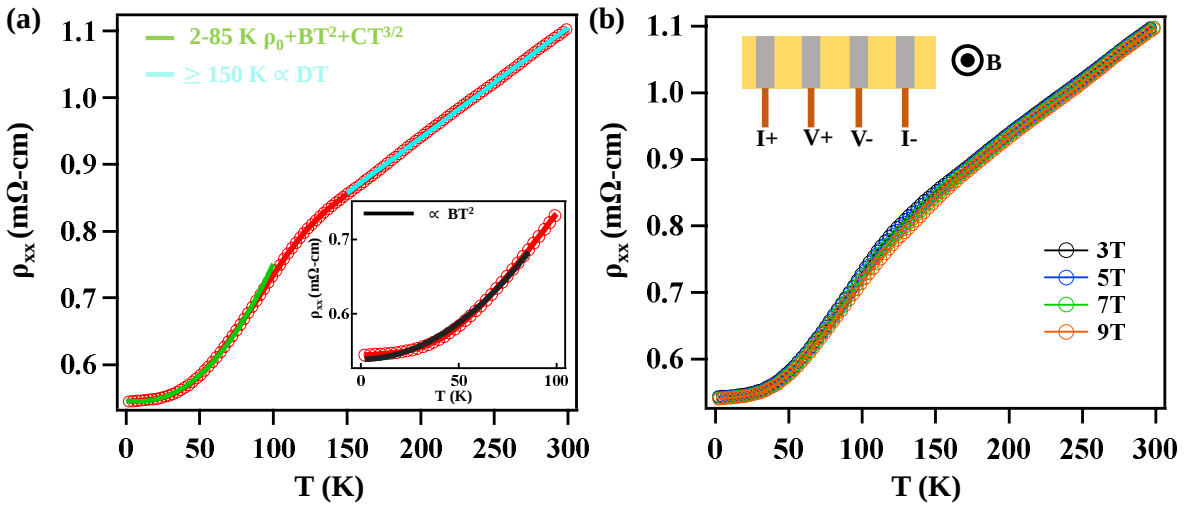

Figure 4.6: (a) Temperature-dependent electrical resistivity of $FeCr_2Te_4$. A green solid curve represents $\rho_0 + BT^2 + CT^{3/2}$ law fitting up to 85 K and the sky solid line represents linear fitting above 150 K. The inset shows the plot of ρ vs T^2 fitting that is not fitted . (b) ρ_{xx} vs T are recorded at constant magnetic fields. Inset shows schematic of linear four probe connection and direction of applied magnetic field.

both ρ_{e-e} and ρ_{e-m} vary quadratically with temperature. The temperature dependent resistivity is fitted within the temperature range of 2 K to 85 K with the equation $\rho(T) = \rho_0 + BT^2 + CT^{3/2}$ [43] as shown in fig. 4.6(a). Here, $T^{3/2}$ term elaborates the contribution of spin fluctuation scattering. The inset in fig. 4.6(a) shows that the low temperature region is not fitted well using equation $\rho_0 + BT^2$.

Figure 4.6(b) shows the resistivity data at different magnetic fields measured along crystallographic c axis. The fitting within the temperature range of 2 K to 85 K in zero magnetic field resistivity yields $\rho_0 = 0.545 \times 10^{-3}\Omega - cm$, $B = 3.31 \times 10^{-8}\Omega - cmK^{-2}$, $C = 1.25 \times 10^{-7}\Omega - cmK^{-3/2}$. There is an order of magnitude difference between the amplitudes of the spin-fluctuation and electron-magnon terms. This suggests that interaction between conduction electrons and localized spins could not be understood as a small perturbations to a system of free electrons [44]. In the high-temperature region above 150 K, the resistivity shows a linear relationship with temperature, indicating that electron-phonon scattering dominates the resistivity at high temperatures. The fitting using the equation $\rho(T) = \rho_0 + BT^2 + CT^{3/2}$ [43] has also been performed within the temperature range of 2 K to 85 K in the presence of applied magnetic fields, although these fittings are not shown here. Generally, the T^2 dependence of resistivity arises from electron-electron and electron-magnon scattering. It should be noted that electron-electron scattering is not sensitive to magnetic fields, whereas the strength of electron-magnon scattering is suppressed by applied magnetic fields [45]. Also, T^3 (s-d scattering) or T^5 (electron-phonon scattering) laws are not observed in the low temperature resistivity data fitting (shown in fig. 4.7).

Using this equation $\rho(T) = \rho_0 + BT^3 + CT^2$ we have got

$\rho_0 = 0.543 \times 10^{-3}\Omega - cm$, $B = 9.96 \times 10^{-11}\Omega - cmK^{-3}$, $C = 1.14 \times 10^{-8}\Omega - cmK^{-2}$. Using this equation $\rho(T) = \rho_0 + BT^5 + CT^2$ we have got

$\rho_0 = 0.541 \times 10^{-3}\Omega - cm$, $B = 5.630 \times 10^{-15}\Omega - cmK^{-5}$, $C = 1.673 \times 10^{-8}\Omega - cmK^{-2}$. So, coefficient of s-d scattering and electron-phonon scattering are very less. Rather, $T^{3/2}$+T^2 fitting is properly fitted.

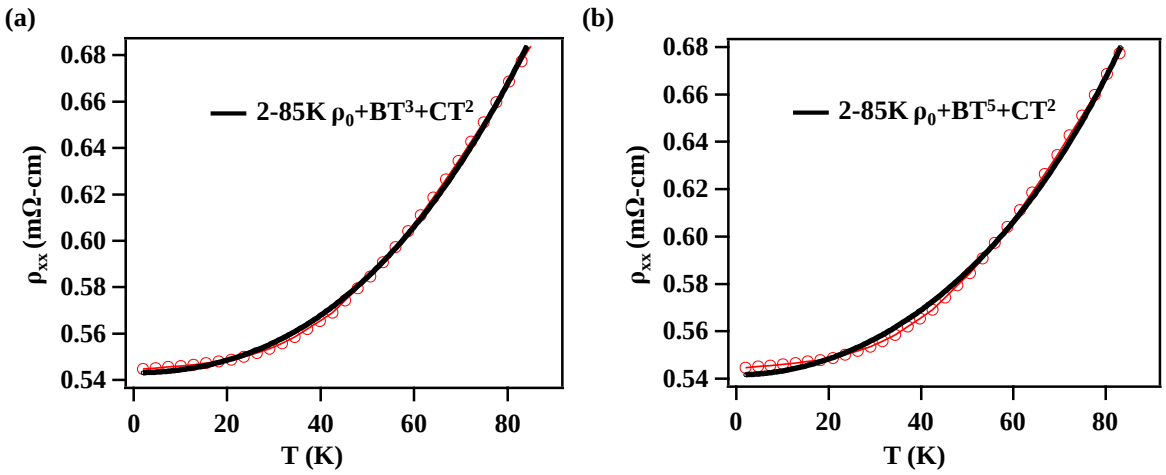

Figure 4.7: (a) T^3 and (b) T^5 fitting are shown.

Table 1

Strength of the scattering coefficients are tabulated below:			
Magnetic Field(T)	Residual Resistivity(mΩ-cm)	B($10^{-8}\Omega - cmK^{-2}$)	$C(10^{-7}\Omega - cmK^{-3/2})$
0	0.000545	3.31	1.25
3	0.000544	3.25	1.22
5	0.000543	3.22	1.21
7	0.000542	3.11	1.15
9	0.000540	2.78	0.913

To elucidate the origin of the T^2 law, the strength of scattering dependent on magnetic field has been estimated through resistivity measurements at various magnetic field strengths. The coefficient (B) of the T^2 term, obtained from fittings using the equation $\rho(T) = \rho_0 + BT^2 + CT^{3/2}$ [43] within the temperature range of 2-85 K under different externally applied magnetic fields ($\mu_0 H$), is plotted against $\mu_0 H$ as depicted in fig. 4.8 (b). This plot demonstrates that B decreases as the magnetic field increases, suggesting that the T^2 dependence of resistivity arises from electron-magnon scattering. Earlier studies have also reported the presence of electron-magnon scattering in this system [36]. Furthermore, the residual resistivity and spin-fluctuation scattering exhibit changes with

magnetic field, as illustrated in fig. 4.8 (a) and (c) respectively. The scattering coefficients are provided in the Table 1.

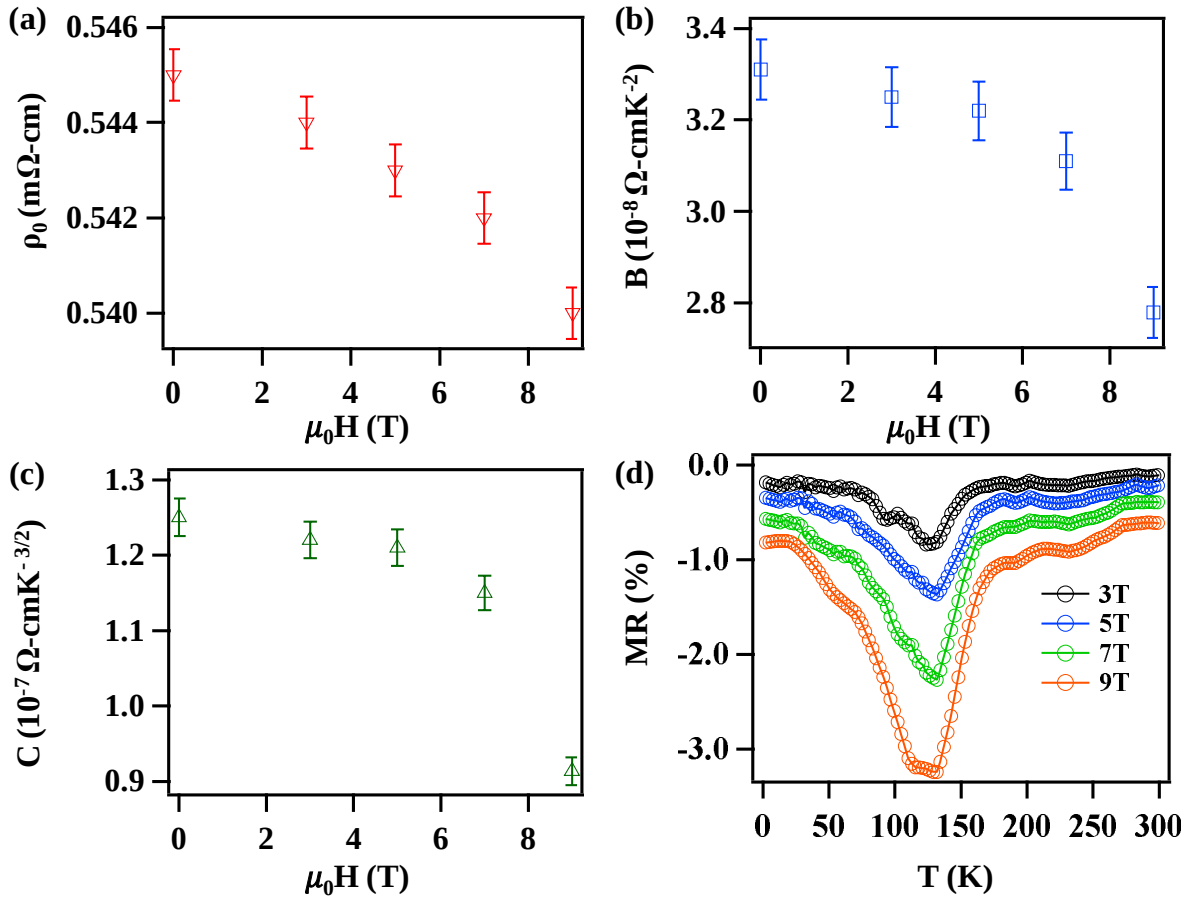

Figure 4.8: Variation of (a) residual resistivity (ρ_0). (b) electron-magnon scattering strength (B). (c) spin-fluctuation scattering strength (C) with magnetic field up to 85 K. (d) Temperature dependent magnetoresistance measurement at different fields .

Temperature-dependent magnetoresistance (MR) measurements for various applied magnetic fields are displayed in fig. 4.8 (d), revealing a dip (negative maximum) in close proximity to T_c, which is associated with the transition from PM to FIM transition.

To investigate the magnetoresistance (MR) behavior observed near T_c, Hall measurements have been conducted on the compound. Fig. 4.9(a) presents the field-dependent Hall resistivity at different temperatures. Below T_c, in the FIM state, ρ_{xy} exhibits two distinct regions. In the low field region, it rises sharply before becoming linear in the high field region, indicating the presence of an anomalous Hall effect in the $FeCr_2Te_4$ single crystal.

In general, the Hall resistivity in a ferromagnet can be expressed as $\rho_{xy} = \rho^0_{xy} + \rho^A_{xy} = R_0\mu_0 H + R_s\mu_0 M$, where R_0 represents the ordinary Hall coefficient and R_s denotes the anomalous Hall coefficient [46–49]. The slope of ρ_{xy} provides information about the charge carrier density, while the sign of the slope indicates the type of charge carriers. The positive Hall coefficient confirms the presence of hole-type carriers. $\rho^A_{xy}(H)$ was

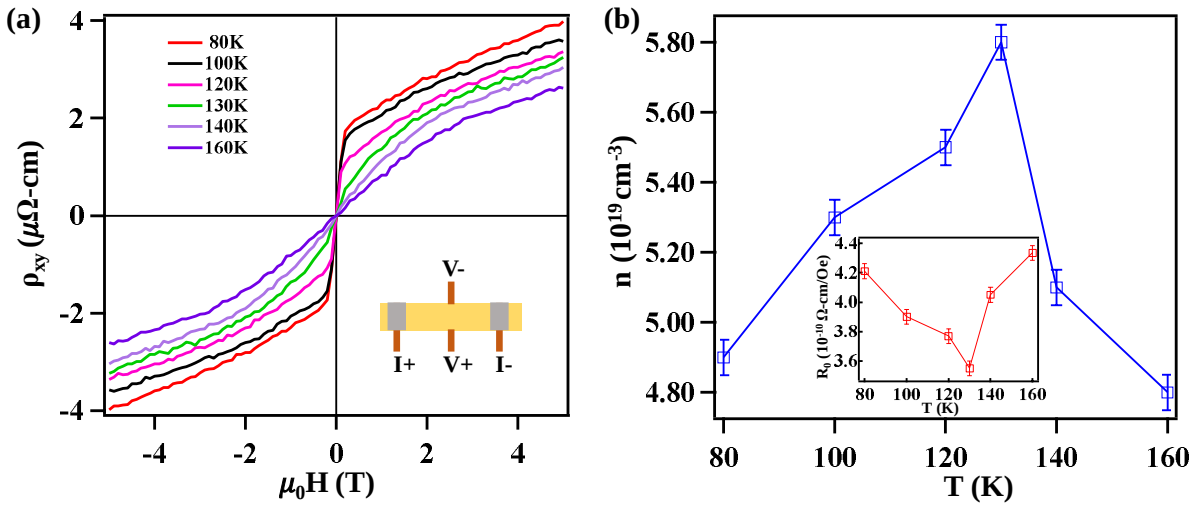

Figure 4.9: (a) Magnetic field dependence of Hall resistivity at different temperatures. Inset shows schematic of four probe connections and direction of applied magnetic field along c direction for Hall measurements.(b) Temperature dependence of carrier concentration (n). Inset shows the ordinary Hall coefficient (R_0) vs temperature plot.

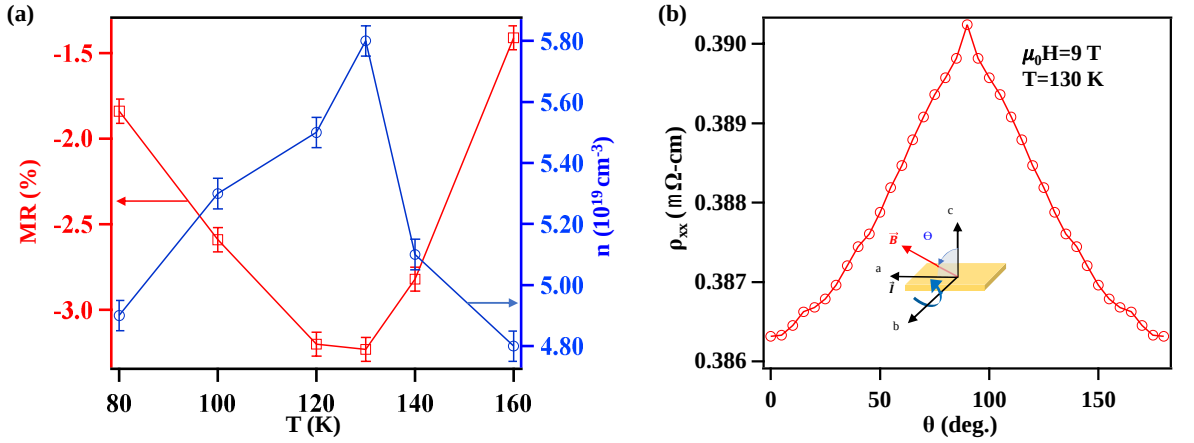

Figure 4.10: (a) MR at 9 T and carrier concentration (n) as a function of temperature.(b) Angle dependent magnetoresistance (AMR) measurement at temperature of 130 K with applied magnetic field of 9 T.

determined by extrapolating the linear fit to the high field region of the ρ_{xy} data back to the zero field. The charge carrier concentration ($n = \frac{1}{R_0 e}$) was found to be 0.49×10^{20} cm^{-3} at 80 K. The derived carrier concentration (n) exhibits variations around T_c and decreases above T_c, as depicted in fig. 4.9(b) [50].

It is observed that the MR displays a maximum value in close proximity to T_c, as shown in fig. 4.10 (a). Additionally, the carrier concentration reaches its maximum value near T_c, as depicted in fig. 4.10(a). This suggests a potential correlation between the MR behavior and the carrier concentration near T_c. Furthermore, in Fig. 4.10(b), the angle-dependent MR (AMR) measured at 130 K exhibits slight anisotropy, which arises from spin-orbit coupling [51, 52].

4.6 Conclusions

In conclusion, we have conducted a comprehensive investigation of the electrical transport, magnetotransport, and magnetic properties in $FeCr_2Te4$ single crystal. The temperature-dependent resistivity, ρ_{xx}, exhibits the influence of electron-magnon scattering and spin fluctuations scattering below the magnetic ordering temperature. Furthermore, we have examined the impact of increasing magnetic field on different scattering mechanisms in this compound. The temperature-dependent MR demonstrates a maximum negative MR in close proximity to T_c, which amplifies with higher magnetic field strengths. Notably, our Hall resistivity measurements have unveiled a direct correlation between the observed MR behavior across T_c and the carrier concentration in this compound. Overall, our study on $FeCr_2Te_4$ presents a promising platform for investigating spin-dependent transport phenomena both theoretically and experimentally."

References

[1] Felser, Claudia and Fecher, Gerhard H and Balke, Benjamin, Spintronics: a challenge for materials science and solid-state chemistry, Angewandte Chemie International Edition 46 (2007) 668–699.

[2] G. Li, B. Zhang, T. Baluyan, J. Rao, J. Wu, A. A. Novakova, P. Rudolf, G. R. Blake, R. A. de Groot, T. T. M. Palstra, Metal–Insulator Transition Induced by Spin Reorientation in Fe_7Se_8 Grain Boundaries, Inorg Chem 55 (2016) 12912–12922.

[3] G. A. Prinz, Magnetoelectronics, Science 282 (1998) 1660–1663.

[4] R. E. Camley, J. Barnaś, Theory of giant magnetoresistance effects in magnetic layered structures with antiferromagnetic coupling, Phys. Rev. Lett. 63 (1989) 664–667.

[5] M. N. Ali, J. Xiong, S. Flynn, J. Tao, Q. D. Gibson, L. M. Schoop, T. Liang, N. Haldolaarachchige, M. Hirschberger, N. P. Ong, et al., Large, non-saturating magnetoresistance in wte_2, Nature 514 (2014) 205–208.

[6] M. B. Salamon, M. Jaime, The physics of manganites: Structure and transport, Rev. Mod. Phys. 73 (2001) 583–628.

[7] B. Raveau, A. Maignan, C. Martin, M. Hervieu, Colossal magnetoresistance manganite perovskites: relations between crystal chemistry and properties, Chemistry of materials 10 (1998) 2641–2652.

[8] Raveau, B and Hervieu, M and Maignan, A and Martin, C, The route to CMR manganites: what about charge ordering and phase separation? Basis of a presentation given at Materials Discussion No. 3, 26–29 September, 2000, University of Cambridge, UK., Journal of Materials Chemistry 11 (2001) 29–36.

[9] P. Majumdar, P. Littlewood, Magnetoresistance in Mn Pyrochlore: Electrical Transport in a Low Carrier Density Ferromagnet, Phys. Rev. Lett. 81 (1998) 1314–1317.

[10] A. P. Ramirez, R. J. Cava, J. Krajewski, Colossal magnetoresistance in Cr-based chalcogenide spinels, Nature 386 (1997) 156–159.

[11] Wang, Zhi-Cheng and Rogers, Jared D and Yao, Xiaohan and Nichols, Renee and Atay, Kemal and Xu, Bochao and Franklin, Jacob and Sochnikov, Ilya and Ryan, Philip J and Haskel, Daniel and others, Colossal magnetoresistance without mixed valence in a layered phosphide crystal, Advanced Materials 33 (2021) 2005755.

[12] P. Rosa, Y. Xu, M. Rahn, J. Souza, S. Kushwaha, L. Veiga, A. Bombardi, S. Thomas, M. Janoschek, E. Bauer, et al., Colossal magnetoresistance in a nonsymmorphic antiferromagnetic insulator, npj Quantum Materials 5 (2020) 1–6.

[13] R. Singha, K. J. Dalgaard, D. Marchenko, M. Krivenkov, E. D. Rienks, M. Jovanovic, S. M. Teicher, J. Hu, T. H. Salters, J. Lin, et al., Colossal magnetoresistance in the multiple wave vector charge density wave regime of an antiferromagnetic dirac semimetal, Science Advances 9 (2023) eadh0145.

[14] Zhang, Shu-Juan and Yan, Jian-Min and Tang, F and Wu, Jin and Dong, Wei-Qi and Zhang, Dan-Wen and Luo, Fu-Sheng and Chen, Lei and Fang, Y and Zhang, Tao and others, Colossal Magnetoresistance in Ti Lightly Doped Cr_2Se_3 Single Crystals with a Layered Structure, ACS Applied Materials & Interfaces 13 (2021) 58949–58955.

[15] Y. Ni, H. Zhao, Y. Zhang, B. Hu, I. Kimchi, G. Cao, Colossal magnetoresistance via avoiding fully polarized magnetization in the ferrimagnetic insulator mn 3 si 2 te 6, Physical Review B 103 (2021) L161105.

[16] F. Ye, M. Matsuda, Z. Morgan, T. Sherline, Y. Ni, H. Zhao, G. Cao, Magnetic structure and spin fluctuations in the colossal magnetoresistance ferrimagnet $mn_3si_2te_6$, Phys. Rev. B 106 (2022) L180402.

[17] T. Kanomata, H. Ido, T. Kaneko, Effect of Pressure on Curie Temperature of Calcogenide Spinels $CuCr_2X_4$ (X=S, Se and Te), Journal of the Physical Society of Japan 29 (1970) 332–335.

[18] N. Menyuk, K. Dwight, R. J. Arnott, A. Wold, Ferromagnetism in $CdCr_2Se_4$ and $CdCr_2S_4$, Journal of Applied Physics 37 (1966) 1387–1388.

[19] S. Yang, Z. Li, C. Lin, C. Yi, Y. Shi, D. Culcer, Y. Li, Unconventional Temperature Dependence of the Anomalous Hall Effect in $HgCr_2Se_4$, Phys. Rev. Lett. 123 (2019) 096601.

[20] V. Tsurkan, M. Mücksch, V. Fritsch, J. Hemberger, M. Klemm, S. Klimm, S. Körner, H.-A. Krug von Nidda, D. Samusi, E.-W. Scheidt, A. Loidl, S. Horn, R. Tidecks, Magnetic, heat capacity, and conductivity studies of ferrimagnetic $MnCr_2Se_4$ single crystals, Phys. Rev. B 68 (2003) 134434.

[21] J. Hemberger, T. Rudolf, H.-A. Krug von Nidda, F. Mayr, A. Pimenov, V. Tsurkan, A. Loidl, Spin-Driven Phonon Splitting in Bond-Frustrated $ZnCr_2Se_4$, Phys. Rev. Lett. 97 (2006) 087204.

[22] T. Guan, C. Lin, C. Yang, Y. Shi, C. Ren, Y. Li, H. Weng, X. Dai, Z. Fang, S. Yan, P. Xiong, Evidence for Half-Metallicity in n-type $HgCr_2Se_4$, Phys. Rev. Lett. 115 (2015) 087002.

[23] Goldstein, L and Gibart, P and Selmi, A, Transport properties of the ferromagnetic semiconductor $HgCr_2Se_4$, Journal of Applied Physics 49 (1978) 1474–1476.

[24] P. K. Baltzer, P. J. Wojtowicz, M. Robbins, E. Lopatin, Exchange Interactions in Ferromagnetic Chromium Chalcogenide Spinels, Phys. Rev. 151 (1966) 367–377.

[25] H. W. Lehmann, Semiconducting Properties of Ferromagnetic $CdCr_2Se_4$, Phys. Rev. 163 (1967) 488–496.

[26] G. Xu, H. Weng, Z. Wang, X. Dai, Z. Fang, Chern Semimetal and the Quantized Anomalous Hall Effect in $HgCr_2Se_4$, Phys. Rev. Lett. 107 (2011) 186806.

[27] K. Tsuda, D. Morikawa, Y. Watanabe, S. Ohtani, T. Arima, Direct observation of orbital ordering in the spinel oxide $FeCr_2O_4$ through electrostatic potential using convergent-beam electron diffraction, Phys. Rev. B 81 (2010) 180102.

[28] K. Singh, A. Maignan, C. Simon, C. Martin, $FeCr_2O_4$ and $CoCr_2O_4$ spinels: Multiferroicity in the collinear magnetic state?, Applied Physics Letters 99 (2011) 172903.

[29] E. S. Bozin, W. G. Yin, R. J. Koch, M. Abeykoon, Y. S. Hor, H. Zheng, H. C. Lei, C. Petrovic, J. F. Mitchell, S. J. L. Billinge, Local orbital degeneracy lifting as a precursor to an orbital-selective Peierls transition, Nature Communications 10 (2019).

[30] J. Bertinshaw, C. Ulrich, A. Günther, F. Schrettle, M. Wohlauer, S. Krohns, M. Reehuis, A. J. Studer, M. Avdeev, D. V. Quach, J. R. Groza, V. Tsurkan, A. Loidl, J. Deisenhofer, $FeCr_2S_4$ in magnetic fields: possible evidence for a multiferroic ground state, Scientific Reports 4 (2014).

[31] A. P. Ramirez, R. J. Cava, J. Krajewski, Colossal magnetoresistance in Cr-based chalcogenide spinels, Nature 386 (1997) 156–159.

[32] J.-S. Kang, G. Kim, H. J. Lee, H. S. Kim, D. H. Kim, S. W. Han, S. J. Kim, C. S. Kim, H. Lee, J.-Y. Kim, B. I. Min, Synchrotron radiation spectroscopy study of $FeCr_2X_4$ (X=S and Se), Journal of Applied Physics 103 (2008) 07D717.

[33] S. Sarkar, M. De Raychaudhury, I. Dasgupta, T. Saha-Dasgupta, Electronic structure of $FeCr_2Se_4$: Evidence of Coulomb enhanced spin-orbit splitting, Phys. Rev. B 80 (2009) 201101.

[34] B. I. Min and Seung Su Baik and H. C. Choi and S. K. Kwon and J.-S. Kang, Electronic structures of magnetic semiconductors $FeCr_2Se_4$ and $Fe_0.5Cu_0.5Cr_2Se_4$, New Journal of Physics 10 (2008) 055014.

[35] Y. Liu, R. J. Koch, Z. Hu, N. Aryal, E. Stavitski, X. Tong, K. Attenkofer, E. S. Bozin, W. Yin, C. Petrovic, Three-dimensional Ising ferrimagnetism of Cr-Fe-Cr trimers in $FeCr_2Te_4$, Phys. Rev. B 102 (2020) 085158.

[36] Y. Liu, H. Tan, Z. Hu, B. Yan, C. Petrovic, Anomalous Hall effect in the weak-itinerant ferrimagnet $FeCr_2Te_4$, Phys. Rev. B 103 (2021) 045106.

[37] H. Tan, Y. Liu, B. Yan, Unconventional anomalous Hall effect from magnetization parallel to the electric field, Phys. Rev. B 103 (2021) 214438.

[38] L. Néel, Antiferromagnetism and ferrimagnetism, Proceedings of the Physical Society. Section A 65 (1952) 869.

[39] S. Mugiraneza, A. M. Hallas, Tutorial: a beginner's guide to interpreting magnetic susceptibility data with the Curie-Weiss law, Communications Physics 5 (2022) 95.

[40] V. P. S. Awana, I. Nowik, A. Pal, K. Yamaura, E. Takayama-Muromachi, I. Felner, Magnetic phase transitions in SmCoAsO, Phys. Rev. B 81 (2010) 212501.

[41] J. M. Ziman, Electrons and phonons: the theory of transport phenomena in solids, Oxford university press, 2001.

[42] D. Pines, P. Noziéres, The Theory of Quantum Liquids, CRC Press, 2018.

[43] K. Ueda, T. Moriya, Contribution of Spin Fluctuations to the Electrical and Thermal Resistivities of Weakly and Nearly Ferromagnetic Metals, Journal of the Physical Society of Japan 39 (1975) 605–615.

[44] A. Rosch, Interplay of Disorder and Spin Fluctuations in the Resistivity near a Quantum Critical Point, Phys. Rev. Lett. 82 (1999) 4280–4283.

[45] R. P. Jena, D. Kumar, A. Lakhani, Scaling analysis of anomalous Hall resistivity in the Co_2TiAl Heusler alloy, Journal of Physics: Condensed Matter 32 (2020) 365703.

[46] Q. Wang, S. Sun, X. Zhang, F. Pang, H. Lei, Anomalous Hall effect in a ferromagnetic Fe_3Sn_2 single crystal with a geometrically frustrated Fe bilayer kagome lattice, Phys. Rev. B 94 (2016) 075135.

[47] J. Yan, X. Luo, G. Lin, F. Chen, J. Gao, Y. Sun, L. Hu, P. Tong, W. Song, Z. Sheng, W. Lu, X. Zhu, Y. Sun, Anomalous Hall effect of the quasi-two-dimensional weak itinerant ferromagnet $Cr_{4.14}Te_8$, EPL (Europhysics Letters) 124 (2019) 67005.

[48] Y. Wang, C. Xian, J. Wang, B. Liu, L. Ling, L. Zhang, L. Cao, Z. Qu, Y. Xiong, Anisotropic anomalous Hall effect in triangular itinerant ferromagnet Fe_3GeTe_2, Phys. Rev. B 96 (2017) 134428.

[49] S. Onoda, N. Sugimoto, N. Nagaosa, Quantum transport theory of anomalous electric, thermoelectric, and thermal Hall effects in ferromagnets, Phys. Rev. B 77 (2008) 165103.

[50] E. Liu, Y. Sun, N. Kumar, L. Muechler, A. Sun, L. Jiao, S.-Y. Yang, D. Liu, A. Liang, Q. Xu, et al., Giant anomalous Hall effect in a ferromagnetic kagome-lattice semimetal, Nature physics 14 (2018) 1125–1131.

[51] W. Zhou, T. Seki, T. Kubota, G. E. W. Bauer, K. Takanashi, Spin-Hall and anisotropic magnetoresistance in ferrimagnetic Co-Gd/Pt layers, Phys. Rev. Materials 2 (2018) 094404.

[52] B.-T. Qi, J.-J. Guo, Y. qing Miao, M. zeng Zhong, B. Li, Z. yan Luo, X. guang Wang, Y. zhuang Nie, Q. lin Xia, G. hua Guo, Abnormal Magnetoresistance Transport Properties of van der Waals Antiferromagnetic $FeNbTe_2$, Frontiers in Physics 10 (2022).

Chapter 5

Magnetic and magnetotransport properties of proposed topological Weyl semimetal $HoSiAl_2$

5.1 Introduction

Rare-earth based intermetallic compounds have garnered significant attention because of their diverse and complex physical properties, such as quantum critical point [1], valence fluctuations [2], non-Fermi liquid behavior [3], heavy fermion behavior [4], charge density wave[5], superconductivity [6], etc . Recently, rare-earth based compounds are fascinating due to their non-trivial topological properties[7–12]. A special interest arises in those materials, which show interplay between topology and magnetism [13]. Topological magnets are especially intriguing due to their tunable phases and electromagnetic responses, which are exciting for both fundamental science and next-generation technological applications [14]. For instance, in magnetic topological Weyl semimetals, the anomalous Hall conductivity value is proportional to net Berry curvature which can be tuned by adjusting the Weyl nodes position in momentum space [15–18]. In addition to the Anomalous Hall Effect (AHE), a distinct form of Hall effect known as the Topological Hall Effect (THE) manifests in noncoplanar spin structures, characterized by the presence of a finite scalar spin chirality [19]. Therefore, exploring the interplay between electronic band topology in momentum space and the topological characteristics of spin texture in real space is a valuable endeavor.

Magnetic Weyl semimetals (MWSMs) with concurrent violations of inversion symmetry and time-reversal symmetries are relatively rare. Recently, there has been increased attention on the RAlX (R: Ce, Pr, Nd; X: Si or Ge) family in research. This family features a noncentrosymmetric crystal structure and the rare earth element R typically possesses an inherent f-electron magnetic moment. In this context, LaAlGe is I-breaking type-II WSM [20, 21] , PrAlGe is T-breaking type-I WSM [22], and CeAlGe is T-breaking

type-II WSM [23]. Different magnetic states such as the magnetic glassy phase, ferromagnetic(FM), antiferromagnetic (AFM), and ferrimagnetic (FMI) arises in these type of systems [24–29]. Recently, GdAlSi, having antiferromagnetic transition at T_N=32K, hosts numerous Weyl points near the Fermi energy[30]. GdAlGe exhibits FM order with Curie temperature (T_c=21K) for tetragonal phase[31] and AFM order with Neel temperature (T_N=34K) for orthorhombic phase [32]. TbAlGe shows two antiferromagnetic transitions at 7K and 39K, respectively and ErAlGe shows AFM transition at 7K[33]. From structural point of view, these group is very interesting. The compound can be divided in two groups based on the size of rare earth elements. Light rare earth based RAlGe (R=La,Ce,Pr,Nd,Sm)which was initially reported in disordered tetragonal α-$ThSi_2$ centrosymmetric crystal structure[34]. Later, it is reported to be an ordered LaPtSi type noncentrosymmetric crystal structure[35]. Heavy rare earth based RAlGe (R= Gd, Tb, Dy, Ho, Er, Tm, Yb, and Lu) crystallizes into an orthorhombic DyAlGe type structure [36]. To date, Ge based RAlGe are well investigated, but investigations on RAlSi (specially R=heavy rare earth) is still lacking. Although, HoAlGe is reported [37], but there are no systematic studies on Ho-Al-Si system. All these exciting phenomena motivated us to further explore Ho-Al-Si systems in context of their structural, magnetic, transport, and electronic band structure properties.

Specially, $R_2Al_3Si_2$(R=Tb,Dy,Ho,Er,Tm) crystallizes in C-centered monoclinic $Y_2Al_3Si_2$-type crystal structure [38, 39]. In particular, Ho-Al-Si system seems to be stabilized in $Ho_2Al_3Si_2$ and $HoAl_2Si$ [40]. Here, we explore the details investigations on the results of our study of $HoSiAl_2$ single crystal. $HoSiAl_2$ crystallizes in monoclinic C12/m1(12) crystal structure. The experimental characterization of $HoSiAl_2$ was complemented by bulk electronic band structure calculations, which revealed the presence of a Weyl nodes.

5.2 Experiment and first principles calculation details

High quality single crystals were grown by the flux growth method. In this method, constituent elements of Ho (99.99%, Alfa Aesar), Si(99.999%, Alfa Aesar), and Al(99.99%, Alfa Aesar) were taken in 1 : 1 : 10 molar ratio and mixed thoroughly in argon atmosphere inside a glove box. The mixture was kept into an alumina crucible and sealed in a quartz ampoule under argon atmosphere. Next, the ampoule was heated in muffle furnace up to 1050°C for 12 hours before slowly cooled down to 750°C at a rate of 3°C/hour. At this temperature, flux was removed by centrifugation. The obtained crystals were in a typical size of 1.5×0.5×0.3 mm^3. Further, a little amount of Al flux deposited on the surface of single crystals was removed by soaking in diluted NaOH solution.

Chemical composition of the as-grown single crystals were examined by energy-dispersive X-ray analysis (EDX) equipped to a scanning electron microscope (SEM) (Quanta 250

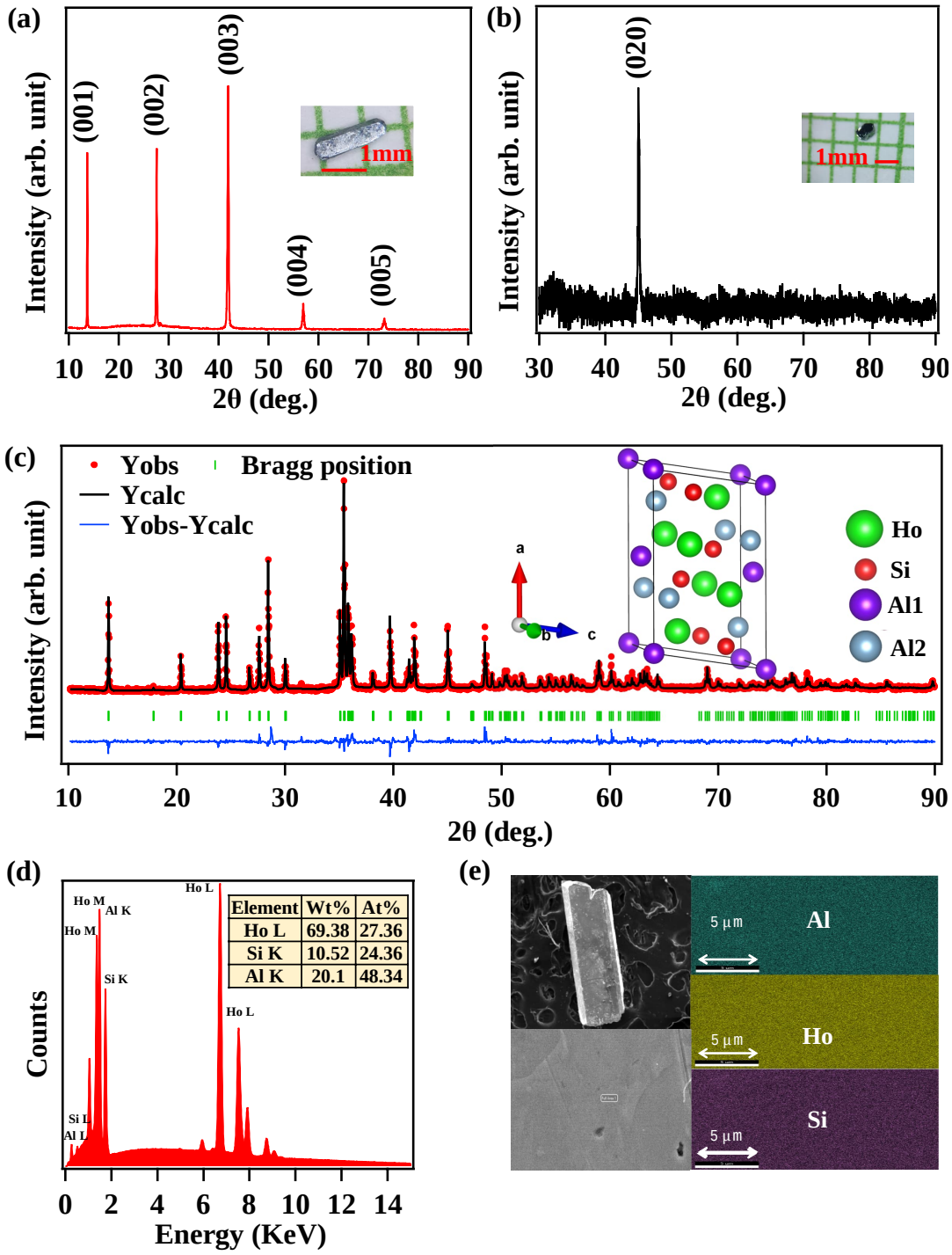

Figure 5.1: (a)Single crystal XRD pattern of $HoSiAl_2$ showing $(00l)$ reflections. Inset shows the optical image of the single crystal of $HoSiAl_2$.(b) Single crystal XRD pattern of $HoSiAl_2$ having $(0l0)$ reflections. Inset shows the optical image of the single crystal at this direction. (c)Experimental (red)and calculated (black) powder XRD data of $HoSiAl_2$. Inset shows the crystal structure of $HoSiAl_2$. (d) EDS spectra of $HoSiAl_2$, accompanied by tabulated elemental ratios. (e) SEM image of a $HoSiAl_2$ single crystal with elemental mapping of Ho, Si, and Al.

FEG) and phase purity checked by X-ray diffraction (XRD) patterns using Cu k_α-radiation (Rigaku SmartLab 9KW). Single-crystal X-ray diffraction (SCXRD) experiments were conducted using a Bruker D8 VENTURE microfocus diffractometer equipped with a PHOTON II detector, utilizing Mo K_α radiation ($\lambda = 0.71073$Å). For the electrical resistivity measurements linear four-probe method was applied. Hall measurements were carried out using the measuring geometry shown schematically in the inset of Fig. 5.4. Electrical transport and Hall measurements were recorded in a Quantum Design physical property measurement system (Quantum Design PPMS) with ETO option using a standard four-probe method, with the a.c. electrical current applied along the plane of sample (ac-plane). The sample temperature was varied between 2 K and 300 K during the transport measurements. In order to eliminate the contact misalignment, the Hall data was anti-symmetrized using this formula $\frac{\rho(H)-\rho(-H)}{2}$.

DC magnetization measurements were performed using PPMS equipped with vibrating sample magnetometer (VSM). Temperature dependence of magnetization in zero-field-cooled (ZFC) and field-cooled (FC) protocols have been carried out under different magnetic fields up to 7T in the temperature range 2-300 K.
In order to comprehend the band structure of $HoSiAl_2$, we employed density-functional theory (DFT) based on the Perdew-Burke-Ernzerhof-type generalized gradient approximation [41], implemented in the QUANTUM ESPRESSO (QE) simulation package [42]. All calculations were conducted with a plane-wave energy cutoff set at 80 Ry. Brillouin zone sampling is performed using a 6× 13 × 8 Monkhorst-Pack k grid, while optimization of the crystal structure is accomplished through the variable-cell relaxation method implemented in QE. To evaluate the ground-state electronic properties, we consider the AFM magnetic structure. The band structure was calculated both with and without the inclusion of spin-orbit coupling (SOC).

5.3 Results and discussions

5.3.1 Crystal Structure

The XRD patterns taken on the $HoSiAl_2$ are shown in Fig. 5.1(a) and Fig. 5.1(b), displaying the (0 0 l) and (0 l 0) Bragg peaks. The (0 l 0) peak parallel to the needle axis of the crystal suggests that the crystal growth axis is along the b-axis. The XRD data confirm that $HoSiAl_2$ crystallizes in monoclinic phase with a space group C12/m1(12). We further performed Rietveld refinement on the powder XRD using the FULLPROF software [43]. The lattice parameters calculated from the Rietveld refinement, a=10.119(2)Å, b=4.024 (9)Å, c=6.575 (15) Å, and β =100.828 $(15)^0$, matched with the previous report [40]. Fig. 5.1(c) shows the powder XRD pattern of crushed single crystals of $HoSiAl_2$ performed at room temperature. Fig. 5.1(d) displays the EDX data, with the atomic and weight percentages of the elements tabulated in the top right inset. From the experimen-

tal data, we obtain Ho:Si:Al is in the ratio of 1.03:0.92:1.84 ($Ho_{1.12}SiAl_{1.98}$), confirm the expected stoichiometry of the crystals investigated. Additionally, elemental mapping for Ho, Si, and Al using EDX is depicted in Fig. 5.1(e), suggesting excellent homogeneity of the studied single crystals.

5.3.2 Magnetic properties

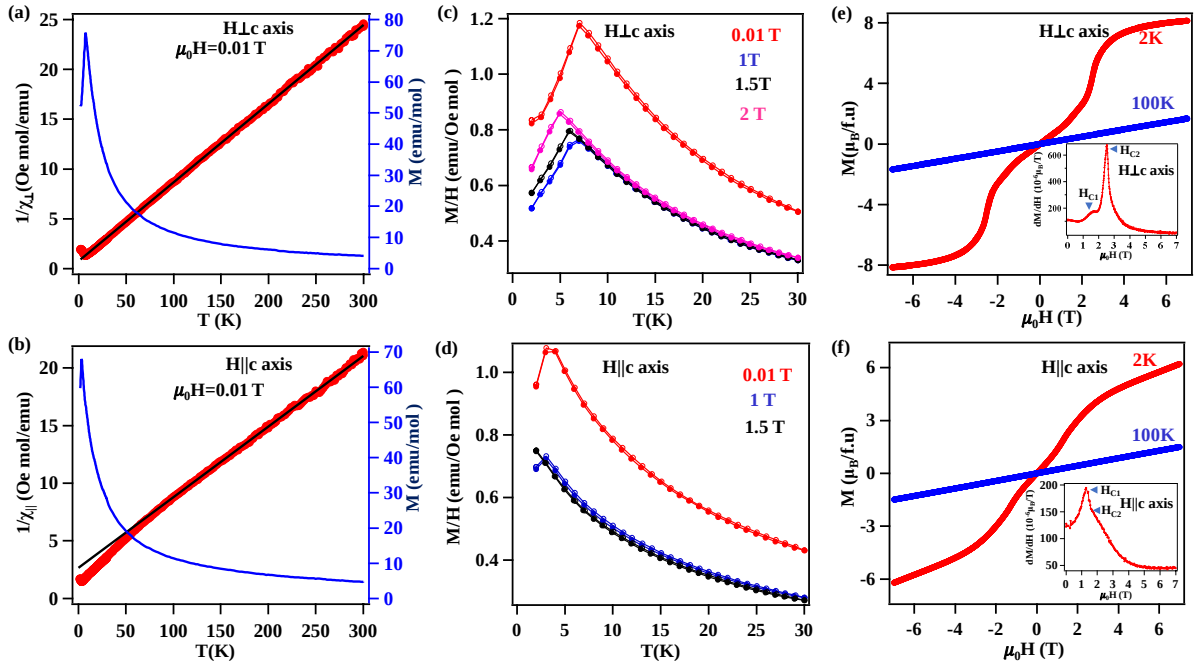

Figure 5.2: Magnetic propertis of $HoSiAl_2$: The inverse magnetic susceptibility (left axis) and magnetization (right axis) were performed with respect to the temperature in a magnetic field of 0.01T along perpendicular to the c axis and parallel to the c axis shown in (a) and (b), respectively. Panels (c) and (d) shows M/H as a function of temperature, recorded in FC (filled circles) and ZFC (open circles)mode in different magnetic fields along c axis and perpendicular to c axis. Panels (e) and (f) displays field dependence of magnetization along perpendicular to the c axis and parallel to the c axis at 2K and 100K.

The temperature dependence of inverse magnetic susceptibilty $\chi_{\parallel}$(T) and $\chi_{\perp}$(T) were performed on $HoSiAl_2$ single crystal sample in a magnetic field of μ_0H=0.01T for H|| c and H⊥ c axis, respectively. The change in susceptibility as a function of temperature from 2 to 300K was demonstrated in Fig. 5.2(a) and Fig. 5.2(b), respectively. The inverse susceptibility can be fitted by the Curie-Weiss law, ($\chi(T) = \frac{C}{T-\theta}$); where C and θ are the Curie constant and Curie-Weiss temperature, respectively. From the Curie-Weiss fitting, we obtain negative Curie constant -9.77K for H⊥ c axis and -43.13K for H|| c. The negetive Curie constant imply the AFM exchange interaction between Ho moments. The effective magnetic moment estimated from the fitting are 10.06 μ_B/f.u for H⊥ c and 11.45μ_B/f.u for H|| c, matches well with the theoretical value of 10.60 for Ho^{3+} ions.

Fig. 5.2(c) and Fig. 5.2(d) display the DC magnetization (M) as a function of temperature in ZFC and FC modes in different magnetic fields for H⊥ c and H‖ c axis. A clear peak around T_N=7K along H⊥ c and around T_N=3K along H‖ c axis, indicates clear AFM phase transition. In Fig. 5.2(e), the isothermal magnetization (M) versus magnetic field (H) data recorded at 2 K is presented. The M(H) curve exhibits step-like behavior, thus showing a field-induced metamagnetic transition from AFM ground state to FM state. There are two metamagnetic transitions occurring at approximately H_{c1}=1.6 and H_{c2}=2.5 T, identified by the maxima in the $\frac{dM}{dH}$ curve, as depicted in Fig. 5.2(e)inset. For H‖ c, the magnetization is far from saturation. There is no indication of saturation, even under a magnetic field of 7T. This suggests that the c axis represents the hard axis, while the perpendicular to c axis serves as the easy axis of magnetization. In the case of H‖ c, $\frac{dM}{dH}$ curve at T = 2 K display small and broad peak at H_c=1.2T, as well as a peak at 2.1 T, displayed in the inset of Fig. 5.2(f). This peak might suggest the presence of weak metamagnetic transition. These peaks might suggest the presence of weak metamagnetic transition. At 100 K, M(H) curves for both directions exhibit linear behavior and small magnetization values, consistent with the paramagnetic (PM) characteristics.

5.3.3 Magnetocaloric Effect

In order to study the magnetocaloric effect (MCE) of $HoSiAl_2$ single crystal, we performed the magnetization isotherms under various magentic fields. Figs. 5.3(a) and 5.3(b) show the magnetization isotherms for the $H \perp c$ and $H \parallel c$, respectively. The magnetization usually decreases with increasing temperature, as observed in Figs. 5.3(a) and 5.3(b). The $M(H)$ curve becomes completely linear only above 40 K, implying that there is a short-range magnetic interactions even above T_N. To study the magnetocaloric effect, the magnetic-entropy change ΔS_M was derived from the field and temperature dependence of magnetization using the Maxwell relation, $\Delta S_M(T,H)=S_M(T,H)-S_M(T,0)=\int_0^H (\frac{\partial M}{\partial T})_H \, dH$. Figs. 5.3(c) and 5.3(d) demonstrate the magnetic entropy change with the temperature of $HoSiAl_2$ single crystal. It can be seen that ΔS_M shows a broad hump around T_N with negative values. The peak value increases with increasing field. The maximum magnetic-entropy change for $H \perp c$ and $H \parallel c$ are -27.427J/Kg K and -17.528J/Kg K, respectively. $HoSiAl_2$ has large ΔS_M compared to other Ho-based MCE materials $HoAl_2Ge_2$ [44], $HoMnO_3$ [45, 46], $HoNiGe_3$ [47], and other rare-earth based materials $TbFeO_3$ [48], $DyMnO_3$ [49],$TbMn_2O_5$ [50],$ErNi_3Al_9$ [51],$ErMnO_3$ [52]. But has much smaller ΔS_M than that of Gd-based materials such as $Gd_5Si_2Ge_2$ [53],$NaGdS_2$ [54], $Gd(OH)F_2$ [55]. Further, the maximum entropy change of the $HoSiAl_2$ with $H \perp c$ is much greater than $H \parallel c$. This consistent with the fact that magnetic moments tend to be more oriented along the *b*-axis. Generally, conventional MCE, i.e, negetive MCE, would be expected for ordinary FM and PM samples [53]. In our case, a negative MCE is obtained above T_N for both axis which decreases with increasing temperature. However,

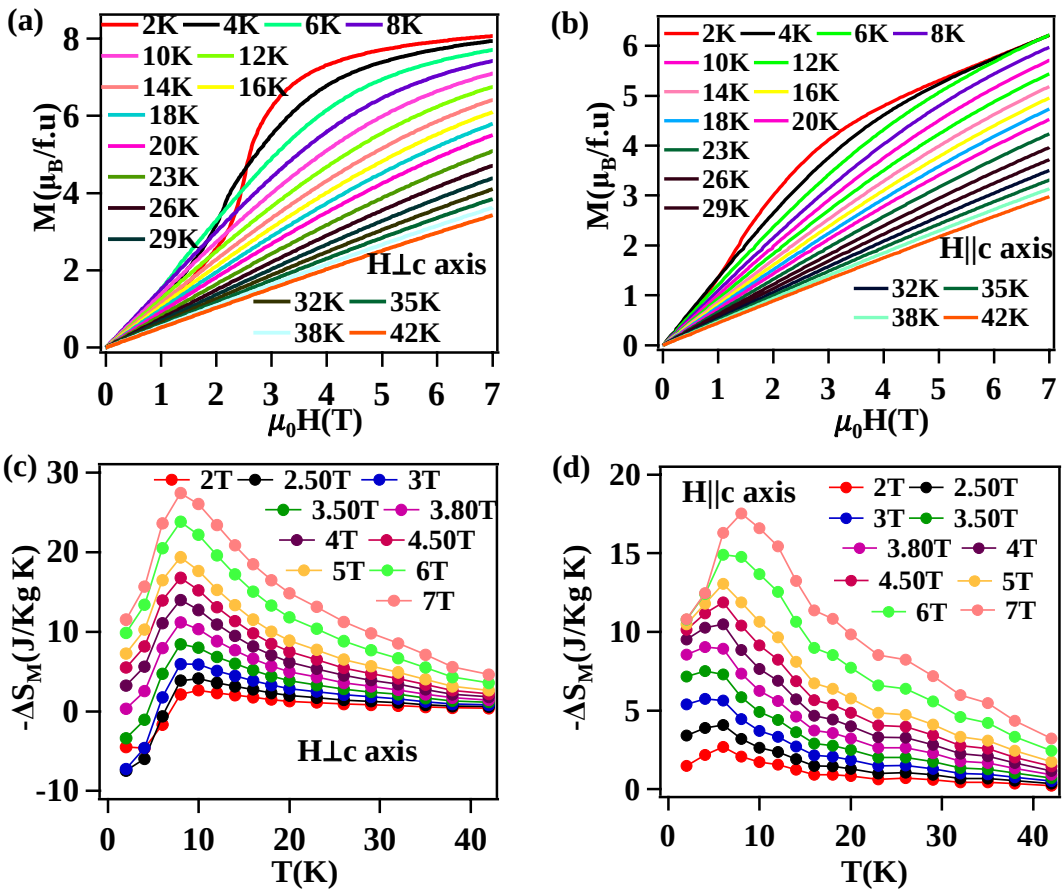

Figure 5.3: Magnetic isotherm curves of $HoSiAl_2$ (a) along perpendicular to the c axis, (b) parallel to the c axis. (c) Magnetic entropy change versus temperature for the H⊥ c and H‖ c axis.

for $H \perp c$, we find MCE with positive ΔS_M below T_N Fig. 5.3(c). According to the M(H), the AFM interaction is dominant below H_c, and turns to be FM behavior above the H_c. So, the value of the positive ΔS_M increases with increasing H and reaches the maximum value at H=H_c (around 2.5T).With further increasing H , ΔS_M decreases and becomes completely negative at around 4T. So, the origin of the positive ΔS_M could be the metamagnetic transition and may be driven by the competition between FM and AFM exchange interactions [56–58]. So,the materials with negative MCE can be used to cool the system by applying the external magnetic field adiabatically, rather than removing the field as in case of regular FM system [56, 59].

5.3.4 Magnetotransport

The temperature dependence of the electrical resistivity (ρ_{xx}) of single crystalline $HoSiAl_2$ in the absence of a magnetic field was shown in Fig. 5.4(a). The resistivity decreases with decreasing temperature, showing metallic nature. This temperature dependence resistivity behavior is similar to those reported for $HoNiGe_3$ [47], SmAlSi [60], TbPtBi [61], GdAgGe [62] .The value of residual resistivity ratio (RRR), defined as ρ_{300}/ρ_2 is 5.00, rela-

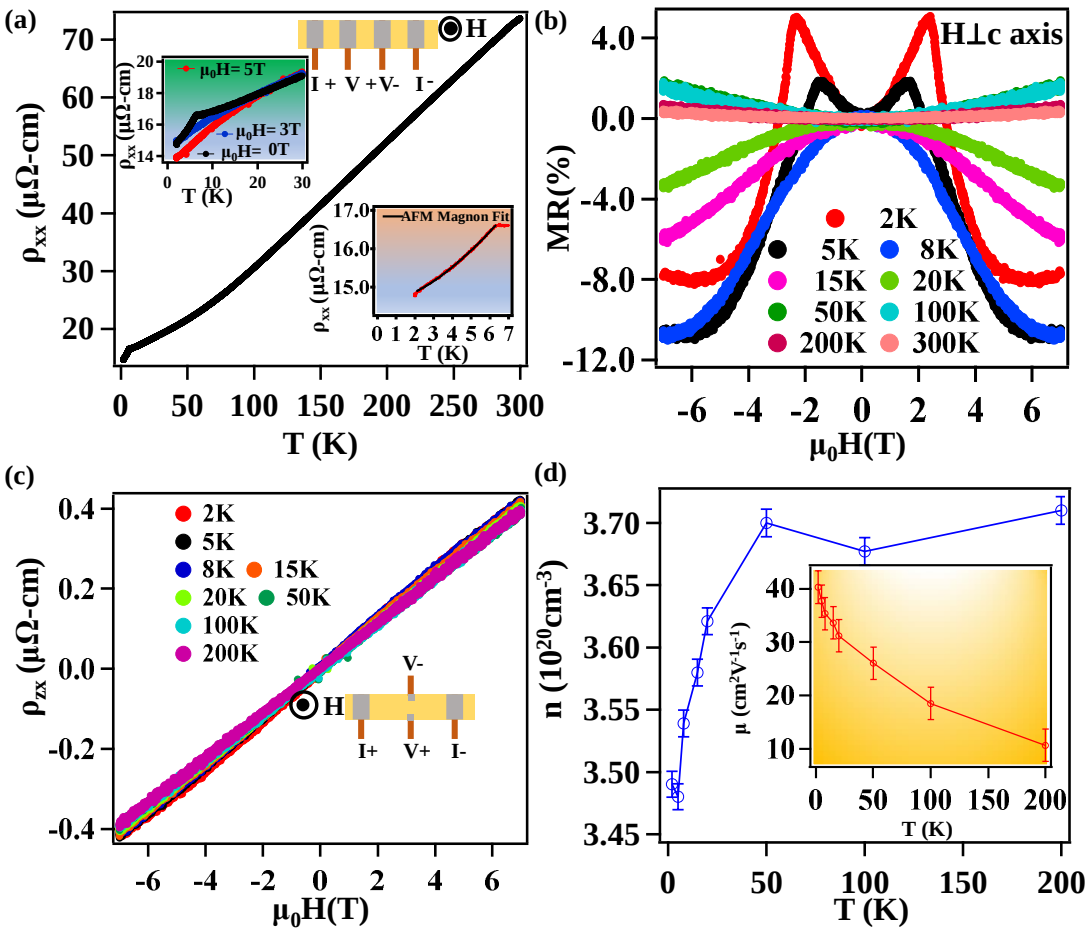

Figure 5.4: (a) Zero-field electrical resistivity as a function of temperature in $HoSiAl_2$ single crystal. Inset displays the resistivity for different applied magnetic field strengths and AFM magnon fitting in the zero-field resistivity data below T_N. (b) Transverse magnetoresistance isotherms of $HoSiAl_2$, measured from 2-300K. (c) Hall resistivity as a function of magnetic field for $HoSiAl_2$ at different temperatures. Inset displays schematic of four probe connections for Hall measurement. (d) Temperature dependence of the charge carrier density n. The inset shows the temperature-dependent mobility(μ).

tively larger than R-Al-X based ternary compounds [63–66], but comaprable to SmAlSi [60]. Below T_N, the resistivity decreases more sharply, shown in the inset of Fig. 5.4(a). This feature can be attributed as reduction of spin-disorder scattering. Application of the external magnetic field smear out this behaviour, displayed in the inset of Fig. 5.4(a). Normal T^2 law is not fitted in the AFM region. In order to know the proper magnetic ground state of $HoSiAl_2$ single crystal, $\rho(T)$ below T_N is fitted with AFM magnon relation [67]: $\rho(T) = \rho_0 + AT^2 + B\Delta^5 e^{-\frac{\Delta}{T}}[1/5(\frac{T}{\Delta})^5 + (\frac{T}{\Delta})^4 + 5/3(\frac{T}{\Delta})^3]$ where ρ_0 is the zero-temperature electrical resistivity, A is the constant for the Fermi liquid term, B is the constant for the electron-magnon scattering term, and Δ is the magnon gap energy. We find the parameters associated with this fit are $\rho_0 = 14.45\mu\Omega - cm$, A=$0.0166\Omega - cmK^{-2}$, A=5.47x$10^{-}4\ \Omega - cmK^{-5}$, Δ=3.50K, as displayed in Fig. 5.4(a), implying that $HoSiAl_2$ has AFM ground state as obtained from magnetic susceptibility data. Usually, collinear

AFM state has gapless magnon characteristic [68]. So, the gapped magnon behavior of $\rho(T)$ implies that $HoSiAl_2$ has non collinear AFM spin structure below T_N. Similar kind of magnon gap like feature at low temperature was observed in the literature for $NdCoSi_3$ [69],TbB_4 [70], and SmB_4 [71] compounds. The transverse magnetoresistance (MR), defined as $\frac{\Delta\rho}{\rho} = \frac{\rho(H)-\rho(0)}{\rho(0)}$, is shown in Fig. 5.4(b). Initially, MR obtained at 2K rises with the increase of applied magnetic field and attains a peak value of $\approx 5\%$ around 2.5T. The peak in MR data is associated with the metamagnetic transition as observed in the magnetization data Fig. 5.2(e). With further increase of magnetic fields, the MR value decreases and turns to be negetive. The positive MR is coming due to the suppression of AFM order and the increment of the spin scattering of the conduction electrons by the applied magnetic field. But, after 2.5T, MR decreases due to the FM behavior that tends to suppress the spin scattering. Similar phenomena is observed in $Na_{0.85}CoO_2$ [72], layered ruthenates [73], EuAuAs [74], $EuMg_2Bi_2$ [75], $EuBiTe_3$ [76].

In order to know the charge carrier concentration and mobility, we measured the magnetic field dependent Hall resistivity from 2-200K, shown in Fig. 5.4(c). The positive and linear ρ_{xz} implies that majority charge carriers are holes. The slope of the linear fit provides the Hall coefficient R_H, utilized to compute hole carrier concentration (n) and Hall mobility (μ) by using these formulas $n=1/(eR_H)$ and $\mu=R_H/\rho_{xx}(H=0)$, respectively. The estimated value of n and μ is $3.49\text{x}10^{20}\text{cm}^{-3}$ and 40.28 $\text{cm}^2\text{V}^{-1}\text{S}^{-1}$. Although carrier density is higher than typical Dirac/Weyl semimetals ($n\approx10^{17}$-10^{18}) [77, 78], but is same order of magnitude reported in several nodal-line semimetals [79–82]. In Fig. 5.4(d), we have shown that carrier concentration and Hall mobility both are almost temperature independent. We do not notice the signature of unconventional Hall effect down to 2K. This could be due to the fact that topological non-trivial band crossing is not precisely positioned at the Fermi level. So, we did not obtain the contribution of topological non-trivial fermions in our transport measurement, which is probably hindered by conventional charge carriers.

5.3.5 Electronic structure

By computing the total energy, AFM is more stable than FM state in $HoSiAl_2$, alighning with the AFM state observed in the magnetization data. Furthermore, total density of states (DOS) and projected density of states (PDOS) were computed for AFM case. This was done to elucidate the behavior of the Ho, Al, and Si elements, and the corresponding outcomes are presented in and Fig. 5.5(a) and Fig. 5.5(b). The valence-band region and conduction band region both are dominated by Ho in both spin-channels. Additionally, the observation of a density of states at the Fermi level in $HoSiAl_2$ confirms its metallic nature.

In order to comprehend the topological characteristics of the compound, the band dispersions are computed using a plane wave based pseudo potential method [83], both

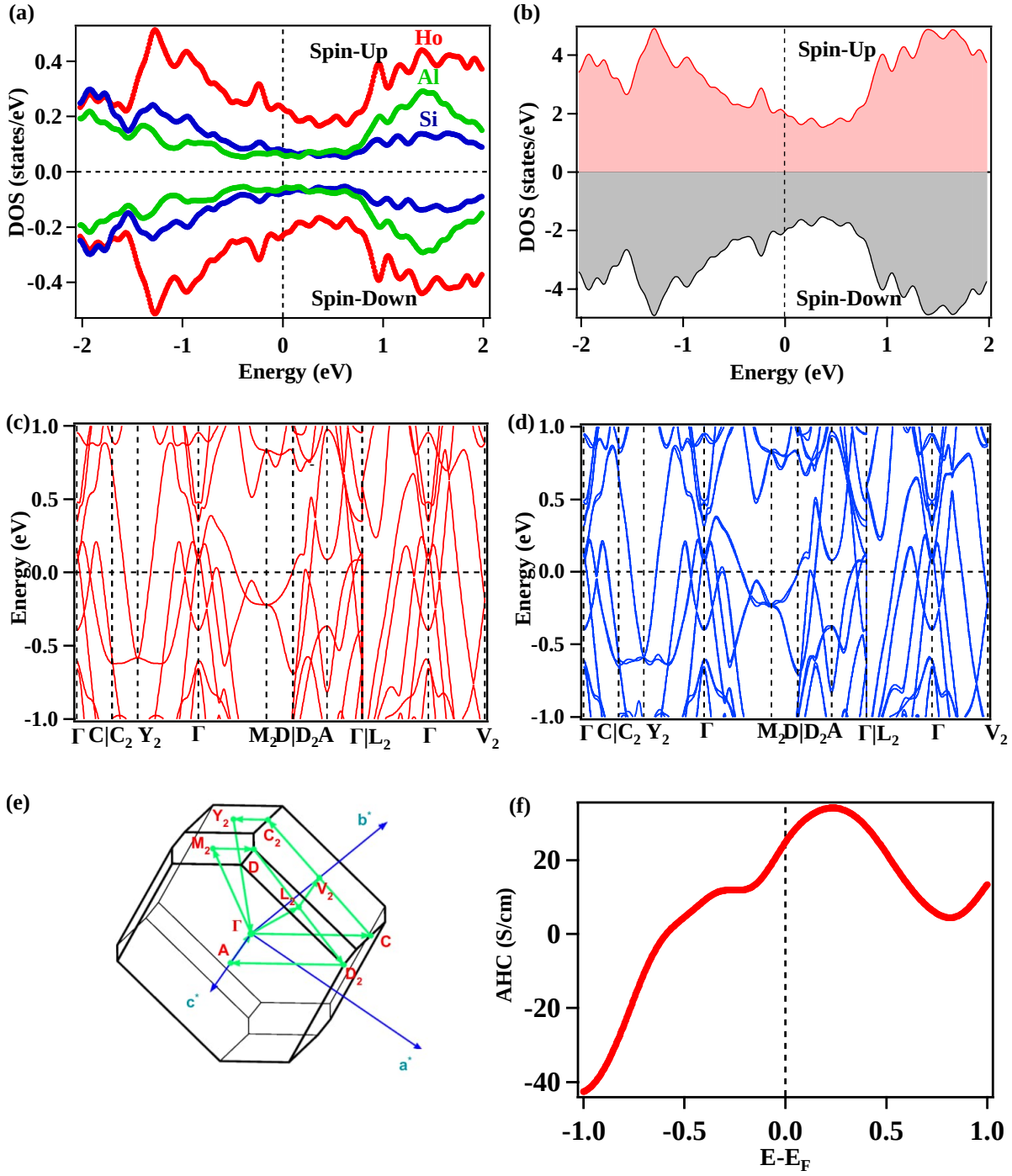

Figure 5.5: (a) Projected density of states and (b) total density of states of $HoSiAl_2$.(c) Band structure without SOC and (d) with SOC of $HoSiAl_2$. (e) Brillouin zone of $HoSiAl_2$. (f) AHC of $HoSiAl_2$.

in the absence and presence of spin-orbit coupling (SOC). Intriguingly, the conduction and valence bands cross each other in a linear manner along the K_y=0 plane, displyed in Fig. 5.5(c). In the presence of SOC, spin is not a good quantum number, shown in Fig. 5.5(d). Symmetric points are characterized within the Brillouin zone of the monoclinic primitive unit cell, shown in Fig. 5.5(e).

Table 5.1: The Weyl point positions, Chern numbers, and energy relative to E_F of $HoSiAl_2$.

Weyl point	k_x	k_y	k_z	Chern number	E-E_F (eV)
W_1	-0.030	-0.003	0.069	1	-0.091
W_1	-0.028	0.001	0.069	-1	-0.085
W_2	-0.089	-0.060	-0.124	1	-0.080
W_2	-0.087	0.061	-0.121	-1	-0.072

Exploring Weyl Nodes in the AFM [010] Ground State reveals the presence of multiple Weyl nodes. A comprehensive exploration of band crossings throughout the entire Brillouin Zone (BZ) reveals 2 pairs of Weyl points with a Chern number of ± 1 in the primitive BZ, located approximately $\approx$ 50 to 100 meV below the Fermi level (E_F).

Also, we have calculated the anomalous Hall conductivity of the sample. The anomalous Hall conductivity (AHC) is directly proportional to the Berry curvature, a geometric characteristic of energy bands. The intrinsic anomalous Hall conductivity (AHC) can be assessed using the linear response theory within the Kubo formalism [84], and the AHC in the xz plane can be represented as follows: $\sigma_{xz} = -\frac{e^2}{\hbar} \int \frac{d^3k}{(2\pi)^3} \sum_n \Omega_n^y(k) f_n(k)$

where $\Omega_n^z(k)$ is the Berry curvature, $f_n(k)$ is the Fermi-Dirac distribution function, and n is the index of the occupied bands.

We have calculated the anomalous Hall conductivity (AHC) using this formula $\sigma_{xz} = \frac{\rho_{zx}}{{\rho_{zx}}^2 + {\rho_{xx}}^2}$. Notably, the maximal value of Hall conductivity 2150$(\Omega\text{-cm})^{-1}$, is achieved at 2 K and 7 T.This exceptionally high Hall conductivity does not originate from the anomalous Hall effect but rather from the elevated longitudinal conductivity, which is derived from the low residual resistivity $\rho_0 = 13.9 \mu\Omega$-cm. This phenomenon has been observed in other materials as well [85]. This phenomena is consistent with our theoretical calculations, shown in Fig. 5.5(f).

5.4 Conclusions

In summary, we have explored the physical properties of $HoSiAl_2$ single crystals by measuring the magnetic susceptibility, magnetometric effect, magnetoresistance, and Hall effect. We find that $HoSiAl_2$ crystallizes into monoclinic phase with a space group of $C12/m1(12)$. The magnetic susceptibility measurements displayed that $HoSiAl_2$ has an AFM transitions at around $T_N = 7$ K along $H \perp c$ and at around $T_N = 3$ K along $H \parallel c$. In the ordered state, M(H) curve displays step-like behavior, indicating a field-induced metamagnetic transition from the AFM ground state to the FM state. The derivative of magnetization with respect to magnetic field, dM/dH, in the $H \perp c$ direction reveals a couple of spin-flop type metamagnetic transitions. For $H \parallel c$, the magnetization is far from saturation even at 7 T. We obtained ΔS_M=-27.427J/Kg K for $H \parallel c$ and -17.528J/Kg K for $H \perp c$ axis. We have got the maximum value of positive ΔS_M at

$H = H_c$ (around 2.5 T), matched with our magnetization data. Below T_N, the transverse magnetoresistance exhibits a peak, suggesting a metamagnetic transition, and at high magnetic fields, the magnetoresistance value decreases and becomes negative. For $T < T_N$, the resistivity data is fitted by AFM magnon relation. The field dependent Hall measurements suggest dominating hole charge carriers. By employing first-principles calculations, we notice that $HoSiAl_2$ exhibits an antiferromagnetic Weyl semimetallic ground state.

References

[1] Liu, Changjiang and Humbert, Vincent FC and Bretz-Sullivan, Terence M and Wang, Gensheng and Hong, Deshun and Wrobel, Friederike and Zhang, Jianjie and Hoffman, Jason D and Pearson, John E and Jiang, J Samuel and others, Observation of an antiferromagnetic quantum critical point in high-purity $LaNiO_3$, Nature communications 11 (2020) 1402.

[2] M. A. Ahmida, M. K. Forthaus, C. Geibel, Z. Hossain, G. R. Hearne, J. Kaštil, J. Prchal, V. Sechovský, M. M. Abd-Elmeguid, Charge fluctuations across the pressure-induced quantum phase transition in $EuCu_2(Ge_{1-x}Si_x)_2$, Phys. Rev. B 101 (2020) 205127.

[3] G. M. Schmiedeshoff, E. D. Mun, A. W. Lounsbury, S. J. Tracy, E. C. Palm, S. T. Hannahs, J.-H. Park, T. P. Murphy, S. L. Bud'ko, P. C. Canfield, Multiple regions of quantum criticality in YbAgGe, Phys. Rev. B 83 (2011) 180408.

[4] C. M. Varma, Phenomenological aspects of heavy fermions, Phys. Rev. Lett. 55 (1985) 2723–2726.

[5] E. DiMasi, M. C. Aronson, J. F. Mansfield, B. Foran, S. Lee, Chemical pressure and charge-density waves in rare-earth tritellurides, Phys. Rev. B 52 (1995) 14516–14525.

[6] U. Paramanik, P. Paulose, S. Ramakrishnan, A. Nigam, C. Geibel, Z. Hossain, Magnetic and superconducting properties of Ir-doped $EuFe_2As_2$, Superconductor Science and Technology 27 (2014) 075012.

[7] R. Singha, A. Pariari, B. Satpati, P. Mandal, Magnetotransport properties and evidence of a topological insulating state in LaSbTe, Phys. Rev. B 96 (2017) 245138.

[8] L. M. Schoop, A. Topp, J. Lippmann, F. Orlandi, L. Müchler, M. G. Vergniory, Y. Sun, A. W. Rost, V. Duppel, M. Krivenkov, S. Sheoran, P. Manuel, A. Varykhalov, B. Yan, R. K. Kremer, C. R. Ast, B. V. Lotsch, Tunable weyl and dirac states in the nonsymmorphic compound CeSbTe, Science Advances 4 (2018) eaar2317.

[9] K. Pandey, R. Basnet, A. Wegner, G. Acharya, M. R. U. Nabi, J. Liu, J. Wang, Y. K. Takahashi, B. Da, J. Hu, Electronic and magnetic properties of the topological semimetal candidate NdSbTe, Phys. Rev. B 101 (2020) 235161.

[10] L. Y. Cao, M. Yang, L. Wang, Y. Li, B. X. Gao, L. Wang, J. L. Liu, A. F. Fang, Y. G. Shi, R. Y. Chen, Optical study of the topological materials lnSbTe (ln = La, Ce, Sm, Gd), Phys. Rev. B 106 (2022) 245145.

[11] S. Regmi, G. Dhakal, F. C. Kabeer, N. Harrison, F. Kabir, A. P. Sakhya, K. Gofryk, D. Kaczorowski, P. M. Oppeneer, M. Neupane, Observation of multiple nodal lines in SmSbTe, Phys. Rev. Mater. 6 (2022) L031201.

[12] J. L. Liu, R. Liu, M. Yang, L. Y. Cao, B. X. Gao, L. Wang, A. F. Fang, Y. G. Shi, Z. P. Yin, R. Y. Chen, Revealing a charge-density-wave gap in the predicted weak topological insulator HoSbTe, Phys. Rev. B 105 (2022) 075111.

[13] A. Laha, R. Singha, S. Mardanya, B. Singh, A. Agarwal, P. Mandal, Z. Hossain, Topological Hall effect in the antiferromagnetic dirac semimetal EuAgAs, Phys. Rev. B 103 (2021) L241112.

[14] Y. Liu, C. Petrovic, Critical behavior of the quasi-two-dimensional weak itinerant ferromagnet trigonal chromium telluride $Cr_{0.62}Te$, Phys Rev B 96 (2017) 134410.

[15] T. Suzuki, R. Chisnell, A. Devarakonda, Y.-T. Liu, W. Feng, D. Xiao, J. W. Lynn, J. Checkelsky, Large anomalous Hall effect in a half-heusler antiferromagnet, Nature Physics 12 (2016) 1119–1123.

[16] E. Liu, Y. Sun, N. Kumar, L. Muechler, A. Sun, L. Jiao, S.-Y. Yang, D. Liu, A. Liang, Q. Xu, et al., Giant anomalous Hall effect in a ferromagnetic kagome-lattice semimetal, Nature physics 14 (2018) 1125–1131.

[17] Q. Wang, Y. Xu, R. Lou, Z. Liu, M. Li, Y. Huang, D. Shen, H. Weng, S. Wang, H. Lei, Large intrinsic anomalous Hall effect in half-metallic ferromagnet $Co_3Sn_2S_2$ with magnetic weyl fermions, Nature communications 9 (2018) 1–8.

[18] T. Liang, J. Lin, Q. Gibson, S. Kushwaha, M. Liu, W. Wang, H. Xiong, J. A. Sobota, M. Hashimoto, P. S. Kirchmann, et al., Anomalous Hall effect in $ZrTe_5$, Nature Physics 14 (2018) 451–455.

[19] P. Puphal, V. Pomjakushin, N. Kanazawa, V. Ukleev, D. J. Gawryluk, J. Ma, M. Naamneh, N. C. Plumb, L. Keller, R. Cubitt, E. Pomjakushina, J. S. White, Topological magnetic phase in the candidate weyl semimetal CeAlGe, Phys. Rev. Lett. 124 (2020) 017202.

[20] S.-Y. Xu, N. Alidoust, G. Chang, H. Lu, B. Singh, I. Belopolski, D. S. Sanchez, X. Zhang, G. Bian, H. Zheng, M.-A. Husanu, Y. Bian, S.-M. Huang, C.-H. Hsu, T.-R. Chang, H.-T. Jeng, A. Bansil, T. Neupert, V. N. Strocov, H. Lin, S. Jia, M. Z. Hasan, Discovery of lorentz-violating type ii weyl fermions in LaAlGe, Science Advances 3 (2017) e1603266.

[21] T. Ng, Y. Luo, J. Yuan, Y. Wu, H. Yang, L. Shen, Origin and enhancement of the spin Hall angle in the weyl semimetals LaAlSi and LaAlGe, Phys. Rev. B 104 (2021) 014412.

[22] B. Meng, H. Wu, Y. Qiu, C. Wang, Y. Liu, Z. Xia, S. Yuan, H. Chang, Z. Tian, Large anomalous Hall effect in ferromagnetic Weyl semimetal candidate PrAlGe, APL Materials 7 (2019) 051110.

[23] H. Hodovanets, C. J. Eckberg, P. Y. Zavalij, H. Kim, W.-C. Lin, M. Zic, D. J. Campbell, J. S. Higgins, J. Paglione, Single-crystal investigation of the proposed type-II weyl semimetal CeAlGe, Phys. Rev. B 98 (2018) 245132.

[24] T. Wang, Y. Guo, C. Wang, S. Yang, Correlation between non-centrosymmetic structure and magnetic properties in Weyl semimetalNdAlGe, Solid State Communications 321 (2020) 114041.

[25] M. Lyu, J. Xiang, Z. Mi, H. Zhao, Z. Wang, E. Liu, G. Chen, Z. Ren, G. Li, P. Sun, Nonsaturating magnetoresistance, anomalous Hall effect, and magnetic quantum oscillations in the ferromagnetic semimetal PrAlSi, Phys. Rev. B 102 (2020) 085143.

[26] P. Puphal, S. Krebber, E. Suard, R. Cubitt, C. Wang, T. Shang, V. Ukleev, J. S. White, E. Pomjakushina, Development of magnetism in the solid solution of Ce $_{1-x}$Pr $_{x}$AlGe: From magnetic topology to spin glass, Physical Review B 101 (2020) 214416.

[27] H. Hodovanets, C. J. Eckberg, P. Y. Zavalij, H. Kim, W.-C. Lin, M. Zic, D. J. Campbell, J. S. Higgins, J. Paglione, Single-crystal investigation of the proposed type-II Weyl semimetal CeAlGe, Phys. Rev. B 98 (2018) 245132.

[28] D. Destraz, L. Das, S. S. Tsirkin, Y. Xu, T. Neupert, J. Chang, A. Schilling, A. G. Grushin, J. Kohlbrecher, L. Keller, et al., Magnetism and anomalous transport in the weyl semimetal PrAlGe: possible route to axial gauge fields, npj Quantum Materials 5 (2020) 5.

[29] C. Li, J. Zhang, Y. Wang, H. Liu, Q. Guo, E. Rienks, W. Chen, F. Bertran, H. Yang, D. Phuyal, et al., Emergence of Weyl fermions by ferrimagnetism in a noncentrosymmetric magnetic Weyl semimetal, Nature Communications 14 (2023) 7185.

[30] A. Laha, A. K. Kundu, N. Aryal, E. S. Bozin, J. Yao, S. Paone, A. Rajapitamahuni, E. Vescovo, T. Valla, M. Abeykoon, R. Jing, W. Yin, A. N. Pasupathy, M. Liu, Q. Li, Electronic structure and magnetic and transport properties of antiferromagnetic Weyl semimetal GdAlSi, Phys. Rev. B 109 (2024) 035120.

[31] C. Wang, Y.-Q. Guo, T. Wang, S.-W. Yang, Crystal structure and electromagnetic responses of tetragonal GdAlGe, Chinese Physics B 29 (2020) 127502.

[32] C. Wang, Y. Guo, T. Wang, Magnetic and transport properties of orthorhombic rare-earth aluminum germanide GdAlGe, Journal of Magnetism and Magnetic Materials 526 (2021) 167739.

[33] C. Wang, Y. Guo, T. Wang, Correlation between slanted magnetic structure and electromagnetic responses in the RAlGe (r= Tb and Er) system, The Journal of Physical Chemistry C 125 (2021) 21764–21770.

[34] S. Pukas, Y. Lutsyshyn, M. Manyako, E. Gladyshevskii, Crystal structures of the RAlSi and RAlGe compounds, Journal of alloys and compounds 367 (2004) 162–166.

[35] S. Ramakrishnan, K. Ghosh, A. D. Chinchure, V. R. Marathe, G. Chandra, Magnetism and superconductivity in RPtSi (R=La, Ce, Nd, and Sm), Phys. Rev. B 52 (1995) 6784–6795.

[36] J. Zhao, E. Parthé, Structure of YAlGe and isotypic rare-earth–aluminium germanides, Acta Crystallographica Section C: Crystal Structure Communications 46 (1990) 2276–2279.

[37] C. Wang, Y. Guo, T. Wang, Dynamic evolution from positive to negative magnetoresistance of RAlGe (R= Dy, Ho) with disordered orthorhombic structure, Journal of Alloys and Compounds 902 (2022) 163623.

[38] A. L. Sharma, S. Bobev, J. Sarrao, Oscillations in magnetocaloric effect and magnetic properties of $RE_2Al_3Si_2$ (for RE= Dy, Ho and Er) and REAlSi (for RE= Ce and Pr), Journal of magnetism and magnetic materials 312 (2007) 400–404.

[39] S. Bobev, P. H. Tobash, V. Fritsch, J. D. Thompson, M. F. Hundley, J. L. Sarrao, Z. Fisk, Ternary rare-earth alumo-silicides—single-crystal growth from Al flux, structural and physical properties, Journal of Solid State Chemistry 178 (2005) 2091–2103.

[40] Chen, Xian-Zhong and Sieve, Bradley and Henning, Robert and Schultz, Arthur J and Brazis, Paul and Kannewurf, Carl R and Cowen, Jerry A and Crosby, Richard and Kanatzidis, Mercouri G, $Ln_2Al_3Si_2$ (Ln= Ho, Er, Tm): New Silicides from Molten Aluminum—Determination of the Al/Si Distribution with Neutron Crystallography and Metamagnetic Transitions, Angewandte Chemie International Edition 38 (1999) 693–696.

[41] J. P. Perdew, K. Burke, M. Ernzerhof, Generalized gradient approximation made simple, Phys. Rev. Lett. 77 (1996) 3865–3868.

[42] P. Giannozzi, S. Baroni, N. Bonini, M. Calandra, R. Car, C. Cavazzoni, D. Ceresoli, G. L. Chiarotti, M. Cococcioni, I. Dabo, et al., Quantum espresso: a modular and open-source software project for quantum simulations of materials, Journal of physics: Condensed matter 21 (2009) 395502.

[43] J. Rodríguez-Carvajal, Recent advances in magnetic structure determination by neutron powder diffraction, Physica B: Condensed Matter 192 (1993) 55–69.

[44] F. Gao, J. Sheng, W. Ren, Q. Zhang, X. Luo, J. Qi, M. Cong, B. Li, L. Wu, Z. Zhang, Incommensurate spin density wave and magnetocaloric effect in the metallic triangular lattice $HoAl_2Ge_2$, Phys. Rev. B 106 (2022) 134426.

[45] A. Midya, S. N. Das, P. Mandal, S. Pandya, V. Ganesan, Anisotropic magnetic properties and giant magnetocaloric effect in antiferromagnetic $RMnO_3$ crystals (R = Dy, Tb, Ho, and Yb), Phys. Rev. B 84 (2011) 235127.

[46] W. Wang, Y. Li, L. Li, Q. Li, D. Wang, J. Zhu, J. Li, M. Zeng, The observed topological vortex domains and the rotating magnetocaloric effect in the hexagonal $RMnO_3$ (R= Ho, Er, and Yb) crystals, Journal of Physics: Condensed Matter 33 (2020) 015802.

[47] X. Zhao, X. Zheng, J. Qi, X. Luo, S. Ma, S. U. Rehman, W. Ren, C. Chen, Z. Zhong, Anisotropic magnetocaloric effect and magnetoresistance in antiferromagnetic $HoNiGe_3$ single crystal, Intermetallics 138 (2021) 107307.

[48] Y.-J. Ke, X.-Q. Zhang, Y. Ma, Z.-H. Cheng, Anisotropic magnetic entropy change in R FeO_3 single crystals (R= Tb, Tm, or Y), Scientific Reports 6 (2016) 19775.

[49] M. Balli, S. Jandl, P. Fournier, S. Mansouri, A. Mukhin, Y. V. Ivanov, A. Balbashov, On the magnetocaloric effect in the multiferroic hexagonal $DyMnO_3$ single crystals, Journal of Magnetism and Magnetic Materials 374 (2015) 252–257.

[50] M. Balli, S. Jandl, P. Fournier, D. Dimitrov, Giant rotating magnetocaloric effect at low magnetic fields in multiferroic $TbMn_2O_5$ single crystals, Applied Physics Letters 108 (2016) 102401.

[51] X. Zhao, X. Zheng, X. Luo, S. Ma, Z. Zhang, K. Liu, J. Qi, H. Zeng, S. U. Rehman, W. Ren, et al., Giant rotating magnetocaloric effect enhanced by crystal electric field in antiferromagnetic $ErNi_3Al_9$ single crystal, Journal of Alloys and Compounds 847 (2020) 156478.

[52] M. Balli, S. Jandl, P. Fournier, J. Vermette, D. Z. Dimitrov, Unusual rotating magnetocaloric effect in the hexagonal $ErMnO_3$ single crystal, Phys. Rev. B 98 (2018) 184414.

[53] Pecharsky, Vitalij K and Gschneidner Jr, Karl A, Giant magnetocaloric effect in Gd_5 (Si_2Ge_2), Physical review letters 78 (1997) 4494.

[54] C. Delacotte, T. A. Pomelova, T. Stephant, T. Guizouarn, S. Cordier, N. G. Naumov, P. Lemoine, $NaGdS_2$: A promising sulfide for cryogenic magnetic cooling, Chemistry of Materials 34 (2022) 1829–1837.

[55] Q. Xu, B. Liu, M. Ye, G. Zhuang, L. Long, L. Zheng, Gd (OH) F_2: A promising cryogenic magnetic refrigerant, Journal of the American Chemical Society 144 (2022) 13787–13793.

[56] T. Krenke, E. Duman, M. Acet, E. F. Wassermann, X. Moya, L. Mañosa, A. Planes, Inverse magnetocaloric effect in ferromagnetic Ni–Mn–Sn alloys, Nature materials 4 (2005) 450–454.

[57] Tohei, T and Wada, H and Kanomata, T, Negative magnetocaloric effect at the antiferromagnetic to ferromagnetic transition of Mn_3 GaC, Journal of Applied Physics 94 (2003) 1800–1802.

[58] K. Sandeman, R. Daou, S. Özcan, J. Durrell, N. Mathur, D. Fray, Negative magnetocaloric effect from highly sensitive metamagnetism in CoMnSi $_{1-x}$ Ge_x, Physical Review B 74 (2006) 224436.

[59] V. K. Dwivedi, P. Mandal, S. Mukhopadhyay, Frustration-Induced Inversion of the Magnetocaloric Effect and Metamagnetic Transition in Substituted Pyrochlore Iridates, ACS Applied Electronic Materials 4 (2022) 1611–1618.

[60] L. Xu, H. Niu, Y. Bai, H. Zhu, S. Yuan, X. He, Y. Han, L. Zhao, Y. Yang, Z. Xia, et al., Shubnikov–de haas oscillations and nontrivial topological states in weyl semimetal candidate SmAlSi, Journal of Physics: Condensed Matter 34 (2022) 485701.

[61] R. Singha, S. Roy, A. Pariari, B. Satpati, P. Mandal, Magnetotransport properties and giant anomalous Hall angle in the half-Heusler compound TbPtBi, Phys. Rev. B 99 (2019) 035110.

[62] D. Ram, J. Singh, M. K. Hooda, O. Pavlosiuk, V. Kanchana, Z. Hossain, D. Kaczorowski, Electronic structure and physical properties of the candidate topological material gdagge, Phys. Rev. B 107 (2023) 085137.

[63] M. Lyu, J. Xiang, Z. Mi, H. Zhao, Z. Wang, E. Liu, G. Chen, Z. Ren, G. Li, P. Sun, Nonsaturating magnetoresistance, anomalous Hall effect, and magnetic quantum oscillations in the ferromagnetic semimetal PrAlSi, Phys. Rev. B 102 (2020) 085143.

[64] H. Su, X. Shi, J. Yuan, Y. Wan, E. Cheng, C. Xi, L. Pi, X. Wang, Z. Zou, N. Yu, W. Zhao, S. Li, Y. Guo, Multiple Weyl fermions in the noncentrosymmetric semimetal LaAlSi, Phys. Rev. B 103 (2021) 165128.

[65] H.-Y. Yang, B. Singh, J. Gaudet, B. Lu, C.-Y. Huang, W.-C. Chiu, S.-M. Huang, B. Wang, F. Bahrami, B. Xu, J. Franklin, I. Sochnikov, D. E. Graf, G. Xu, Y. Zhao, C. M. Hoffman, H. Lin, D. H. Torchinsky, C. L. Broholm, A. Bansil, F. Tafti,

Noncollinear ferromagnetic Weyl semimetal with anisotropic anomalous Hall effect, Phys. Rev. B 103 (2021) 115143.

[66] J.-F. Wang, Q.-X. Dong, Z.-P. Guo, M. Lv, Y.-F. Huang, J.-S. Xiang, Z.-A. Ren, Z.-J. Wang, P.-J. Sun, G. Li, G.-F. Chen, NdAlSi: A magnetic Weyl semimetal candidate with rich magnetic phases and atypical transport properties, Phys. Rev. B 105 (2022) 144435.

[67] E. Jobiliong, J. S. Brooks, E. S. Choi, H. Lee, Z. Fisk, Magnetization and electrical-transport investigation of the dense kondo system $CeAgSb_2$, Phys. Rev. B 72 (2005) 104428.

[68] A. Auerbach, Interacting electrons and quantum magnetism, Springer Science & Business Media, 2012.

[69] S. Nallamuthu, S. S. Chandrasekaran, P. Murugan, M. Reiffers, R. Nagalakshmi, Magnetic, thermodynamic and transport properties of novel non-centrosymmetric $RCoSi_3$ (R= Pr, Nd and Sm) compounds, Journal of Magnetism and Magnetic Materials 416 (2016) 373–383.

[70] J.-S. Rhyee, J. Y. Kim, B. K. Cho, Multiple magnetic transitions and magnon gaplike characteristics in the high purity TbB_4 single crystal, Journal of Applied Physics 101 (2007). 09D509.

[71] J. Kim, N. Sung, B. Kang, M. Kim, B. Cho, J.-S. Rhyee, Magnetic anisotropy and magnon gap state of SmB_4 single crystal, Journal of Applied Physics 107 (2010) 09E111.

[72] J. L. Luo, N. L. Wang, G. T. Liu, D. Wu, X. N. Jing, F. Hu, T. Xiang, Metamagnetic transition in $Na_{0.85}CoO_2$ single crystals, Phys. Rev. Lett. 93 (2004) 187203.

[73] S. Nakatsuji, D. Hall, L. Balicas, Z. Fisk, K. Sugahara, M. Yoshioka, Y. Maeno, Heavy-mass fermi liquid near a ferromagnetic instability in layered ruthenates, Phys. Rev. Lett. 90 (2003) 137202.

[74] S. Malick, J. Singh, A. Laha, V. Kanchana, Z. Hossain, D. Kaczorowski, Electronic structure and physical properties of EuAuAs single crystal, Phys. Rev. B 105 (2022) 045103.

[75] M. Marshall, I. Pletikosić, M. Yahyavi, H.-J. Tien, T.-R. Chang, H. Cao, W. Xie, Magnetic and electronic structures of antiferromagnetic topological material candidate $EuMg_2Bi_2$, Journal of Applied Physics 129 (2021). 035106.

[76] W. Shon, J.-S. Rhyee, Y. Jin, S.-J. Kim, Magnetic polaron and unconventional magnetotransport properties of the single-crystalline compound $EuBiTe_3$, Phys. Rev. B 100 (2019) 024433.

[77] B. Lv, H. Weng, B. Fu, X. P. Wang, H. Miao, J. Ma, P. Richard, X. Huang, L. Zhao, G. Chen, et al., Experimental discovery of weyl semimetal TaAs, Physical Review X 5 (2015) 031013.

[78] A. Narayanan, M. D. Watson, S. F. Blake, N. Bruyant, L. Drigo, Y. L. Chen, D. Prabhakaran, B. Yan, C. Felser, T. Kong, P. C. Canfield, A. I. Coldea, Linear magnetoresistance caused by mobility fluctuations in n-doped Cd $_3$ As_2, Phys. Rev. Lett. 114 (2015) 117201.

[79] J. Hu, Z. Tang, J. Liu, X. Liu, Y. Zhu, D. Graf, K. Myhro, S. Tran, C. N. Lau, J. Wei, Z. Mao, Evidence of topological nodal-line fermions in ZrSiSe and ZrSiTe, Phys. Rev. Lett. 117 (2016) 016602.

[80] J. Hu, Z. Tang, J. Liu, Y. Zhu, J. Wei, Z. Mao, Nearly massless dirac fermions and strong zeeman splitting in the nodal-line semimetal ZrSiS probed by de haas–van alphen quantum oscillations, Phys. Rev. B 96 (2017) 045127.

[81] E. Emmanouilidou, B. Shen, X. Deng, T.-R. Chang, A. Shi, G. Kotliar, S.-Y. Xu, N. Ni, Magnetotransport properties of the single-crystalline nodal-line semimetal candidates Ca T X (T= Ag, Cd; X= As, Ge), Phys. Rev. B 95 (2017) 245113.

[82] A. Laha, S. Malick, R. Singha, P. Mandal, P. Rambabu, V. Kanchana, Z. Hossain, Magnetotransport properties of the correlated topological nodal-line semimetal YbCdGe, Phys. Rev. B 99 (2019) 241102.

[83] P. E. Blöchl, Projector augmented-wave method, Phys. Rev. B 50 (1994) 17953–17979.

[84] Gradhand, M and Fedorov, DV and Pientka, Falko and Zahn, P and Mertig, I and Györffy, BL, First-principle calculations of the Berry curvature of Bloch states for charge and spin transport of electrons, J. Phys.: Condens. Matter 24 (2012) 213202.

[85] Zhang, Rui and He, Yangkun and Chen, Kaiyun and Yang, Sen and Sen, Siddhartha and Coey, JMD, Influence of topology on the phase transition of a ferromagnetic metal, Proc. Natl. Acad. Sci. 120 (2023) e2302466120.

Chapter 6

Summary

In my thesis, my primary focus has been on exploring the electrical and magnetic characteristics of three materials: $Cr_{0.79}Se$, $FeCr_2Te_4$, and $HoSiAl_2$. Here are the key findings:

- In chapter 3, We ascertain that $Cr_{0.79}Se$ is synthesized with the same NiAs-type hexagonal crystal structure as the stoichiometric CrSe, in contrast to other off-stoichiometric systems that exhibit different crystal symmetries. Analysis of resistivity data indicates that $Cr_{0.79}Se$ behaves as a Fermi-liquid-type metal at low temperatures, while at higher temperatures, the resistivity shows a sublinear dependence on temperature. Significantly, we observe weak ferromagnetism below 100 K alongside antiferromagnetism. Consequently, there is a notable exchange bias below 100 K due to the interaction between the ferromagnetic and antiferromagnetic phases. Therefore, we are reporting, for the first time, the existence of exchange bias in Cr_xSe systems.

- In chapter 4, we have conducted a thorough investigation of the electrical transport, magnetotransport, and magnetic properties in $FeCr_2Te4$ single crystal. The temperature-dependent resistivity, ρ_{xx}, shows the influence of electron-magnon scattering and spin fluctuations scattering below the magnetic ordering temperature. Furthermore, we have examined the impact of increasing magnetic field on different scattering mechanisms in this compound. The temperature-dependent MR demonstrates a maximum negative MR in close proximity to T_c, which amplifies with higher magnetic field strengths. Remarkably, our Hall resistivity measurements have unveiled a direct correlation between the observed MR behavior across T_c and the carrier concentration in this compound. Overall, our study on $FeCr_2Te_4$ presents a promising platform for investigating spin-dependent transport phenomena both theoretically and experimentally.

- In chapter 5, we have investigated the physical properties of $HoSiAl_2$ single crystals by measuring the magnetic susceptibilty, magnetocaloric effect, magnetoresistance

, Hall effect, and by calculating the electronic band structure. We conclude that $HoSiAl_2$ crystallizes in monoclinic space group(space group C12/m1(12)). The magnetic susceptibility measurements displayed that $HoSiAl_2$ has AFM Transitions around T_N=7K along H$\perp$ c and around T_N=3K along H$\parallel$ c axis. In the ordered state , the magnetization increases linearly with increasing field, then saturates in the high field region. dM/dH vs H data along H$\perp$ c shows couple of spin-flop type metamagnetic transition. For H$\parallel$ c, the magnetization is far from saturation. For a magnetic field change of 0-7T at 8K, we have obtained Δ S_M=-27.427J/Kg K for H$\parallel$ c axis and -17.528J/Kg K H$\perp$ c axis. We have got the maximum value of positive Δ S_M at H=H_c (around 2.5T), matched with our magnetization data. Below T_N, the transverse magnetoresistance displays a positive maximum, implying metamagnetic tarnsition, and it saturates at negetive value. For $T < T_N$, the resistivity data is fitted by AFM magnon relation. The field dependent Hall measurements show that dominating charge carriers are hole. By employing first-principles calculations, we show that $HoSiAl_2$ exhibits an antiferromagnetic Weyl semimetal ground state.